NANOCELLULOSE PROPERTIES MEASURED BY ATOMIC FORCE MICROSCOPY

INVESTIGATION OF NANOCELLULOSE MECHANICAL PROPERTIES AND INTERACTIONS IN SALT AND SURFACTANT SOLUTIONS MEASURED BY ATOMIC FORCE MICROSCOPY

By HEERA SINGH MARWAY, B.ENG.BIOSCIENCES

A Thesis

Submitted to the School of Graduate Studies

in Partial Fulfillment of the Requirements for the

Degree Master of Applied Science

Master of Applied Science (2016) McMaster University

(Chemical Engineering) Hamilton ON

Master of Applied Science (2016) McMaster University

(Chemical Engineering) Hamilton ON.

Title: Investigation of Nanocellulose Morphology, Mechanical Properties and Surfactant Interactions using Atomic Force Microscopy

Author: Heera Singh Marway, B.Eng.Biosciences (McMaster University)

Supervisor: Professor Emily D. Cranston

Number of Pages: xviiii, 138

Lay Abstract

Nanocellulose is a sustainable nanomaterial most commonly extracted from plants and trees. In recent research, nanocellulose has been shown to have potential as a reinforcing agent for materials such as plastics, foams, paints and adhesives. In this study, the potential of nanocellulose was investigated using atomic force microscopy (AFM). As predicted, AFM measurements indicated that nanocellulose has a high stiffness, supporting the substitution of this biobased material in the place of metals and synthetic fibres. AFM was also used to examine particle interactions in salt and soap-like (surfactant) solutions; changes in nanocellulose size and charge were used to support the findings. Negatively charged nanocellulose interacted more with positively charged surfactants and vice versa. Low salt and high surfactant concentrations led to high adhesion and better material compatibility, which is preferred. This understanding can help us design better nanocellulose materials for future applications.

Abstract

In this study, the potential of nanocellulose as a reinforcing agent in composite materials was investigated using atomic force microscopy (AFM). AFM was used to probe the mechanical properties of nanocelluloses and to investigate their interactions and adhesion in liquid media. Amplitude modulated-frequency modulated AFM was used to map the mechanical properties of cellulose nanocrystals (CNCs) and cellulose nanofibrils (CNFs). Results showed Young's moduli of 90 GPa and 120 GPa for CNCs and CNFs, respectively, which are comparable to literature values determined using other methods.

Additionally, colloid probe AFM was implemented to observe the interactions (attractive, repulsive, steric, adhesive) between cellulose and silica colloid probes with anionic CNCs (containing either a Na^+ or H^+ counterion) and cationic CNCs. Colloid probe AFM measurements were carried out in five different liquid media: two salt solutions (NaCl and $CaCl_2$) and three surfactant solutions (cationic cetyltrimethylammonium bromide, CTAB; anionic sodium dodecyl sulfate, SDS; and nonionic Triton X100). It was found that low salt concentrations resulted in electrostatic repulsion and high adhesion, whereas the reverse was observed at high salt concentrations. On the contrary, an increased surfactant concentration and increased number of surfactant aggregates (micelles, bilayers, etc.) resulted in increased adhesion. Surprisingly, the interactions were strongly dependent on the CNC counterion as surfactant adsorption seemed to be primarily driven by electrostatic interactions; CTAB adsorbed more to anionic CNCs, SDS adsorbed more to cationic CNCs and Triton X100 adsorbed minimally to all CNCs. Electrophoretic mobility and particle size data showed

complementary results to colloid probe AFM, indicating that interactions between surfactants and CNC films and CNCs in suspension are closely related. This research suggests that CNCs have potential as reinforcing agents due to their high strength and the tunability of their interactions through the simple addition of salts or surfactants. This understanding can be directly applied in future formulation design to use nanocellulose in polymer nanocomposites, foams, emulsions, latexes, gels and biomedical materials.

Acknowledgments

Firstly, I would like to express my gratitude to my supervisor Dr. Emily Cranston, without her constant encouragement, guidance and support none of this work would have been possible. Thank you for taking a chance and hiring me as one of your first summer students. I cannot thank you enough for always being patient with me.

I would also like to thank past and current members of the Cranston research group for your useful discussions, suggestions, and assistance. To Kevin Kan, Justin Yang, Justin Hu, Joseph Pang and Jonathan Monster thank you for letting me discover new techniques and instruments with you. To Dr. Tiffany Abitbol, thank you for letting me help you with your very exciting work, teaching me how to use the AFM and being my reading buddy. To Dan LeClair, Stephanie Kedzior, Mike Reid, Urooj Gill, Kevin Defrance, Dan Osorio, and Lexa Graham thank you for creating a nurturing and friendly work environment. To all the summer students that I have had the pleasure of working with thank you for your questions and useful suggestions.

Special thanks to Dr. Robert Pelton, Dr. Carlos Filipe, Dr. Todd Hoare, and Dr. Moran-Mirabal for access to their instruments and expertise. Thanks to Dr. Emil Gustafsson for answering all my random science questions and useful suggestions. Thanks to Paul Gatt, Dan Wright and Doug Keller for your much appreciated support, suggestions and technical assistance.

Lastly, I would like to thank my friends and family for their continuous support and encouragement. To my parents and brothers who always push me to do my best, thank you for your guidance, support and unwavering love, words will never be enough.

Table of Contents

Table of Tables

Table of Figures

Abbreviations

AFM	Atomic force microscopy
AM-FM AFM	Amplitude modulated-frequency modulated AFM
BNA	Beycostat NA
Cat-CNCs	Cationic cellulose nanocrystals
CMC	Critical micelle concentration
CNCs	Cellulose nanocrystals
CNFs	Cellulose nanofibrils
CP-AFM	Colloid probe atomic force microscopy
CTAB	Cetyl trimethlyammonium chloride
DLS	Dynamic light scattering
EM	Electrophoretic mobility
H-CNCs	Acid form cellulose nanocrystals
HCl	Hydrochloric acid
Na-CNCs	Sodium form cellulose nanocrystals
NTA	NanoSight single particle tracking analysis
R	Radius
SDS	Sodium dodecyl sulfate
TEMPO	(2,2,6,6-tetramethylpiperidin-1-yl)oxyl
TX100	Triton X100
VDW	van der Waals
W	Work

Declaration of Achievement

I declare that the research contribution that follows represents original work, completed and written by myself, with editorial assistance from my supervisor, Dr. Cranston.

The production of Cationic CNCs and NanoSight single particle tracking analysis and electrophoretic mobility experiments in Chapters 5 were done in collaboration with Stephanie Kedzior.

Scanning Electron Microscopy images were taken by Xuan (Justin) Yang.

The following is a list of publications, in chronological order, which I have made significant contributions to as a research assistant under the supervision of Dr. Cranston.

Abitbol, T.; Marway, H.; Cranston, E. D.; "Surface Modification of Cellulose Nanocrystals with Cetyltrimethylammonium Bromide." *Nordic Pulp Paper Research Journal, 29*, 46, February **2014**.

Hu, Z.; Marway, H. S.; Kasem, H.; Pelton, R.; Cranston, E. D. Dried and Redispersible Cellulose Nanocrystal Pickering Emulsions. *ACS Macro Letters*, *5*, 185, January **2016**.

Dong, X.; Marway, H. S.; Cranston, E. D.; Pelton, R. H. "Relating nanoparticle shape and adhesiveness to performance as flotation collectors", Ind. Eng. Chem. Res. **2016**.

1. Introduction

1.1 Nanocellulose as a Mechanical Reinforcing Agent in Composite Systems

Fibers have been used throughout history as reinforcing agents. Lately, the focus of reinforcing agents has turned towards nanotechnology which takes advantage of unique properties such as high strength-to-weight ratio, large specific surface area, quantum effects, and self-assembly which can only be realized by particles with nanoscale dimensions. Nanocellulose, a class of bio-based nanofibers derived mainly from wood, plants, and bacteria, has become the focus of much research due to its favourable mechanical properties, biodegradability, and non-toxic nature [1]. Cellulose nanocrystals (CNCs) are one type of nanocellulose that exhibit a very high degree of crystallinity, which is often associated with stiff and strong materials. Moreover, with the recent initiative to "go green", nanocellulose has quickly gained popularity as a potential reinforcing agent for various polymers and cement systems.

Like many bio-based materials, the two main challenges associated with nanocellulose are its strong sensitivity to water and its poor compatibility with hydrophobic matrices [2]. Despite this, researchers have incorporated CNCs into many composite systems and have demonstrated improved mechanical properties [3–6]. Yet incorporating CNCs into hydrophobic polymers remains challenging largely due to unknown particle-matrix interactions. Thus to improve the development of composite materials we seek to establish a fundamental understanding of these interactions.

In this work, the interactions in nanocellulose–silica and nanocellulose–cellulose model systems (in air, salt solutions and surfactants) are probed to develop an understanding that will help optimize the formulation of nanocellulose composites.

Ideally, the knowledge gained will aid in the development of a large number of material systems that take full advantage of green bio-based nanofibers through enhanced compatibility and uniform distribution of reinforcing agents.

1.2 Atomic Force Microscopy as a Mechanical Measurement Technique

Atomic force microscopy (AFM) is a scanning probe microscopy technique that was first developed as a topographical technique to extend the capabilities of scanning tunneling microscopy to nonconductive surfaces. AFM employs a cantilever with a sharp tip that causes the cantilever to deflect when rastered across a surface. The deflection of this cantilever is recorded and translated into a topographical map.

Since its development, AFM functionality has been extended beyond just topographic measurements to include measurements of conductivity, indentation, mechanical properties, magnetic fields and numerous spectroscopy techniques [7]. The AFM has also permitted the development of techniques that do not rely on topographical information such as lithography, friction and interaction force measurements [8]. Recent advances have further allowed for the detection of nanomechanical characteristics by amplifying what are normally subtle changes in the cantilever deflection [9]. Additionally, the replacement of the sharp tip with a colloidal particle (ca. 1- 50 μm) allows researchers to probe a wide range of materials, detect smaller forces, and compare measurements to established theories. Of these techniques, force measurements, in which the cantilever is moved vertically to and from the surface, is of great interest as it can provide insight into fundamental surface interactions such as DLVO, steric, electrosteric, hydrophobic, and solvation interactions.

1.3 Research Objectives

This work strives to resolve the issues surrounding the development of novel nanocellulose composites first by comparing mechanical properties of two nanocellulose types using amplitude modulated-frequency modulated AFM imaging (AM-FM AFM) and secondly by elucidating the links between cellulose nanocrystal surface chemistry and adhesion using AFM force measurements.

Mechanical Measurements by AM-FM AFM:

This work presents the first AM-FM AFM measurements of nanocelluloses. This technique accurately measures the elastic modulus using a small sample set and greatly improves upon other measurement methods, which require large sample volumes and offer non-trivial preparation and analysis procedures.

Surface Force Measurements by Colloid Probe AFM:

The goal of this work is to learn what properties influence cellulose nanocrystal interactions using colloid probe AFM force measurements in salt and surfactant solutions. The findings in this project may guide predictions of cellulose nanocrystal behaviour in emulsions, gels, foams, latexes, composites and biological systems.

1.4 Thesis Outline

The content of this thesis is divided into seven chapters, including the Introduction. Chapter 2 presents a literature review discussing the preparation and characterization of nanocellulose materials along with an overview of AM-FM AFM and direct surface force measurement using colloid probe AFM. Chapter 3 summarizes the experimental

procedures and characterization techniques used in this research. Chapter 4 presents the results and discussion of AFM imaging using AM-FM AFM mode where an elastic modulus for cellulose nanofibrils (CNFs) and cellulose nanocrystals (CNCs) is determined. Chapter 5 presents results and discussion of direct surface force measurements of CNC surfaces using colloid probe AFM – focusing on *approach curves* only. Experiments were done in salt and surfactant solutions for which the electrostatic interactions and the presence/absence of surfactant aggregates at the surface are also discussed. The results gathered are compared to changes in CNC surface charge and apparent size in the presence of surfactants, as measured by electrophoretic mobility and NanoSight particle tracking analysis, respectively. Chapter 6 presents results and discussion for the direct surface force measurements of CNC surfaces using colloid probe AFM – this time focusing on *retraction curves* only, to elucidate adhesive behavior in the presence of salt and surfactant solutions. The occurrence of adhesion, or lack thereof, is discussed with respect to the approach force measurements presented in Chapter 5. Concluding remarks and suggestions for future work are presented at the end of chapters 4, 5 and 6 and a general conclusion for the entire thesis is given in Chapter 7.

2. Literature Review

2.1 Cellulose

Cellulose, the most abundant polysaccharide on earth, is the main structural framework of higher order plants, such as trees, making it a renewable, sustainable and carbon neutral material. Other than trees, cellulose serves as a key structural component of plants as well as some fungi, algae and sea life (ie. tunicate) [10]. It is also produced by some bacteria, where it is excreted to form an external network or as a mode of propulsion [11]. This abundance and adaptability has led cellulose to be used in a wide variety of applications ranging from traditional paper and board products to fillers in pharmaceuticals and even biomedical devices. The ability of cellulose to impart structural support has sparked the interest of many researchers looking for a renewable resource to enhance strength either as a support material or as a functional filler in composites.

Cellulose is a linear polymer made up of glucose rings (anhydro-D-glucose) linked together covalently. This is done via an oxygen at the C1 position of one glucose ring and the C4 position of the other glucose ring resulting in a β-1,4-glycosidic bond. This in turn forms the repeat unit of cellulose: cellobiose, as seen in Figure 2.1 [1].

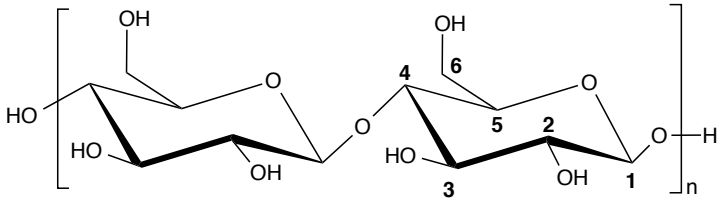

Figure 2.1: Cellulose repeat unit cellobiose, where n is the number of repeat units in the cellulose chain and the numbers indicate the carbon position on the anhydro-D-glucose rings.

The number of cellobiose units per cellulose chain, or degree of polymerization (n), is a property-inherited from the cellulose source. Some sources and their respective degree of polymerization are listed in Table 2.1.

Table 2.1: Cellulose sources and corresponding degree of polymerization, where n is the number of cellobiose units. Adapted from [12]**.**

Cellulose	Degree of Polymerization (n)
Wood of various species	6,000-10,000
Pulp	500-2,000
Sulfate pulp	950-1,300
Cotton	10,000-15,000
Cotton linters bleached	1,000-5,000
Bacterial cellulose	4,000-6,000
Textile flax	9,000
Rayon	300-500
Cellophane	300
Cellulose acetate	200-350

Figure 2.2 shows the hierarchical structure of cellulose within a tree. Plants produce the cellulose "building blocks" by using carbon dioxide and water, whereas bacteria, algae and fungi build cellulose by using sugars. Hydrogen bonding and van der Waals (VDW) forces between adjacent cellulose chains during biosynthesis promote stacking of the chains into elementary fibrils which then further aggregate into macrofibrils, this goes on to become key components in the plant structure as seen in Figure 2.2.

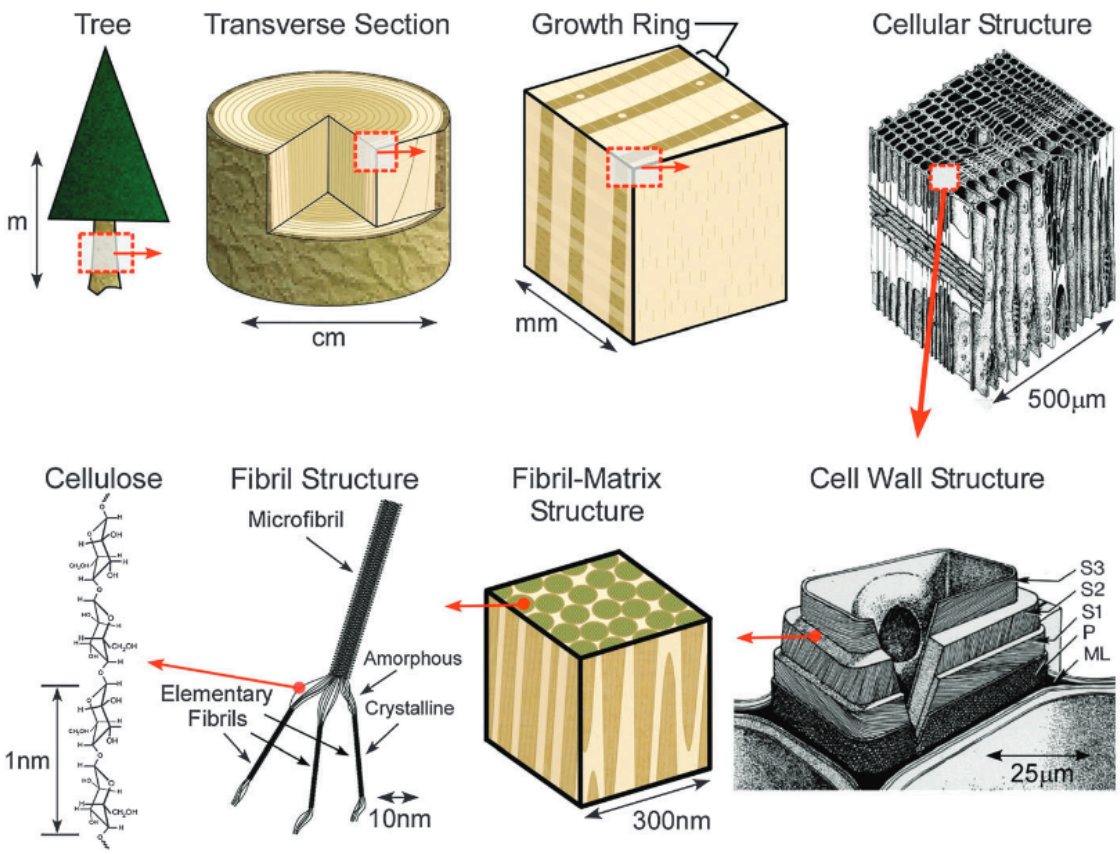

Figure 2.2: Hierarchical structure within a tree. Reproduced from [13]**.**

During the industrial revolution, cellulose and its derivatives were investigated intensely for their important properties and potential applications [14]; the same trend is true today for nanocellulose.

2.2 Nanocellulose

Nanocellulose is a sub class of cellulosic materials and generally includes cellulose nanofibrils (CNFs), cellulose nanocrystals (CNCs) and bacterial cellulose (BC). CNFs are always plant-derived and produced through mechanical disintegration processes. CNCs can be extracted from plants, bacteria, algae and animals but always by chemical methods. BCs refers to the nano-scale ribbons synthesized directly by Gluconacetobacter

xylinus [13]. The classification of nano comes from the materials having a width (or both length and width) in the nanometer range as shown in Table 2.2.

Table 2.2: Typical length, width and aspect ratio for cellulose nanofibers, cellulose nanocrystals from cotton and wood, and bacterial cellulose.

Nanocellulose type		Length (nm)	Width (nm)	Aspect ratio (L/d)	Reference
Cellulose nanofibrils		500-2000	4-20	25-500	[13]
Cellulose nanocrystals	from cotton	100-210	5-10	10-42	[15]
	from wood	100-300	3-5	20-100	
Bacterial cellulose		many microns	20-100	>1000 μm	[16]

Recently nanocellulose has attracted considerable attention, which is attributed to its availability, renewability, high strength-to-weight ratio and biocompatibility [3,17]. Nanocellulose has been shown to be adaptable to many applications however currently very few commercial products exist. Applied research with nanocellulose generally focuses on nanocomposites and hybrid materials, and more specifically packaging, gels and foams with CNFs, coatings and rheological modifiers with CNCs, and biomedical and wound healing applications with BC. Table 2.3 provides a list of some potential applications for the three major types of nanocellulose.

Table 2.3: Potential applications of nanocellulose by nanocellulose type ranging from fillers to standalone devices.

Nanocellulose type	Application	Reference
Cellulose nanofibrils	Hydrogels	[13]
	Packaging and barrier coating	[18]
	Composites	[1,19]
Cellulose nanocrystals	Hydrogels and aerogels	[20–23]
	Coatings	[13,24]
	Chiral nematic films/ templates	[25]
	Emulsions	[26]
	Drug delivery	[27,28]
	Tissue engineering	[28,29]
	Energy storage	[30,31]
	Water treatment	[32]
	Composite materials	[1,33,34]
Bacterial cellulose	Hydrogels (and wound healing)	[1,35,36]
	Films	[37]
	Thickeners for foods	[1]
	Food (Nata de coco)	[1,38]

2.2.1 Cellulose Nanofibrils

Cellulose nanofibrils, also known as nanofibrillated cellulose (NFC) or microfibrillated cellulose (MFC), are plant-based cellulose fibers broken down to the micron and nanoscale. Nanocellulose research and industrial production in Europe and

Japan has primarily focused on CNFs whereas the North American attention has been on CNCs [39]. CNFs, which consist of both amorphous and crystalline cellulose regions, are made through mechanical processes with high shear, sometimes combined with chemical or enzymatic pretreatments [40] and non-harsh chemical processes which lead to the degradation of cellulose. There are a variety of mechanical disintegration methods to produce CNFs including: high-pressure homogenization, grinding, cryocrushing, and high-intensity ultrasonication [1,5,16].

CNFs can be thought of as a "spaghetti-like" form of nanocellulose where the fibrils have significant flexibility and can easily entangle. They are stable as colloidal suspensions in water due to surface charged groups which either stem from residual hemicelluloses, or carboxyl or carboxymethyl groups introduced onto the surface during chemical pretreatment [41–43]. CNFs can be further broken down to CNCs with acid hydrolysis or oxidation, but this is an energy/cost intensive method and therefore an uncommon route to CNC production. Current industrial efforts are focused on reducing the energy of production for CNFs through chemical pretreatment, improved mechanical equipment and the addition of mineral grinding agents that may aid in the intended applications [44,45].

2.2.2 Cellulose Nanocrystals

Canada is currently the world-leader in the industrial production of CNCs with ton-per-day capabilities, soon to be even larger [46,47]. CNCs are rigid rod-shaped nanoparticles, or more "rice-like" compared to CNFs, and are highly crystalline cellulose in the native cellulose I crystal form. While there are different methods to produce CNCs, such as enzymatic hydrolysis, oxidation with ammonium persulfate, ionic liquid

treatment, sub and super-critical water treatment, and hydrolysis with gaseous acid, liquid acid hydrolysis is the most common process [1]. Acids such as sulfuric, hydrochloric, acetic, hydrobromic [3], citric or phosphoric acid [3,13,48] can be used to hydrolyze cellulose, where the amorphous regions are preferentially degraded and the crystalline regions are isolated into nanocrystals as shown schematically in Figure 2.3.

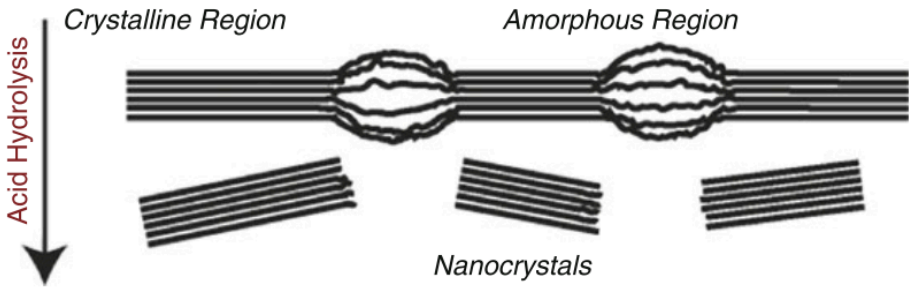

Figure 2.3: The use of acid hydrolysis to separate the crystalline regions of cellulose leaving isolated nanocrystals. Reproduced from [49]**.**

The hydrolysis reaction mechanism where the proton from the acid attacks the ester bond between glucose units is shown in Figure 2.4.

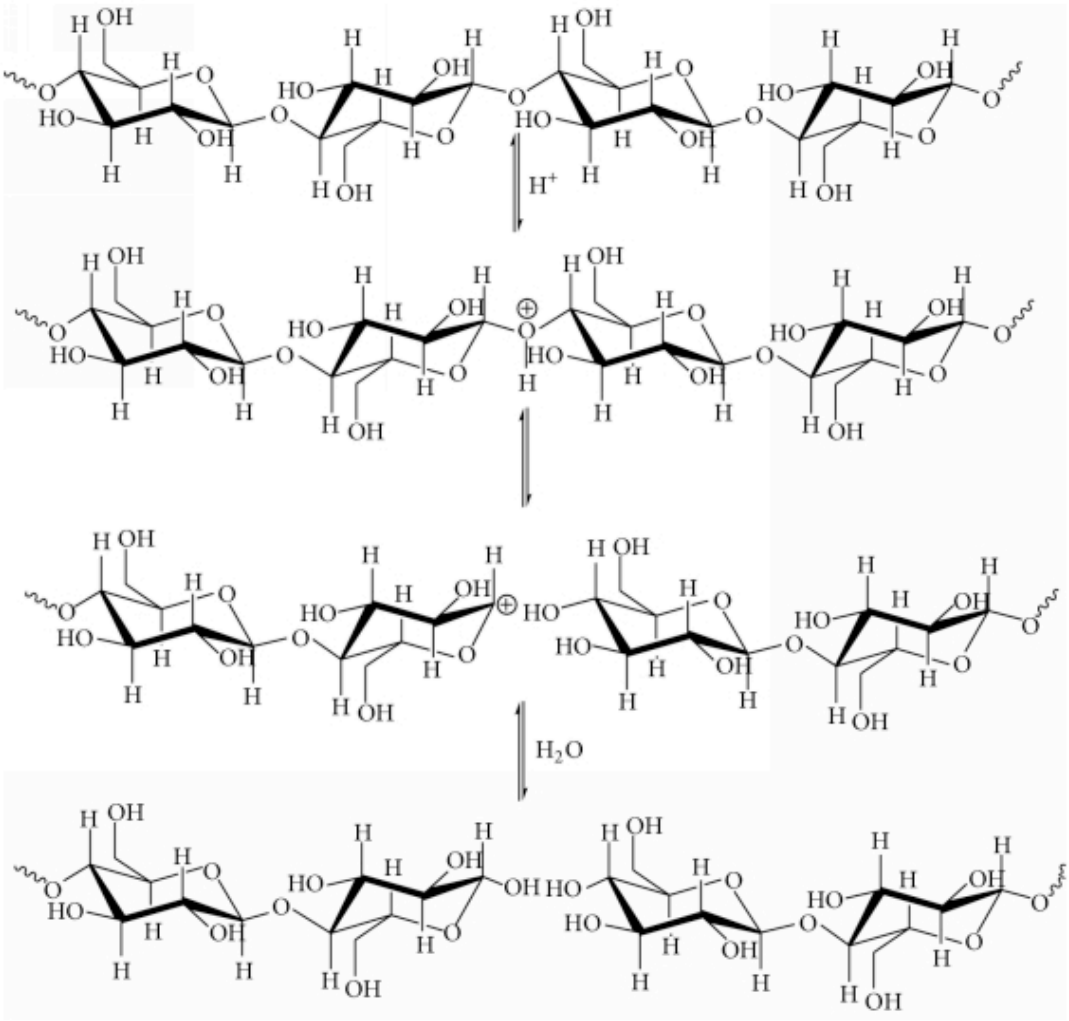

Figure 2.4: General mechanism for the acid hydrolysis of accessible (i.e. amorphous) cellulose to produce CNCs. Reproduced from [50]**.**

Sulfuric and hydrochloric acid are the most commonly used acids and lead to cellulose nanocrystal surfaces with sulfate half esters in the case of sulfuric acid, or no grafted surface groups in the case of HCl; in some cases HCl hydrolyzed CNCs can have carboxyl groups introduced using (2,2,6,6-tetramethylpiperidin-1-yl)oxyl (TEMPO) oxidation, as shown in Figure 2.5 [51]. These surface groups dictate how the nanocrystals behave in suspension, in chemical reactions and for drying/redispersing purposes.

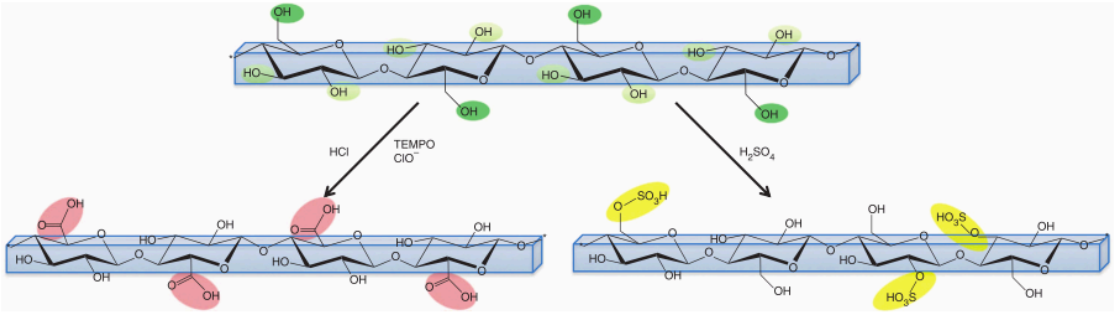

Figure 2.5: Surface functionality of acid hydrolyzed cellulose by either hydrochloric acid followed by TEMPO oxidation or by sulfuric acid. Reproduced from [51] **.**

Sulfuric acid hydrolyzed CNCs are the most studied due to their high yield and the colloidal stability above pH 2.5, whereby sulfate half esters are dissociated giving CNCs a negative surface charge. Industrially produced CNCs currently use sulfuric acid, which is low cost and can be recycled. While microcrystalline cellulose (MCC or Avicel used as pharmaceutical excipients) is produced industrially using hydrochloric acid, it is only a partial hydrolysis leaving aggregated crystalline cellulose particles of undefined size and shape. Harsher hydrochloric acid conditions are needed to produce rod-shaped particles but the product yield is generally low and due to the lack of surface charged groups, the CNCs are unstable in suspension and tend to aggregate irreversibly.

To enhance the shelf life of sulfuric acid hydrolyzed CNCs in suspension, acid form CNCs (H-CNCs, i.e. where the sulfate half ester group has a proton as the counterion, $-OSO_3^-H^+$, shown in yellow in Figure 2.5) are often neutralized from their acid form to a salt form through the addition of a base. Most commonly NaOH is added which displaces hydrogen on the sulfate half ester converting H-CNCs to sodium-form CNCs (Na-CNCs). This neutralization process has been found to reduce the degradation of CNCs over time, decrease the auto-catalyzed desulfation of CNCs (which leads to loss of colloidal stability), and also reduces the hydrogen bonding between CNCs when dried, which

means that the Na-CNCs can much more easily be redispersed into stable aqueous suspensions after drying compared to H-CNCs [52].

The type of acid used to extract CNCs imparts a unique surface chemistry that contributes to the CNCs' physical and chemical properties. Although, due to their low surface charge, CNCs produced using phosphoric acid (P-CNCs) and hydrochloric acid (HCl-CNCs) are less colloidally stable in suspension than CNCs produced using sulfuric acid. It has been seen that both P-CNCs and HCl-CNCs have a higher thermal stability than sulfuric acid-extracted CNCs, with P-CNCs being the most thermally stable [53]. However, CNCs produced by all methods share a few fundamental physical properties: they are rod-shaped anisotropic particles which have a large dipole moment, piezoelectric properties [54], and align in electric and magnetic fields [55]. Importantly, CNCs are chemically inert, and do not dissolve easily, such that to interrupt H-bonding, hydrophobic interactions and the crystalline structure of CNCs requires unconventional solvents (such as ionic liquids) or mixed solvent systems (like LiCl/N,N-dimethylacetamide) [13,56]. The most discussed property of CNCs is probably the Young's modulus (~70 GPa) which has been shown to be similar to that of Kevlar (60-125 GPa) and accounting for material density, as a ratio between the Young's modulus and density, CNCs (65 GPa cm^3/g) are often said to be stronger than steel (25 GPa cm^3/g) [57,58]. These properties offer diverse application potential and ways to process CNCs into structured and functional materials [59,60].

2.2.3 Limitations of Nanocellulose in Nanocomposites

Although nanocellulose is seen as a material with great potential, particularly as a reinforcing agent in nanocomposites, it has some drawbacks in terms of compatibility.

Cellulose is hydrophilic due to the high density of surface hydroxyl groups (three per anhydroglucose unit) and does not interact well with most hydrophobic polymers and non-polar solvents. Furthermore, for some applications/processing, such as melt-compounding, the heat tolerance of cellulose is insufficient. These drawbacks of nanocellulose have led to significant research focused on increasing the dispersabilty and stability of nanocellulose in solvents and polymer matrices which are typically used during the production of nanocomposites [1]. Fortunately, CNCs can be easily modified based on their surface "chemical handles" which facilitate chemical reactions and physisorption of molecules that can help compatibilize cellulose with other materials.

2.2.4 Surface Modification of Nanocellulose

Literature demonstrates a variety of physical and chemical modification routes for nanocellulose with the goal to increase compatibility with solvents and polymers; this is summarized in a comprehensive review by Habibi [61]. Physical adsorption with polysaccharides, hydrophilic polymers, polyelectrolytes and surfactants (or bulky amphiphilic salts) presents a straightforward and water-based functionalization strategy which is likely more industrially feasible than the chemical modification routes discussed below. For example, our group has recently shown that the coupling of cationic surfactant cetyl trimethlyammonium chloride (CTAB) to CNCs through ionic interactions can be controlled through solution parameters and the modified CNCs can be dispersed in increasingly non-polar solvents [62]. Similar studies with surfactants have been done by others showing the compatibilizing nature of surfactant adsorption [63–68]. From a compounding perspective, it has been demonstrated that modification of CNCs with

surfactants can lead to better thermal stability and dispersability of modified CNCs in, for example, polylactic acid [69] polystyrene [6] and polypropylene matrices [70].

Chemical modification of the surface of nanocellulose by small molecules (esterification, silylation, cationization) or polymers can be done by following well-known carbohydrate chemistry; some of the routes are illustrated in Figure 2.6. Grafting polymers either *from* the surface [33,71–74] or *to* the surface [75] are possible but are often limited by the need to work in solvents where nanocellulose is colloidally unstable, are multistep/multi-purification processes or result in low grafting yields. While both physical and chemical modification methods share the same compatibilization end goal, polymer grafting or chemical modification can also have the benefit of adding functionality such as responsive behavior, fluorescence, conductivity, etc.

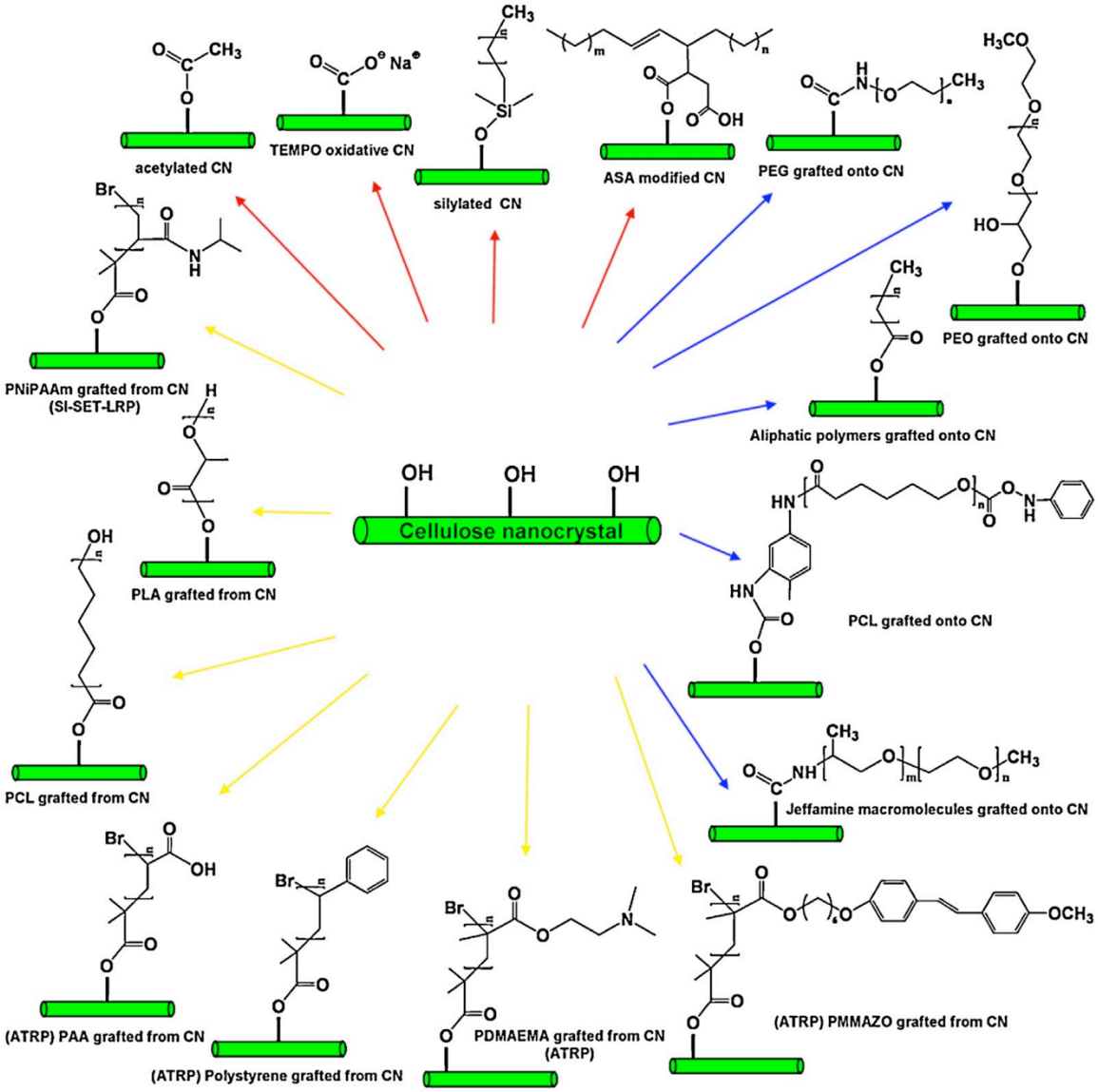

Figure 2.6: Cellulose nanocrystal surface modification routes where red arrows indicate surface modification, blue arrows *graft to* and yellow *graft from* polymerization. [PEG: poly(ethylene glycol); PEO: poly(ethylene oxide); PLA: poly(lactic acid); PAA: poly(acrylic acid); PNiPAAm: poly(N-isopropylacrylamide);and PDMAEMA: poly(N,N-dimethylaminoethyl methacrylate)]. Reproduced from [48] **and similar modification routes are available for CNFs** [5]**.**

2.2.5 Nanocellulose Properties and Characterization Techniques

Characterization of nanocellulose often includes many sophisticated instruments such as dynamic light scattering (DLS), NanoSight single particle tracking analysis (NTA), atomic force microscopy (AFM), polarized optical microscopy, electron microscopy, electrophoretic mobility (EM), conductometric titrations, x-ray diffraction

(XRD), elemental analysis, neutron/x-ray scattering and x-ray photoelectron spectroscopy (XPS). Before one starts working with a material it is important to characterize it and understand what it is that they are working with. The information obtained from these techniques, their theory, limitations, and average values for CNCs are listed Table 2.4.

Table 2.4: Typical techniques used for the characterization of cellulose nanocrystals with a corresponding description of information provided, underling or governing theory, technique limitations, and average values.

Technique	Information	Theory	Limitations	Average value/range for CNCs	References
Morphology					
DLS/NanoSight	Particle size: "apparent" diameter	Diffusion and Brownian motion	Not accurate for non-spherical particles (can be used to track CNC consistency and changes in size but not absolute values unless combined with other techniques)	70-200 nm	[33,76,77]
AFM	Particle size and distribution, shape, morphology	Hook's law relates deflection of cantilever to force and topography	Tip convolution for lateral measurements	Length: 90-150 nm Height: 5-10 nm	[78]
Polarized optical microscopy (with retardation plate)	Liquid crystal self assembly, chiral nematic pitch, and birefringence (indirect measurement of CNC dispersion)	Optics	Cannot see nanoparticles so dispersion is assessed based on uniformity of birefringence	Chiral nematic pitch of nm to μm, birefringence of 0.06, for well dispersed composites a uniform color (pink or yellow) is observed	[79–81]
Electron Microscopy	Particle size and morphology	Optics	Sample preparation	Length:147± 18 nm Width: 7 ± 1 nm	[82]

XRD (X-Ray Diffraction)	Crystallinity	Bragg's Law	Fitting	~94% crystalline	[66,74,83]
Neutron/X-ray scattering	Orientation/ arrangement of particles in solution	Light/particle scattering	Aggregation biases results, and extensive data processing/modeling	Particle alignment twist decreases 1° for each ~3% increase in solid concentration	
Surface Chemistry					
EM/Zeta Potential	Surface charge (+/-)	Smoluchowski equation to convert to zeta potential	Unreliable for non-spherical particles	-2.5×10^{-8} $m^2V^{-1}s^{-1}$ for EM and -39 ± 3 mV Zeta Potential (better if reported as electrophoretic mobility)	[84]
Conductometric Titration	Number of surface charge groups for sulfate and phosphate esters or COOH groups	Acid-base chemistry	Ionic strength of suspension must be sufficiently high, CNCs must be in acid form, cannot differentiate different strong acid groups on the surface	0.5-0.7 % S 15 – 20 mmol S/kg, 6.8×10^{-21} glucose units per charge, 0.41 *e*/nm^2 (for H_2SO_4 hydrolyzed CNCs)	[71,85,86]
XPS (X-Ray Photoelectron Spectroscopy)	Atomic composition at the surface and binding state of elements	Optics and electron binding	Surface contamination	Surface concentration of: O: 42.6%, C: 57.1%, S: 0.3%. Carbon type: C1: 12.5%, C2: 69.6%, C3: 18.1%	[87]
Elemental Analysis	Atomic content	Various depending on method	Sample size	0.6 % sulfur (S)	[86]

2.3 Surfactants

The term "surfactant" is an abbreviation for surface-active agent, meaning that surfactants are molecules that are active at interfaces, which results in a lowering of interfacial tension. An interface is the boundary between two immiscible phases, be it solid/vapour, solid/liquid, solid/solid, liquid/vapour or liquid/liquid. The preference of surfactants for the interface is due to their amphiphilic nature, having one hydrophilic/polar end (typically the head) and a hydrophobic/non-polar end (typically the tail/tails) as shown in Figure 2.7.

Figure 2.7: A typical surfactant structure with a hydrophilic head and hydrophobic tail.

Due to their preference for interfaces and chemical asymmetry, increasing the amount of surfactant in a liquid decreases the surface tension of that liquid, while increasing osmotic pressure until a plateau is reached and further surfactant addition does not lead to changes in surface tension or osmotic pressure [88]. The surface at this point is, in a sense, saturated with surfactant. Surfactant molecules added beyond this point start to aggregate and form various structures, the most common are spherical micelles [88]. The concentration where this transition occurs is called the critical micelle concentration, CMC (or critical aggregation concentration for non-micelle forming surfactants), and depends on the surfactant structure and chemical make-up.

Surfactants can be classified by their head groups which fall into four different categories: cationic, anionic, zwitterionic and nonionic, where the cationic and anionic surfactants are accompanied by counter ions as seen in Figure 2.8 [88]. The difference in

both the head and tail group, for example the number, length and structure, plays a big role in how the surfactant behave in solution, structures at the interface and the morphology of the aggregates [89].

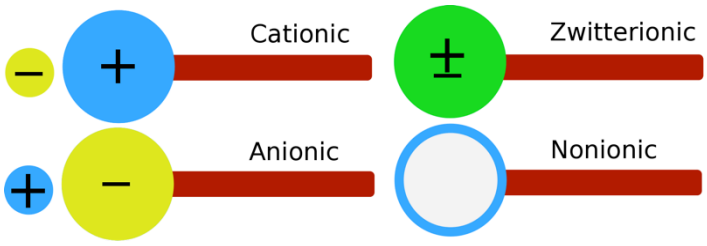

Figure 2.8: A schematic showing the four classes of surfactants: cationic, anionic, zwitterionic, and non-ionic.

2.3.1 Morphology

In aqueous solutions, at concentrations below the CMC, surfactant molecules quickly migrate and adsorb at the air/water or solid (container)/water interface where they orient to minimize the contact between the hydrophobic parts (tails) of the surfactant and the hydrophilic solvent (water) [89]. This adsorption of surfactant at the interface helps to keep the surfactant from being completely expelled from the surface and changes the properties of the interface. The surfactant molecules tend to form a film of single molecules at the air/liquid interface or micelles that pack closer and closer together at the liquid/solid surface until the CMC is reached [88]. At the CMC, the formation of micelles, where the hydrophobic groups face the inside of the aggregate and the hydrophilic groups face the outside, starts. The formation of micelles is an entropy driven process governed mainly by hydrophobic interactions [90]. Depending on the hydrophobic interactions of the non-polar ends, molecular packing (due to steric hindrance) of the tails, and the electrostatic repulsion between the polar ends, the shape of the surfactant aggregates ranges from lamellar, Figure 2.9 A, to spherical, Figure 2.9 B, to cylindrical, Figure 2.9 C [88,91]. Reverse micelles, Figure 2.9 D, occur in hydrophobic

solvents or when the tail group of the surfactant is more hydrophilic that the head group. At concentrations significantly higher than the CMC, micelles are forced to pack into larger structures, known as mesostructures, such as bicontinuous structures, Figure 2.9 E, or hexagonal arrays, Figure 2.9 F [91].

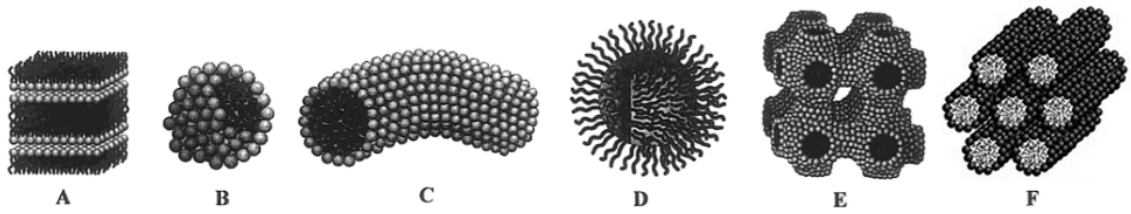

Figure 2.9: Typical surfactant structures and mesostructuers where (A) is lamellar, (B) spherical micelle, (C) cylindrical micelle, (D) reverse micelle, (E) bicontinuous mesostructure and (F) a hexagonal array. Adapted from [91]**.**

In the literature, three surfactants: CTAB, sodium dodecyl sulfate (SDS), and Triton X-100 (TX100) have been studied extensively and are often studied together to offer a complete picture of surfactant interactions [90,92–94]. CTAB (Figure 2.10) is a cationic surfactant with a CMC of 1 mM in water at room temperature and a micelle diameter of 3 nm [90]. Typical uses of CTAB are in cosmetics, such as hair conditioners [95,96], and as templates, i.e.. for gold nanoparticle synthesis [97].

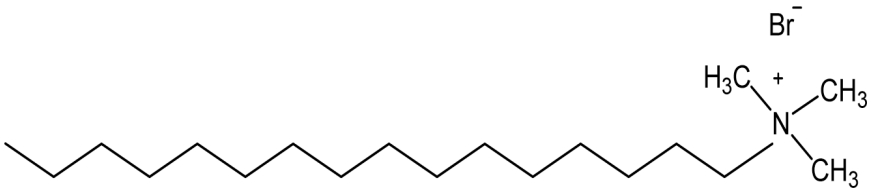

Figure 2.10: The chemical structure of cetyltrimethylammonium bromide.

SDS (Figure 2.11) is an anionic surfactant with a CMC of 8.2 mM in water at room temperature and a micelle diameter of 1.5 nm [98]. Typical uses of SDS are shampoos, biological cell lysis/gel electrophoresis, and detergents [99].

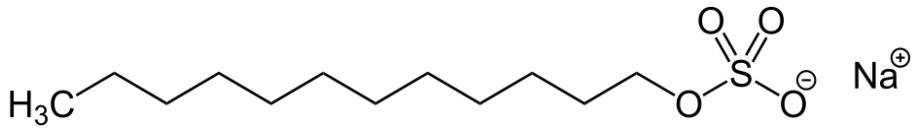

Figure 2.11: The chemical structure of sodium dodecyl sulfate.

TX100 (Figure 2.12) is a nonionic surfactant with a CMC of 0.24 mM in water at room temperature and a micelle diameter of 5.4 nm [100–102]. Triton X-100 has a hydrophobic head and a hydrophilic tail and no charged groups, in contrast to CTAB and SDS. Typical uses of TX100 are pharmaceuticals, cleaning solutions, and dispersant for biological cells [100].

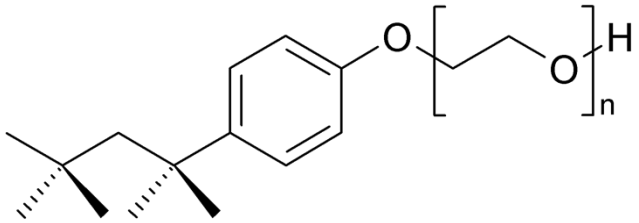

Figure 2.12: The chemical structure of Triton X where n for Triton X-100 is an average of 9.5 ethylene glycol units.

2.3.2 Surfactants as Additives

Amphiphilic properties make surfactants ideal for compatibilizing and linking boundaries between hydrophilic and hydrophobic substances leading to a wide variety of uses. Applications range from detergents and coating products such as paints, to pharmaceuticals and food as depicted in Figure 2.13 [103]. Among the many applications of surfactants is their application with cellulose and paper products.

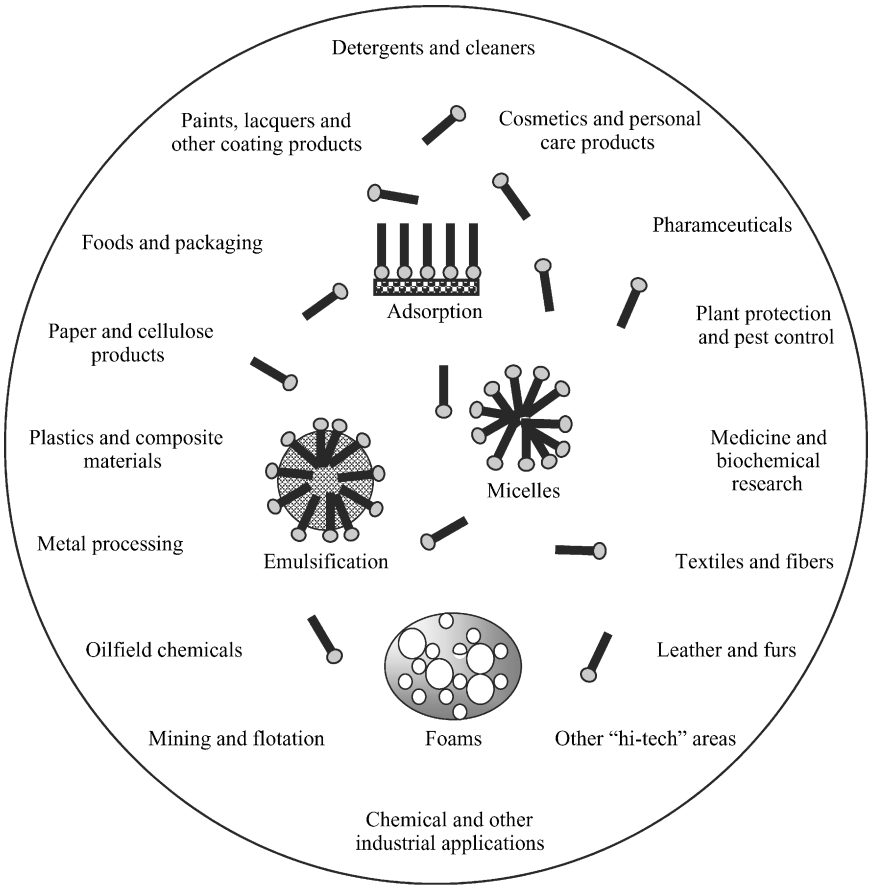

Figure 2.13: A general list of surfactant applications. Reproduced from [103]**.**

2.3.3 Surfactants and Cellulose

The interactions between cellulose and surfactants have been long studied, for example, various surfactants are used in the recycling of paper products in the deinking processes [104,105], and in the production of tissue and antistatic paper [106–108]. Cellulose-surfactant interactions are greatly influenced by surface charge, surfactant tail length, ionic strength and the concentration of components in solution [109–111]. On a smaller scale, surfactants with micro or nanocellulose have been studied for the production of gels [64,94,112], emulsions [113], functional materials such as adsorbents

for organic molecules and antiseptic coatings [62,114–116], and to improve the compatibility of cellulose in composites [68,70,117,118].

CNCs were the first nanocelluloses to be modified with surfactants, as presented by Heux and coworkers. Their study aimed to improve CNC dispersion in hydrophobic materials by using an ethoxylated phosphoric ester of nonylphenol surfactant, commercially known as Beycostat NA (BNA) [63,65]. Continuing this work, CNCs modified with BNA or a variant Beycostat A B09, shown in Figure 2.14, were used to produce CNC-polymer composites with polypropylene and polylactic acid [69,117–120]. While the adsorbed surfactant increased the CNC dispersion, the surfactant had adverse effects to the polymer matrix itself. Similar surfactant-modified CNCs were also dispersed in organic solvents and their self-assembly and alignment in an electric field were studied [116,121,122].

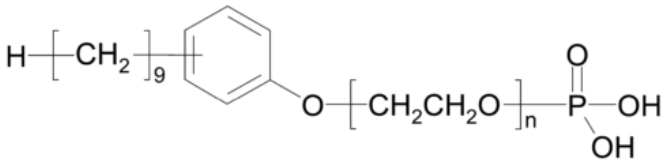

Figure 2.14: Chemical structure of the Beycostat series of commercial surfactants. Chemical structure reproduced from [116]**.**

Following those works, Salajkova et al. and Abitbol et al. modified CNCs with bulky amphiphilic cations, i.e. quaternary ammonium salts with increasing alkyl chain lengths on COOH-CNCs and CTAB on sulfuric acid-extracted CNCs, respectively [62,66]. In both reports, the adsorption of cationic surfactant to the surface of CNCs allowed for re-suspension in non-polar solvents and furthermore, preserved the CNC liquid crystalline properties [16]. In another example, Hu et al. showed that the addition of cationic CTAB or didecyldimethyl ammonium bromide increased the stability and

tailorability of CNC-stabilized Pickering emulsions by increasing the hydrophobicity and surface activity of CNCs [113]. Nagalakshmaiah et al. demonstrated that CNCs modified using hexadecyl trimethylammonium bromide could be incorporated into a polypropylene matrix at high loadings (10 wt % CNCs) without discoloration upon thermal treatment, whereas, it was shown that a 3 wt % CNC-polypropylene composite without surfactant discolored after heating (Figure 2.15) [70].

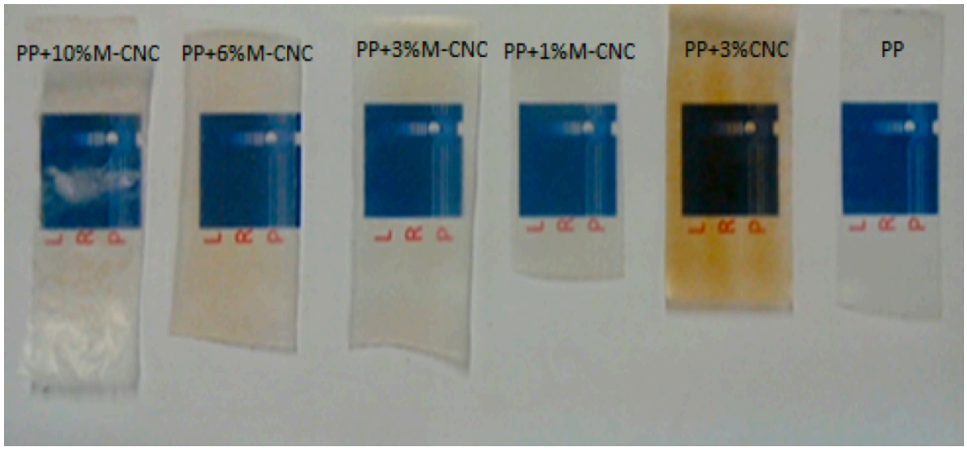

Figure 2.15: Blends of CNCs modified with hexadecyl trimethylammonium bromide and neat CNCs with polypropylene (PP) and neat PP processed by compounding at 190 °C in a double screw set-up. Image reproduced from [70]**.**

Non-ionic surfactants have also been shown to help in the dispersion of CNCs in a polymer matrix. Through the addition of sorbitan monostearate (span-60), a nonionic surfactant, Kim et al., created CNC-polystyrene suspensions in THF [6]. The suspensions showed decreasing turbidity with increasing surfactant content, likewise the solvent cast films from these suspensions showed a macroscopic increase in CNC dispersion with increasing surfactant content [6]. Extending this study further, Rojas et al. electrospun CNC-polystyrene nanocomposite fibers form a THF suspension with the help of span-60. A control without surfactant showed that the HCl-hydrolyzed CNCs aggregated into

clusters that appeared along the spun fiber but upon addition of surfactant, smooth fibers were produced as shown in Figure 2.16 [4].

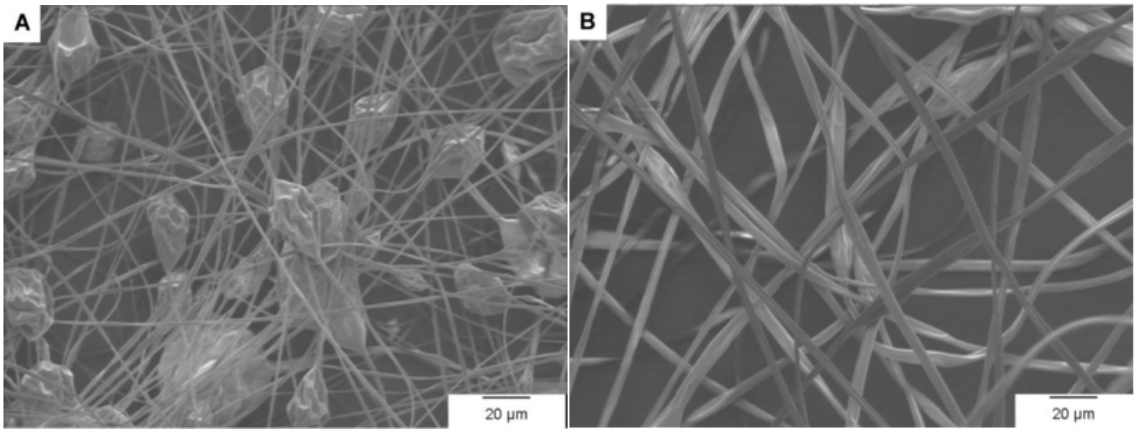

Figure 2.16: SEM micrographs of electrospun fibers of polystyrene and 6 wt % CNCs, (A) without surfactant (B) with surfactant, from a THF suspension. Figure reproduced from [4]**.**

Other than improving CNC dispersibility in polymers, understanding surfactant-cellulose interactions can lead to functional materials, such as cellulose and surfactant complexes. Aloulou et al. showed that the adsorption of cationic surfactants (like CTAB) to the surface of cellulose fibers (~200 µm in length) facilitated the adsorption of hydrophobic materials to the fiber surface [114,123]. For example, 2-naphthol, benzene and quinolone were effectively removed from aqueous media by surfactant-modified fibers, extending potential applications of cellulose fibers to water treatment [114]. It was also shown that increasing the chain length of the surfactant increased the affinity of the surfactant to move to the surface, such that the local surfactant concentration on the surface could surpass the CMC and increase the amount of organic compounds removed from the aqueous environment [114]. In a similar study using CNCs, CTAB modification was used to couple anti-cancer drugs to CNCs for controlled release applications [124].

Interestingly, it has been demonstrated that the interaction of surfactants with CNCs versus CNFs is not always the same; in a study by Quennouz et al. neutral

surfactants such as Triton X-100 and Pluronic F68 were shown to have no effect on CNFs' natural tendency to gel, whereas ionic surfactants such as cationic dodecyltrimethyl ammonium bromide (DTAB) and SDS destabilized the gel [94]. However, through rheology it was seen that anionic sodium lauryl ether sulfate (SLES, Figure 2.17) enhanced the stability of the CNF gels, a property that is attributed to the ethylene chain between the head and tail group, as this was the only chemical difference from other surfactants tested and the main difference between SDS and SLES. This is in contrast to Hu et al. that showed that strong polysaccharide-CNC gels could be destabilized by the addition of SDS or TX100 (because the surfactant removed the polysaccharides adsorbed to the CNC surface), however, cationic CTAB bound to and improved the gels overall [92]. While the adsorption of surfactants to cellulosic materials can extend the possible applications, these studies highlight the delicate balance of cellulose and surfactant type and that other components such as salts, polymers, etc. will also play a significant role in controlling suspension properties and compatibilization.

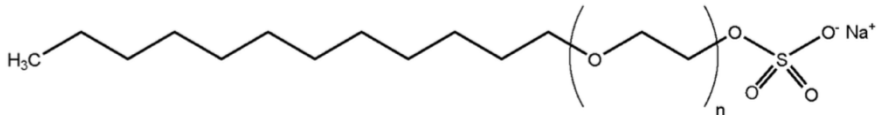

Figure 2.17: Chemical structure of sodium lauryl ether sulfate where n = 3. Figure reproduced from [94]**.**

2.4 Atomic Force Microscopy (AFM)

2.4.1 Introduction

AFM is a scanning probe microscopy (SPM) technique which was first developed by Binnig et al. to extend the imaging resolution of scanning tunneling microscopy (STM) to nonmetallic or insulating materials [125]. Since then, the AFM has evolved to become a technique that is regularly used to measure not only topography but also

mechanical, surface and chemical properties of all types of molecules, nanoparticles, and materials. In addition, AFM has been used as a tool for lithography, etching and deposition to create micron to nanoscale patterns [126,127]. AFM has been a key enabling technique in the development of nanoscience and nanotechnology [128].

2.4.2 AFM Mechanics

The AFM instrument consists of a spring like cantilever with a sharp tip, which is used to probe the surface of a moving sample, a laser and photodiode detector to track the movement of the cantilever, and a stage embedded with piezoelectric positioners, which rasters the sample of interest under the tip. The typical AFM set-up is shown in Figure 2.18.

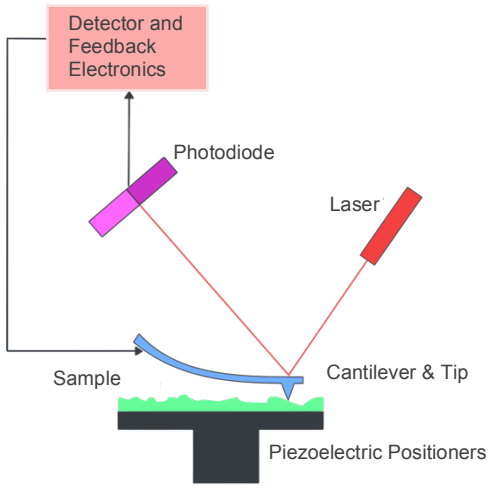

Figure 2.18: A simplified AFM setup. Adapted from Wikipedia Commons.

The sample is placed on top of a stage, which moves it back and forth. The movement of the tip, deflection of the spring like cantilever with respect to surface features, is measured using a laser beam reflected off the back of the AFM cantilever into a 4-quadrant photodiode [8]. These measurements are mapped pixel by pixel into lines as

the sample moves under the AFM tip consecutively building line upon line in order to produce an image of the sample surface.

AFM is widely used and capable of providing a range of surface properties. Topographical data can be collected in either contact mode, where the AFM tip drags across the surface (often used for hard surfaces) or tapping mode, where the AFM tip makes intermittent contact with the surface (useful for all types of surfaces, even very delicate samples such as DNA). In tapping mode, also called amplitude modulated (AM) or alternating current (AC) mode, the cantilever is oscillated at its resonant frequency and the drive frequency and amplitude are held constant by adjusting the distance between the AFM tip and the sample surface through a feedback loop. The contact time between the tip and surface and how hard the tip is tapping can be adjusted to minimize tip dulling and sample damage.

Typical data collected in tapping mode are height, amplitude, phase and z-sensor position. The height data is the height change of the piezoelectric scanner in the vertical (z) direction needed to keep the cantilever oscillation amplitude constant as it move across the sample. The amplitude channel records the change in amplitude with position as the AFM tip tracks the sample surface. Since the amplitude is a set parameter, this data is essentially an error measurement. Due to the high sensitivity to the changes in the x and y plane, amplitude data can be used to show fine features and can often give a visual representation of sample morphology, but should not be used for any quantitative measurements. Phase data, which corresponds to the phase shift in, or stability of the cantilever oscillation, can be used to monitor changes in the sample material properties. This data can be related to various properties such as sample modulus, adhesion,

toughness etc. however, definitive and quantitative interpretation of this data is not currently possible. The z-sensor data records the same information as the height data when the feedback loop is working perfectly.

2.4.3 Advanced Mode: Amplitude Modulated-Frequency Modulated AFM

Amplitude modulated–frequency modulated AFM mode (AM-FM AFM) is a bimodal AFM technique that can be used to quantitatively measure the mechanical properties of a sample, most commonly the Young's modulus. The technique is an add-on to AM (tapping) mode where it combines the signal of the first resonance frequency, AM mode, and a higher resonance frequency, FM mode, of a cantilever to extract additional information during AFM imaging. Resonating at a higher frequency, typically the second resonance frequency, gives a better indication of tip surface interactions by amplifying the information received at higher frequencies, such information is otherwise undetectable or difficult to interpret [128–130].

The set-up for AM-FM mode is the same as tapping mode except that it requires a high frequency specific cantilever holder, and that the signal that is used to drive the cantilever is a combination of both the fundamental (first harmonic, F_1) and a higher (usually the second or third harmonic, F_2) frequency. As a result of the combined signal input, the output signal, collected as cantilever deflection, is also a combined signal that is deconvoluted and displayed as maps of the scanned surface (Figure 2.19) [128].

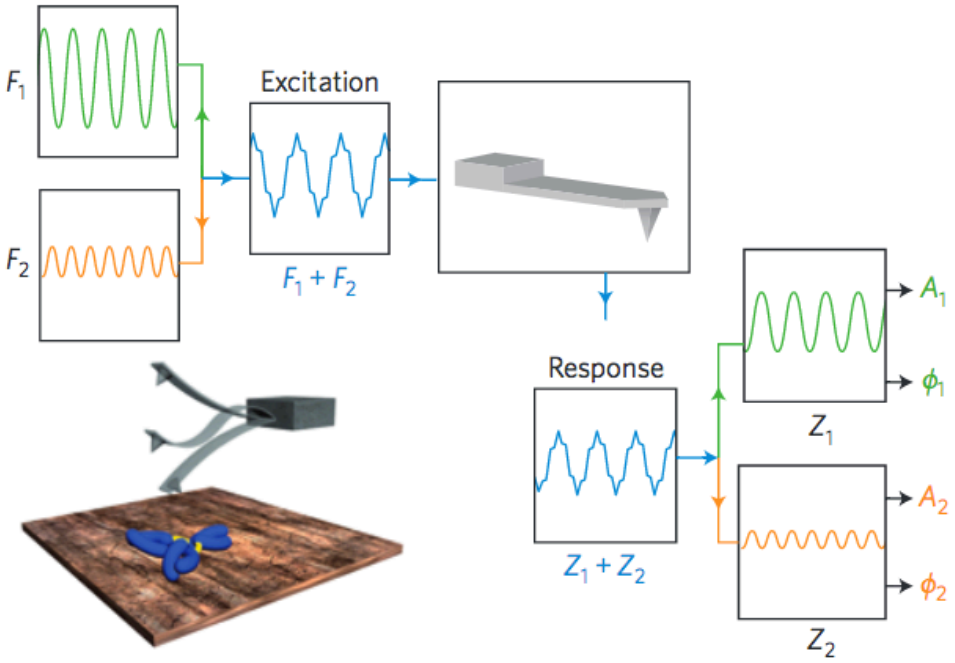

Figure 2.19: Schematic of bimodal AFM measurement where the subscript 1 refers to information gathered using the first resonance or AM mode and 2 refers to information gathered using the second resonance or FM mode. Reproduced from [128]**.**

AM-FM collects changes in the sample through the AFM cantilever dissipation, frequency and indentation from the higher frequency in addition to height, amplitude, phase and z-sensor trace and retrace data from the first frequency. A stiffer sample will shift the F_2 signal to a value larger than the frequency setpoint (second or third harmonic, $f_{0,2}$) whereas a softer sample shifts it lower. This shift in frequency (Δf_2) can be used to calculate the corresponding material elasticity expressed as the Young's modulus using Equation 2.1 derived from Hertz contact mechanics,

$$E_{eff} = -\frac{\Delta f_2 \, k_2}{f_{0,2} r_c} \qquad \text{Equation 2.1}$$

Where E_{eff} is the local Young's modulus of the tip-surface interface, k_2 is the stiffness of the second mode, and r_c is the contact area between the surfaces [9].

In one of the first AM-FM AFM studies published, the technique was shown to quantitatively identify the location of polymers in a blend based on their Young's moduli as shown in Figure 2.20 [9].

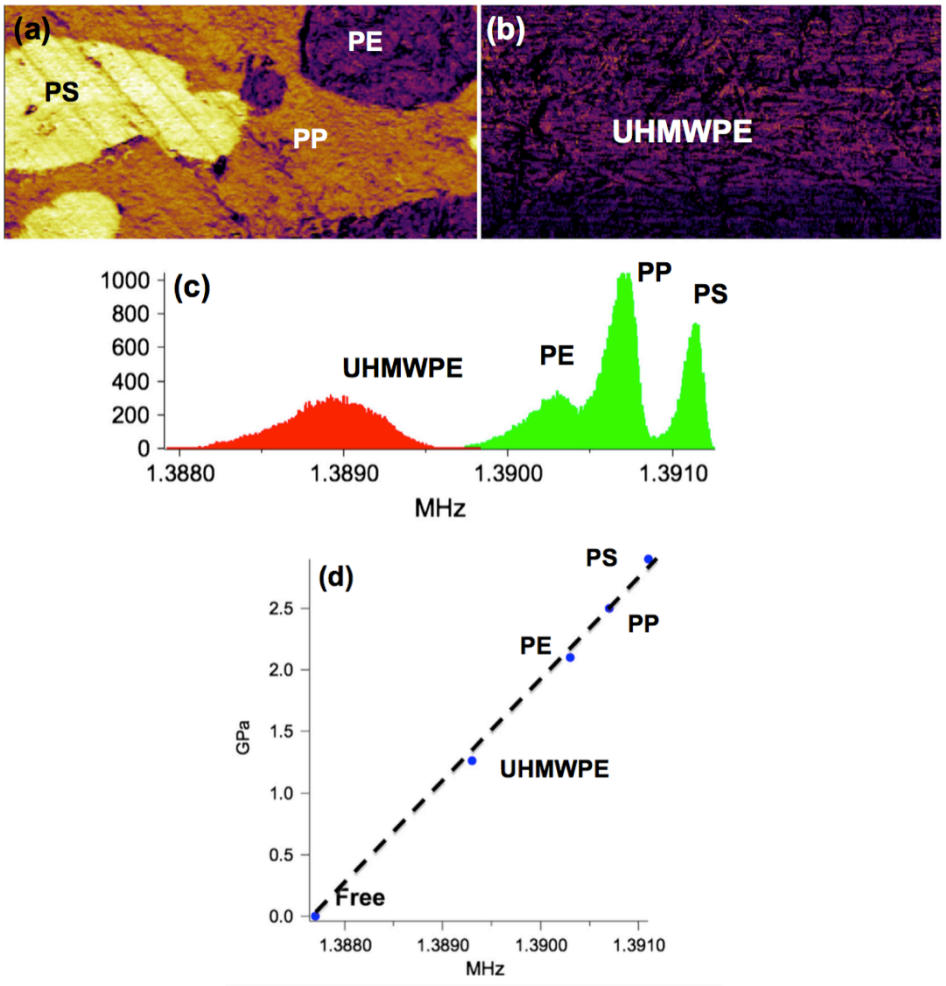

Figure 2.20: AM-FM images (15 µm scans) of polymer surfaces; (a) polypropylene (PP), polyethylene (PE), polystyrene (PS) blend, (b) ultra-high molecular weight polyethylene (UHMWPE), used as a reference for the Young's modulus, (c) a histogram of the frequency shifts taken from a section of the AFM image and (d). the calculated Young's modulus based on the change in frequency. Reproduced from [9]**.**

Lamour et al. used AM-FM AFM to determine the axial and radial Young's moduli of mouse prion nanofibrils (Figure 2.21). In this study, it was demonstrated that the Young's modulus of a very soft structure such as prions can be measured using AM-FM with good agreement to literature [131].

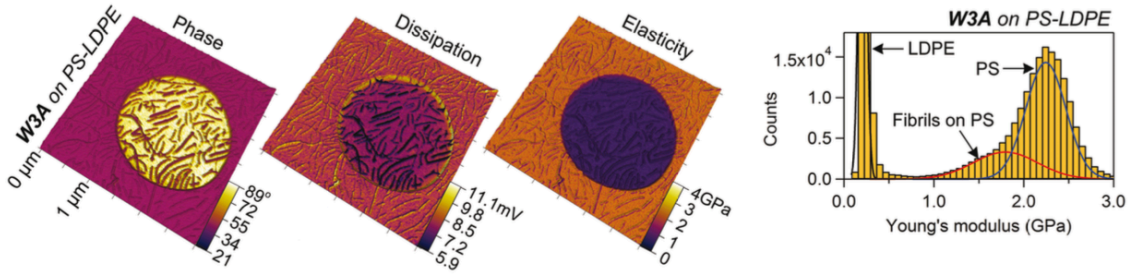

Figure 2.21: Selected AFM images of phase, dissipation and elasticity for mouse prion nanofibrils on a polymer blend of polystyrene (PS) and low-density polyethylene (LDPE), used as a reference and a histogram of the measured Young's moduli. Reproduced from [131]**.**

2.5 Surface Forces and Colloid Probe Microscopy

2.5.1 Surface Forces

Surface and intermolecular forces govern the fundamentals of matter. By studying these fundamental aspects we strive to understand and gain new knowledge on how particles and molecules interact in contact and in close proximity. There are various surface forces and techniques used to measure them. This work focuses on measuring DLVO and adhesion forces using colloid probe AFM.

2.5.2 DLVO

DLVO theory is named after Derjaguin, Landau, Verwey and Overbeek – four scientists who simultaneously worked to understand fundamental particle interactions in 1945. The theory describes the interactions between charged particles in liquid media and is generally used to predict colloidal stability [132,133]. DLVO interactions include attractive VDW and repulsive electrostatic double layer forces between particles of the same composition (i.e., symmetric systems). The theory also applies to asymmetric systems where repulsive VDW and attractive double layer forces can also exist. VDW forces are always present short range interactions (attractive or repulsive) between

electrically neutral species, i.e. interactions that are not due to covalent bonds or electrostatic interaction between ions; there are three contributions to VDW forces: interactions due to two permanent dipoles known as Keesom (permanent-permanent dipole) interactions, interaction between a permanent dipole and dipole induced by the proximity of the permanent dipole known as the Debye (permanent-induced dipole) force, and the interaction between a fluctuation dipole and its induced dipole know as the London dispersion (dipole-induced dipole) force. VDW forces can be calculated using Hamaker theory, Equation 2.2, which accounts for the pairwise interactions of particles.

$$W_{VDW} = -\frac{A}{12\pi D^2} \qquad \text{Equation 2.2}$$

Here W_{VDW} is the VDW interaction energy, A is the Hamaker constant of the materials, and D is the distance between two planar surfaces. The Derjaguin approximation, Equation 2.3, can be used to derive the VDW interaction energy for non-planar surfaces, including spheres and crossed cylinders with radius R [134,135].

$$W_{VDW}(D) = \frac{F(D)_{sphere-plane}}{2\pi R} = \frac{F(D)_{sphere-sphere}}{\frac{2\pi(R_1R_2)}{R_1+R_2}} = \frac{F(D)_{crossed\ cylinders}}{2\pi\sqrt{R_1R_2}} \qquad \text{Equation 2.3}$$

Electrostatic double layer forces result from the osmotic pressure that arises when two surfaces approach each other due to counter ions at charged surfaces in aqueous media. The balance between Coulombic forces attracting ions to the surface and the entropic drive to spread them away creates a diffuse shell of ions called the double layer [136]. The double layer thickness (also called the Debye length or decay length) is large at low ion concentrations leading to longer range and stronger repulsion between surfaces. When salt is added, the double layer is thinner and more effectively shields the charged surfaces leading to less repulsion. The thickness of the double layer can be

calculated as 1/κ, where κ, a function of the ion concentration, is described by Equation 2.4.

$$\kappa = \sqrt{\frac{e_0^2 N_A}{\varepsilon_r \varepsilon_0 kT} \sum_i c_i z_i^2} \qquad \text{Equation 2.4}$$

Where e_0 is electronic charge, N_A is Avogadro's number, c_i is the ion concentration in mol/m^3 of the ion denoted by i, z_i is the valance of the ion, ε_0 is the permittivity of free space ε_r is the solvent permittivity, k is the Boltzmann constant, and T is the temperature in K [135,137]. The double layer thickness can be used to calculate the pressure between two approaching surfaces. The force of the pressure between symmetric surfaces can be integrated to give the work of electrostatic repulsion (W_{ER}), Equation 2.5 is an approximation of the Poisson-Bolzmann equation for two flat plains and Equation 2.6 for two spheres.

$$W_{ER} = (64kT\rho_\infty \gamma^2/\kappa)e^{-\kappa D} \qquad \text{Equation 2.5}$$

$$W_{ER} = (64\pi kTR\rho_\infty \gamma^2/\kappa^2)e^{-\kappa D} \qquad \text{Equation 2.6}$$

Where ρ_∞ is the ion concentration, γ is the surface charge, D is the distance between the particles, R is the radius of the two spheres [135,138]. Figure 2.22 is a schematic of interaction energy versus inter plane distance, D, for similarly charged surfaces. The net DLVO interaction can be calculated using Equation 2.7.

$$W_{DLVO} = W_{VDW} + W_{ER} \qquad \text{Equation 2.7}$$

Figure 2.22 is shown taking into account the double layer repulsion and VDW attraction with respect to a change in surface charge density, σ [135].

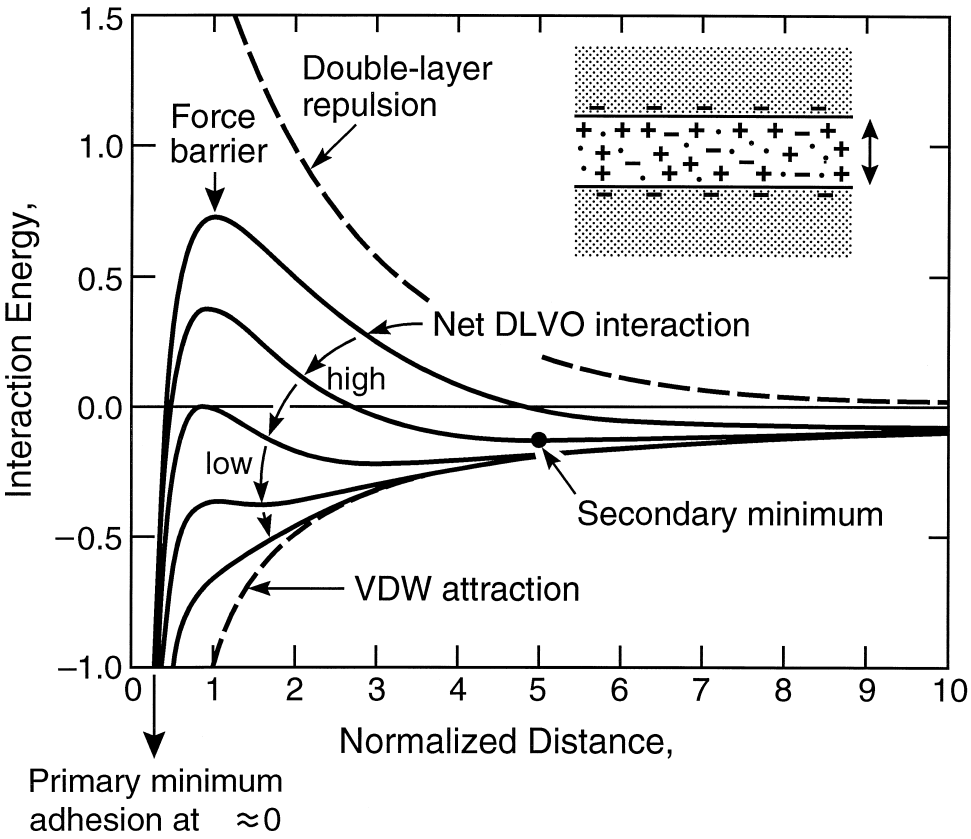

Figure 2.22: Energy versus distance profile of DLVO interactions, where interaction energy, W is proportional to the interaction area between two planar surfaces, σ is surface charge density. Reproduced from [135].

2.5.3 Adhesion

Adhesion is a complicated set of inter-connected phenomena and a fundamental property of nature that has been the subject of scientific exploration for centuries [139]. In simple terms, adhesion is the tendency of one material to cling to another, whereas the tendency of similar molecules to stick together is termed cohesion [140]. Adhesion can be caused by a variety of phenomena, ranging from chemical to structural, which are often grouped into five categories: mechanical theory, electrostatic theory, diffusion theory, adsorption theory, and weak-boundary layer theory [139,141]. Figure 2.23 schematically represents these categories; Figure 2.23a shows mechanical theory, which accounts for lock and key mechanisms also known as mechanical interlocking adhesion, which is dependent on the porosity or roughness of the surface and penetration of the

adhesive. Figure 2.23b shows electrostatic theory, which accounts for adhesion due to physisorption by surface charges and VDW forces of attraction. Figure 2.23c shows diffusion theory which accounts for adhesion due to diffusion of chain segments from one material to another bridging them together, or entanglement of surface chains and Figure 2.23d shows adsorption theory which accounts for adhesion due to the wetting of the surface and is extended to include chemical reactions (chemisorption) at interacting surfaces. Finally, weak-boundary layer theory, not shown in Figure 2.23, but similar to Figure 2.23c with smaller chains, accounts for interphase adhesion where low molecular weight species migrate to the interface which often leads to poor adhesion or adhesion failure [139].

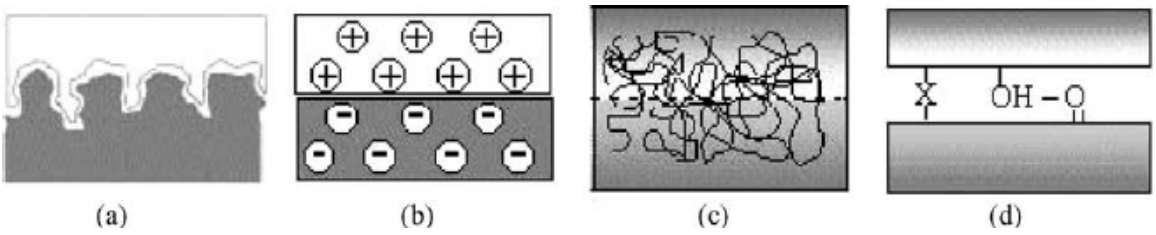

Figure 2.23: Graphical representation of adhesion theories, (a) mechanical theory, (b) electrostatic theory, (c) diffusion theory, and (d) adsorption theory. Image reproduced from [141]**.**

2.5.4 General Measurement Techniques

The first measurements of surface forces were done by Derjaguin and coworkers in the mid 1950's where the attractive VDW forces were measured between two glass surfaces. Although limited by surface roughness, these measurements where within 30% of theoretical values [142,143]. Today, there are ten common methods for surface force measurements: AFM, micro cantilever (MC), optical tweezers or optical tapping (OT), micro pipette aspiration (MPA) or bio force probe (BFP), total internal reflection microscopy (TIRM), reflectance interference contrast microscopy (RICM), surface forces

apparatus (SFA), osmotic pressure (OP) or osmotic stress (OS) and shear flow detachment (SFD). AFM, MC, OT, MPA/BFP, TIRM, and SFD, have an accurate measurement resolution for particle interactions at the micron scale, with AFM, SFA, MC, OT and MPA/BFP giving accuracy at the nanoscopic and atomic scale, whereas RICM, OP/OS are accurate only on the macroscopic scale [135]. Even though the measurement accuracy and setup of these instruments is different they follow the same underling principles where the results can be summarized using a force-distance diagram, which can be used to generate an interaction energy versus distance (or surface separation) profile as shown in Figure 2.24. Due to its precision, versatility and ability to work in most media, AFM has become a common technique for surface force measurements.

2.5.5 Colloid Probe AFM

Colloid probe atomic force microscopy (CP-AFM), a technique first developed by Ducker et al., uses a colloidal particle attached to the end of an AFM cantilever instead of a traditional pointed tip [135,144]. Using a colloid probe presents a well-defined tip geometry allowing the Derjaguin approximation (Equation 2.3) to be used to relate the interactions between the colloidal probe sphere and the flat substrate to the interaction energy between planes [135]. This allows for the normalization of forces with contact area and makes measurements comparable between systems/probes, experiments, and with theory. The larger size of the colloid probe in comparison to the traditional sharp tip allows for a more accurate measure of interaction forces as it averages over a larger area and can thus detect weaker forces. In addition, the effect of wear on the sample and probe

during CP-AFM measurements are considered negligible compared to the dulling of a tip with a nm-range radius, which indefinitely occurs.

In the first CP-AFM report, Ducker et al. used a 3.5 μm silica colloid probe to measure forces as it approached a flat silica surface in aqueous NaCl solution. The data agreed with theoretical calculations of DLVO forces at the respective salt concentrations, as shown in Figure 2.25 [144].

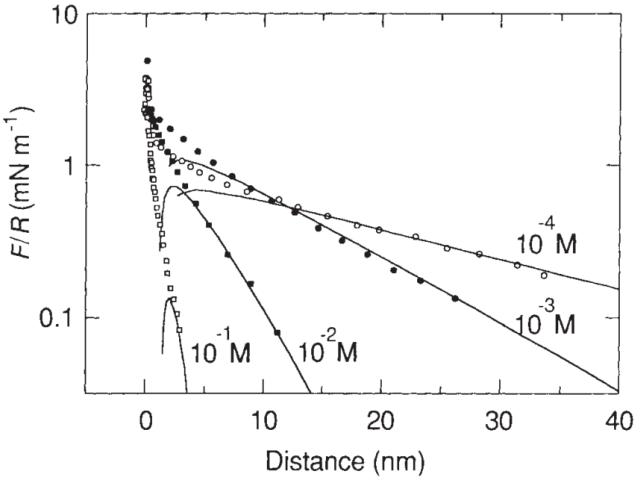

Figure 2.24: Normalized force versus distance curve for a silica sphere approaching a flat silica surface in NaCl concentrations ranging from 0.1 mM to 100 mM, where data points show measured data and solid lines show calculated DLVO forces for the respective salt concentrations. Image reproduced from [144]**.**

All AFM force measurements, including CP-AFM, rely on the AFM cantilever being ramped perpendicular (z axis) to the surface whereby positive (attractive) and negative (repulsive) cantilever deflection is recorded; this is in contrast to imaging modes where the cantilever rasters over the surface in the xy plane. The axial deflection of the cantilever is recorded with respect to the distance moved, as depicted in Figure 2.25. Upon approach, the distance between the AFM probe and the surface is decreased; the probe eventually comes into contact with the surface and upon further extension the cantilever bends. DLVO-type forces, steric forces, hydrophobic interactions, and solvation forces can be seen in the approach curve between points 2 and 3 as shown in

Figure 2.25. Upon retraction, the probe releases from the surface when the force on the cantilever is sufficient to overcome any adhesive forces between the probe and surface and the cantilever returns to its original position. The dip in the retraction curve at point 5 in Figure 2.25 indicates an adhesive force causing the cantilever to bend in the opposite direction. The deflection of the cantilever can be related to the force applied using Hook's law and assuming the cantilever is a spring with a known normal spring constant.

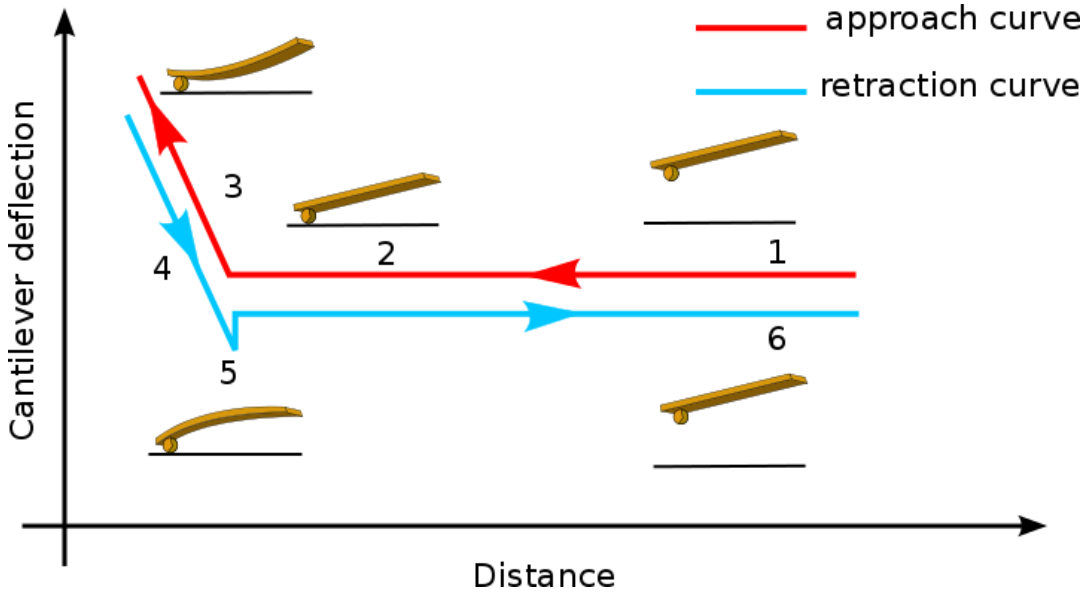

Figure 2.25: Cantilever deflection versus distance AFM force curve where the cantilever location and interaction is shown with respect to the data, 1. Probe is fully retracted from the surface, 2. The probe approaches the surface, 3. The probe is in contact with the surface and is pushed past the contact point causing the cantilever to bend, 4. The probe is beginning to retract from the surface, 5. Adhesive forces resist the retraction of the probe from surface resulting in a jump from the surface do to bending of the cantilever, 6. The probe is brought back to the original position in the fully retracted position. Figure adapted from [145].

As mentioned, in addition to DLVO forces, CP-AFM can be used to observe structuring of molecules, particles and solvents at surfaces by measuring steric interactions. A steric interaction generally manifests as a discontinuity, or jumps, in the force-distance curve. The force necessary to break or move a surface structure can be measured on the force (y) axis and the size of the feature can be estimated from the

distance (x) axis. If the feature cannot be moved or penetrated by the probe then the cantilever will bend and a "pseudo" contact point will be reached.

In one example in the literature, the influence of CTAB on the approach curves for a silica colloid and a flat silica surface was investigated by Vakarelski et al.; resistance on approach was observed which upon the application of additional force resulted in a jump to the surface. The jump distance was found to be equivalent to the diameter of two CTAB micelles, as shown in Figure 2.26 [146].

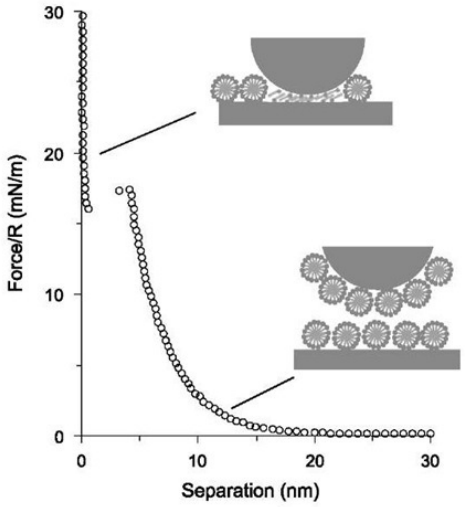

Figure 2.26: CP-AFM force versus separation approach curve for a silica colloid approaching a silica surface in CTAB solution above its CMC with a diagram showing the presence of micelles at both surfaces to explain the resistance upon approach. Image reproduced from [146]**.**

While approach curves show pre-contact surface forces, retraction curves provide information on adhesion, often seen as one or a series of pull off forces. A study by Troncoso et al. on the interactions between a silica probe and a flat silica surface in the presence of salt solutions showed that the addition of salt increased long range adhesion resulting in a large jump-from-contact force profile rather than the multiple pull off steps sometimes seen in the unfolding of proteins, DNA or untangling of polymer chains (Figure 2.27) [147].

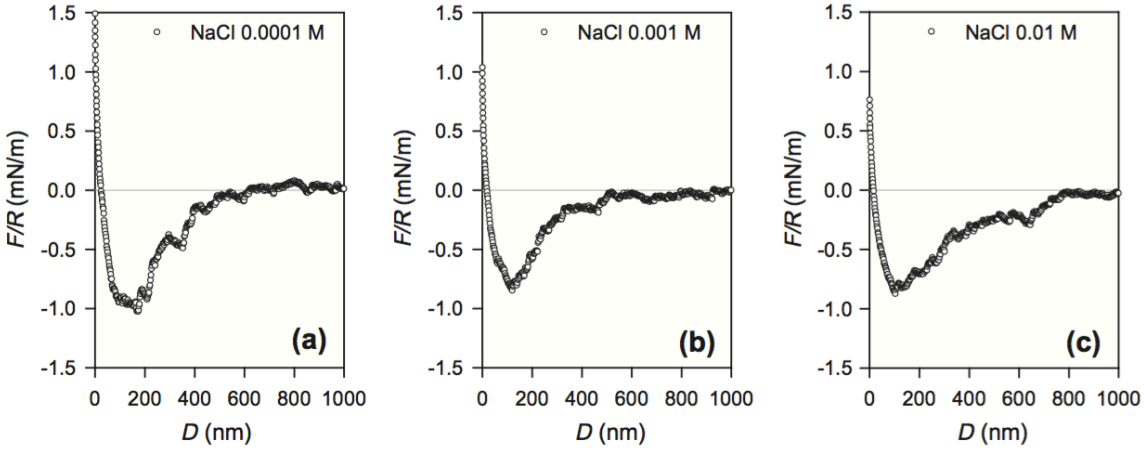

Figure 2.27: Retraction curves for CP-AFM force measurements between a silica colloid probe and a flat silica surface in the presence of (a) 0.1 mM, (b) 1 mM and (c) 10 mM NaCl. Figure adapted from [147]**.**

By understanding the interactions between materials at the micro and nano scale AFM force measurements can be used to help design new materials such as nanocomposites. For example, a study by Nordgren et al. used a cellulose colloid glued to an AFM cantilever to measure the adhesion of cellulose to cellulose and cellulose to poly(ε-caprolactone) (PCL) grafted cellulose; the results are shown in Figure 2.28. Due to the clean separation of the probe from the surface it is concluded that there is no intrinsic affinity or "chain adhesion" for PCL-grafted cellulose to cellulose [148].

In cases such as the examples described, CP-AFM measurements supply information that can be used as a screening process for material development with the advantage of using very little material and negligible damage to the test surface, which allows for multiple tests with varying conditions to be done on the same surface [148]. In addition, AFM force measurements can provide information on material interactions relevant to adhesion theories [144,148–150].

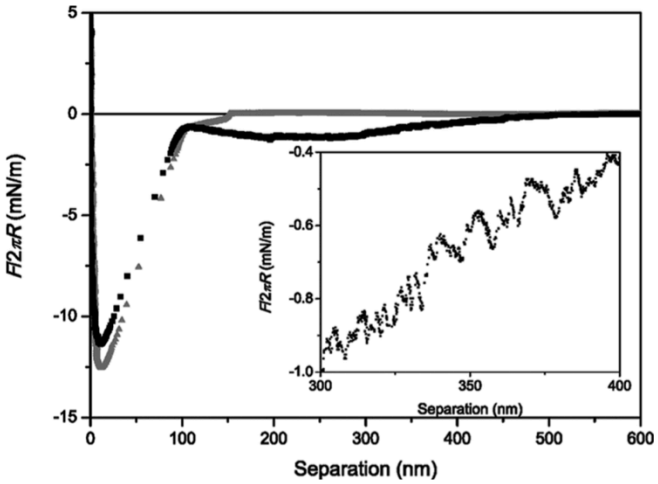

Figure 2.28: Normalized force versus separation CP-AFM curves showing pull off forces for cellulose to cellulose (in black) and cellulose to poly(ε-caprolactone) grafted cellulose (in grey). Reproduced from [148]**.**

3. Experimental

3.1 Chemicals and Materials

All solutions were made using purified water (Nano Pure, Thermo Fisher,ON) with a resistivity of 18.2 MΩ cm. Sodium chloride (NaCl), calcium chloride ($CaCl_2$), potassium hydroxide (KOH), sodium dodecyl sulfate (SDS), cetyltrimethylammonium bromide (CTAB), and triton X100 (TX100) were purchased from Sigma Aldrich (Oakville, ON). Sodium hydroxide (NaOH), and hydrochloric acid (HCl) were purchased form Caledon Laboratories Ltd. (Georgetown, ON).

Silicon wafers (<100>, boron doped, MEMC Elect. Materials, Malaysia), cut into pieces of 1 cm x 1 cm, cleaned using acidic piranha, 3:1 ratio of 95 wt. % sulfuric acid (Sigma Aldrich) to 30 wt. % hydrogen peroxide (Sigma Aldrich), copiously rinsed with purified water and dried using compressed nitrogen, were used as substrates for all AFM experiments.

3.2 Cellulose Nanocrystal (CNC) Production

3.2.1 Acid-form CNCs, Na-form CNCs and Cat-CNCs

Acid-form CNCs were made by acid hydrolysis of cellulose. Typically, 40 g of the cellulose source was hydrolyzed per batch with a 50-60% yield of CNCs. The starting cellulose material was cotton filter aid (Whatman ashless clippings, GE Healthcare, ON). To increase the surfaces area of the cellulose for the hydrolysis reaction, the filter aid, available as paper like sheets, was ground up using a kitchen blender to form smaller less dense packets. To accurately measure the mass of the cellulose, it was dried in an oven at 105 °C for 30 minutes and weighed immediately. The cellulose (40 g) was then hydrolyzed with 700 mL of 64% (w/w) sulfuric acid (prepared from 95% sulfuric acid by

dilution) at 45 °C for 45 minutes under constant mechanical stirring. This hydrolysis process grafts sulfate half esters to the surface of CNCs. Immediately following the reaction the solution was quenched by 10-fold with cooled purified water and left to settle. The solution was then decanted to remove excess water and centrifuged at 6000 rpm for 10 minutes to remove the excess acid; the formed pellet was rinsed using purified water until the supernatant was no longer transparent. Any formed clumps or pellet were re-suspended into the supernatant and put into dialysis tubes (Sigma Aldrich) with a typical molecular weight cut off (MWCO) of 12-14 000 Da. Dialysis tubes were soaked in purified water for at least 2 hours and rinsed before use. Dialysis against purified water was carried out, against 15 times more water than cellulose suspension, until the dialysis water pH remained constant, typically after 14 water changes. The resulting suspension was sonicated, using a probe sonicator (Sonifier 450, Branson Ultrasonics, Danbury, CT) at 20% output (with cooling in a ice bath), for 45 minutes in 15 minute intervals, to break up any loosely bound aggregates. The sonicated suspension was filtered, using a glass microfiber filter (Whatman grade GF/B circles, Sigma Aldrich), to remove dust and metal particles from the sonication probe tip. The concentration of the CNC suspension was then determined as a weight percent. In an aluminum weighing dish, 200 µL of the suspension by weight was dried in an oven, at a temperature of 105 °C, for 15 minutes. The weight percent was calculated by dividing the dry mass of the solution by the wet mass of the solution, accounting for the mass of the weighing dish, as shown in Equation 3.1.

$$wt.\% = \frac{M_{dry} - M_{dish}}{M_{wet} - M_{dish}} \times 100\ \% \qquad \text{Equation 3.1}$$

Where M_{dish} is the mass of the weighing dish with out the CNC solution, M_{wet} is the mass of the weighing dish with the CNC solution and M_{dry} is the mass of the weighing dish with CNC solution after drying. The final concentration of acid-form CNCs (H-CNCs) was 1 wt. %, with a pH of ~ 3, a length of 100 nm, cross section of 5 nm size, particle surface charge of -2.5×10^{8} $m^2V^{-1}s^{-1}$, and a sulfur content of 0.67 S% determined by conductometric titration.

Sodium-form CNCs (Na-CNCs) were prepared by neutralizing the H-CNC suspension, using the molar equivalent of NaOH to CNC sulfate half esters, to a point where all the sulfate ester group counter ions, i.e., protons, were replaced by sodium ions. The amount of NaOH needed was determined through conductometric titrations discussed later. The final concentration of Na-CNCs was 1 wt. % with a pH of ~7, all other aspects of the CNCs remained unchanged.

Cationic CNCs (cat-CNCs) were produced by a reaction of partially desulfated CNCs with epoxypropyltrimethylammonium chloride (EPTMAC). Anionic Na-CNCs were partially desulfated by NaOH treatment [84,151] with equal parts of 3 M NaOH to 10 wt. % CNC solution at 65 °C, in an oil bath, for 5 hours with constant stirring. The resulting product was cooled and dialyzed against purified water for at least 5 rinses to remove excess NaOH, resulting in a 2 wt. % suspension of partially desulfated CNCs (0.4 % S). The suspension was then adjusted to a pH of 13.2 using NaOH and heated to 65 °C, in an oil bath, with constant stirring while EPTMAC was added drop wise at a 1:16 ratio by mass of EPTMAC to partially desulfated CNCs. The mixture was sealed and left stirring for 5 hours. The resulting suspension of hydroxyproplytrimethylammonium chloride-modified CNCs was then diluted 5× with purified water and dialyzed to remove

NaOH and unreacted EPTMAC [152]. The final concentration of cat-CNCs was 1 wt. %, at a pH of 10 with 0.55 %N from the grafted EPTMAC, 0.4 %S residual sulfur determined by elemental analysis. The particle surface charge was 2×10^{8} $m^2V^{-1}s^{-1}$ and particle size did not show a measureable change.

3.2.2 CNC Characterization

3.2.2.1 Dynamic Light Scattering

Dynamic light scattering (DLS) measurements of 0.01 wt. % CNC suspensions with 5 mM NaCl added were made using a Zetasizer Nano-S instrument (Malvern, Worcestershire, UK) at 25 °C. The "apparent" particle diameter was recorded and the average was used as an estimate of particle size. The term "apparent" is used in recognition of the fact that DLS measures a hydrodynamic radius based on the diffusion coefficient of spherical particles and CNCs are rod-shaped particles which do not fulfill the method assumptions. DLS is used only as an internal check for batch-to-batch and CNC surface modification reproducibility.

3.2.2.2 NanoSight

Single particle tracking was done via NanoSight (Malvern) on suspensions prepared as follows: to a 0.1 wt. % CNC suspension with 10 mM added NaCl, CTAB, SDS and TX100 surfactants were added at concentrations of 0, 0.2, 0.5, 1, 2, and 4 times the critical micelle concentration (CMC), and then diluted 1000× to be suitable for NanoSight analysis (18 samples). The average particle size is reported from this method, again assuming spherical particles, similar to DLS.

3.2.2.3 AFM Imaging

Piranha-cleaned silicon wafers were spin coated (4000 rpm for 30 seconds) with a 0.001 wt. % CNC suspension and dried over night in an oven at 80°C. All samples were imaged in tapping mode using an MFP-3D atomic force microscope (Asylum Research an Oxford Instrument Company, Santa Barbara, USA). The surfaces were probed under ambient conditions using FMR cantilevers (NanoWorld Technologies, Neuchatel, Switzerland) having nominal spring constants and resonance frequencies of 2.8 N/m and 75 kHz, respectively. A "soft engage" technique, which involves alternating between manual and electronic lowing of the AFM cantilever to avoid dulling of the tip, was used to approach the sample surface. AFM data were collected and processed using the Asylum Research AFM software (version 13.15, MFP3D XOP version 20122, Argyle XOP version 20121) built on Igor Pro version 6.3 (Wavemetrics, Portland, OR, USA). AFM height images were flattened using a first order-flattening algorithm. Where applicable, ImageJ (Wayne Rasband, National Institutes of Health, USA) was used to measure feature sizes in the obtained height images. Image scale bars were used to calibrate the pixel to unit ratio for each image.

3.2.2.4 Electrophoretic Mobility/Zeta Potential

Electrophoretic mobility of CNC suspensions with surfactant concentrations of 0, 0.2, 0.5, 1, 2, and 4 times the CMC of CTAB, SDS and TX100 was measured using a Zeta Potential ZetaPlus Analyzer (Brookhaven, Holtsvile, NY). Suspensions for electrophoretic mobility measurements were prepared keeping the CNC (0.1 wt. %) and salt (10 mM NaCl) concentrations constant. CNC suspensions void of surfactant, i.e., at 0× the CMC, were used to characterize the CNCs themselves and used as a control. All

measurements were done in aqueous suspensions at 25 °C. Although the Smoluchowski model can be used to calculate the zeta potential, ζ, from electrophoretic mobility values, μ, Equation 3.2.

$$\mu = \frac{\zeta \epsilon_m V}{4\pi\eta D} \qquad \text{Equation 3.2}$$

Where ϵ_m is the dielectric constant of the solution, V is the voltage applied to the probes, η is the viscosity of the solution and D is the electrode separation, it is only valid for spherical particles with a uniform charge density and can thus overstate the ζ-potential [153]. The ζ-potential however still used as an internal check for batch-to-batch reproducibility and both the electrophoretic mobility and ζ-potential are stated for reference.

3.2.2.5 Conductometric Titration

Acid-form CNCs were titrated with NaOH to determine the sulfate half ester content on the surface of the CNCs. Conductometric titration was used to monitor the change in conductivity as CNC proton counterions are exchanged for sodium ions; conductivity leads to a more precise measure of the equivalence point than pH titrations. Typically, 0.05 g of CNC suspension (0.01 wt. %) with 75 g of NaCl (1 mM) is titrated with NaOH (2 mM) standardized with 0.01 mM HCl. The equivalence point, indicating the sulfur content as a percent, was calculated using Equation 3.3.

$$\%S = \frac{V_{NaOH} C_{NaOH} M_W(S)}{m_{CNC} C_{CNC}} \qquad \text{Equation 3.3}$$

Where V_{NaOH} is the volume of NaOH at the equivalence point, C_{NaOH} is the concentration of NaOH, M_W(S) is the molecular weight of sulfur, m_{CNC} is the mass of the CNC suspension and C_{CNC} is the concentration of the CNC suspension [85,86,154].

3.2.2.6 Polarized Optical Microscopy

Aqueous samples of CNCs (2 wt. %), on ethanol-cleaned glass slides with cover slips, were viewed under a polarized optical microscope (Nikon Eclipse LV100N POL). Digital color micrographs were obtained using an Infinity 1 color camera (Lumenera, Ottawa, ON) and Infinity Capture software (Lumenera).

3.3 Cellulose Nanofibril (CNF) Preparation

A dispersion of industrially supplied carboxymethylated cellulose micro/nano-fibrils from wood pulp (Generation 2, EG 130829, Innventia AB, Stockholm, Sweden – generously provided by Dr. Tom Lindström) described by Wågberg et al. [42], was diluted to 1 g/L with purified water using a mechanical stirrer and sonicated using a probe sonicater at 20% output, in an ice bath, for 10 minutes. The suspension was centrifuged at 6000 rpm for 60 minutes to size fractionate micro and nano fibrils. The supernatant, consisting mainly of cellulose nanofibrils, was retained. CNF films for AFM imaging were prepared by spin coating 0.001 wt. % CNF onto a Si wafer to measure particle size and dispersity.

3.4 Viscoelastic Mapping by AM-FM Atomic Force Microscopy

3.4.1 Sample Preparation and Calibration

Silicon wafers cleaned in piranha solution were spin coated (4000 rpm for 30 seconds) with 0.1 wt. % cellulose nanofibril or 0.1 wt. % cellulose nanocrystal suspensions or a 10:1 CNF:CNC mixture for amplitude modulation-frequency modulation (AM-FM) AFM imaging which provides viscoelastic and mechanical information about the sample.

3.4.2 AFM Probe Calibration and Measurement

An AM-FM/3D high frequency cantilever holder was used for AM-FM mechanical mapping experiments in the MFP-3D AFM (Asylum Research, an Oxford Instruments Company). AFM cantilevers, AC 160TS (Olympus) were tuned to their first and second resonance frequency, the "Get Real" calibration function which is built into the AFM software was used to calibrate the cantilever spring constant using the built in parameters (length 240 μm and width 30 μm). Following the calibration an autotune at the 1st resonance frequency was done and the phase was centered on the first resonance frequency and an autotune on the 2nd resonance frequency (~5.6 times the first frequency) was performed.

A "soft engage" approach, typically with a ~2 V deflection set point, was used to avoid damage to the AFM tip. Images were taken at relatively fast scan rates (1 Hz or 5 nm/s) as this AM-FM technique is extremely sensitive to tip dulling which naturally occurs with time. As usual, integral gains were adjusted to optimize for the best height and amplitude image. Specific to AM-FM, amplitude modulated (AM) drive integral gain was adjusted to optimize, to ~ 400 Hz, the dissipation retrace image and force modulated (FM) frequency drive integral gain was adjusted to optimize, to ~ 450 Hz, frequency retrace and the real-time calculation of Young's modulus retrace images. Height image integral gain was adjusted to fine tune height and amplitude images once AM and FM frequency drive integral gains were set.

Real time elasticity calculation inputs for tip geometry and radius were adjusted to calibrate the calculated Young's modulus values. SiO_2 (the substrate) was used as an internal standard during imaging whereby we assume a typical literature modulus value

for SiO_2 of ~160 GPa [155]. Images were collected at a resolution of 256 measurements per line with an image size of 5 µm.

3.4.3 Image Processing

As noted, silicon wafers were used as a reference to determine real time elastic moduli of the samples during AFM viscoelastic mapping. For quantitative analysis, the images which map the sample's Young's modulus were not flattened or processed in any way. However, other images, such as height and amplitude were flattened using a 2nd order-flattening algorithm.

3.5 Force Measurements – Colloid Probe Atomic Force Microscopy

Colloid probe AFM (CP-AFM) was used to measure normal (perpendicular) forces between a micron-sized probe glued to an AFM cantilever and the CNC films, in aqueous environments. An "open fluid cell" was used to perform these experiments by adding aqueous solution dropwise to the sample surface until a drop was formed, as shown in Figure 3.1.

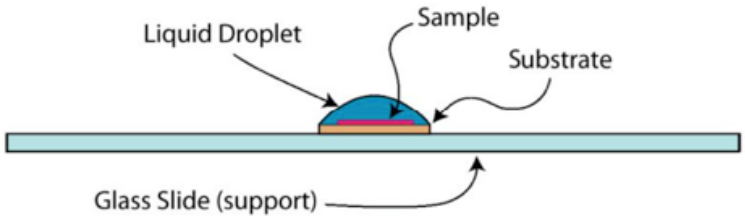

Figure 3.1: Open fluid cell setup for AFM measurements in liquid. Adapted from the MFP-3D users manual [156]**.**

Si substrates coated with CNC films were adhered to a glass slide using *First Contact* polymer optics cleaning solution (Photonic Cleaning Technologies) to prevent substrate lifting. An MFP-3D AFM (Asylum Research an Oxford Instrument Company)

was used to conduct the force-distance measurements in contact mode using the Asylum Research AFM software (Igor Pro). The "hard engage" method was used to approach the surface with a 1 V deflection set point. For normal force measurements, the tip was withdrawn from the surface and "force pulls" were collected by ramping the probe perpendicular to the substrate at a scan rate of 0.5 Hz (500 nm/s), using a trigger point of 0.8 V and an approach (pull) distance of 500 nm. All data were collected and exported using the Asylum Research AFM software.

Data for cantilever deflection *(z-z$_0$)*, a measure of cantilever bending, in volts (V) were collected as a function of distance *(z$_0$)* in µm, a typical z-z$_0$ versus z$_0$ plot is shown in Figure 3.2a. The *z-z$_0$* versus *z$_0$* data were converted to force per unit area (Force/2πR) in mN/m versus separation *(z)*, the distance between the surface and the AFM probe in nm, a typical Force/2πR versus z is shown in Figure 3.2b.

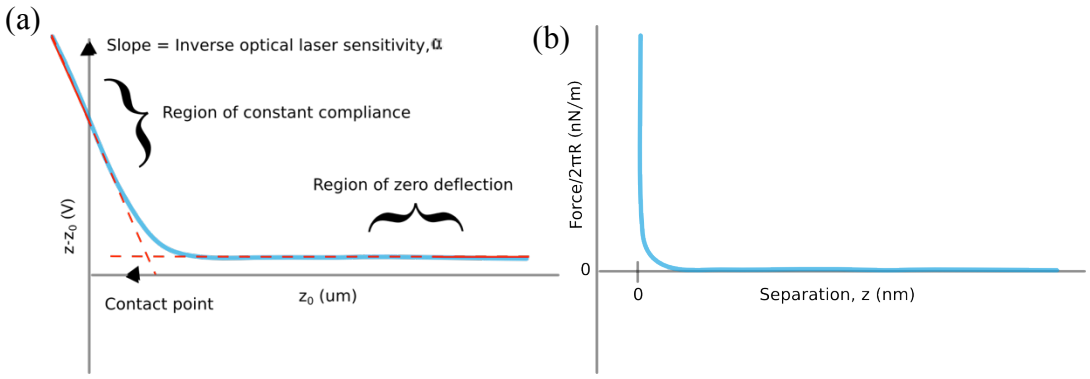

Figure 3.2: A typical force curve, (a) raw data, deflection (z-z$_0$) versus distance (z$_0$), showing the region of constant compliance, region of zero deflection, contact point and inverse optical laser sensitivity, (b) normalized and processed data, energy per unit area (Force/2πR) versus separation (z).

The contact point is the intercept of the linear fit of the region of constant compliance and region of zero deflection (identified in Figure 2a) and is used to shift the data horizontally such that the minimum separation value on the x-axis is 0. The inverse optical laser sensitivity (α in V/µm), which is the slope of the region of constant

compliance, was used to convert deflection in units of V to µm. Separation, in µm, was calculated as the sum of deflection, in µm, and distance ($z\text{-}z_{0+}z_0$). The normal force (F) between the probe and the surface was calculated using Hooke's law, Equation 3.4.

$$F = -k_n(z - z_0) \qquad \text{Equation 3.4}$$

Where k_n is the normal spring constant of the cantilever and $(z\text{-}z_0)$ is deflection in µm.

The Derjaguin approximation, for a sphere of know radius R, and a flat plane [135], Equation 3.5, was used to normalized the force data by the probe area.

$$F = 2\pi RW \qquad \text{Equation 3.5}$$

Where W, expressed as Force/2πR, is the interaction energy per unit area between a two flat surfaces. Force data were normalized by the probe diameter determined by scanning electron microscopy (SEM) and optical microscopy. SEM imaging of the cellulose colloids and cantilevers with cellulose colloids attached were taken using a JEOL 7000F SEM (JEOL Ltd., Japan) in the Canadian Center for Electron Microscopy (CCEM). Samples were sputter coated with a 5 nm gold layer prior to imaging.

3.5.1 Probe Preparation and Calibration

3.5.1.1 Silica Probes

Silica colloid probes consisted of a 2.5 µm diameter particle on a Si cantilever, with an approximate length of 280 µm and width of 20 µm and a nominal spring constant of 0.09 N/m (Novascan Technologies Inc., Ames, IA, USA). Silica probes were used as received and rinsed with water, ethanol and dried with pressurized air between measurements.

3.5.1.2 Cellulose Probes

Cellulose colloid probes were prepared in-house. Regenerated cellulose spheres (approximately 10 μm in diameter) produced by the viscose process (Kanebo, Japan) were glued to tipless triangular AFM cantilevers (PNP-TR-TL, NANO World), with a cantilever length of 100 μm, width of 13.5 μm per connecting beam and a nominal spring constant of 0.32 nN/m, using a very small amount of a two part epoxy resin (Araldite Rapid, Casco). Tungsten wires to pick up and move glue and particles were sharpened under a microscope by electro polishing in a 10 M KOH solution using a custom potentiometer setup set to 6 V. Two sharpened tungsten wires were controlled by a micromanipulator (Eppendorf Micromanipulator 5171, Hamburg, Germany) under a microscope (Olympus BX51), to maneuver glue and a cellulose sphere onto the AFM cantilever. The glue was allowed to set minimally overnight before probes were used.

3.5.1.3 Probe Calibration

Rectangular silica AFM probes were calibrated following the Sader method [157] in which the length, width, normal resonance frequency (f_0) and quality factor (Q) of the cantilever are used to calculate spring constant (k_n). Using a internet-based software [158] maintained by Dr. John Sader (Department of Mathematics and Statistics, University of Melbourne, Australia) spring constants ranged from 0.13 to 0.17 N/m (Table 3.1: S1, S2, S3), which are in reasonable agreement with the nominal value of 0.09 N/m reported by the manufacturer.

Triangular cantilevers used for cellulose probe experiments were calibrated following the thermal noise method [159] using Equation 3.6.

$$k = k_B \mathrm{T}/\mathrm{P} \qquad \text{Equation 3.6}$$

Where k_B is the Boltzmann's constant, T is the temperature in Kelvin, and P is the area of the fitted resonance power spectrum. Following this procedure, P is determined by fitting resonance power spectrum (obtained by a thermal tune) and the measured amplitude inverse optical lever sensitivity (Amp InvOLS) obtained by a single force curve. Spring constants were calculated using built in software and ranged from 0.18 to 0.3 N/m (Table 3.1: C1, C2, C3), again in good agreement with the nominal value of 0.32 N/M.

Table 3.1: Cantilever length, width, and effective height (h_{eff}), normal frequencies and quality factors.

Probe Name	Probe Type	Cantilever length (μm)	Cantilever width (μm)	Particle diameter (μm)	f_0 (kHz)	Q	Spring N/m
S1	SiO_2	280	20	2.5	26.96	47.3	0.13
S2	SiO_2	280	20	2.5	29.44	53.3	0.17
S3	SiO_2	280	20	2.5	24.78	110.4	0.15
C1	Cellulose	100	13.5 x2	19	26.90	55.7	0.30
C2	Cellulose	100	13.5 x2	18	28.89	63.6	0.18
C3	Cellulose	100	13.5 x2	15	29.08	67.9	0.27

3.5.2 Sample and Solution Preparation for Force Measurements

3.5.2.1 CNC Films

Piranha-cleaned silicon wafers were spin coated at 4000 rpm for 30 seconds with 1 wt. % H-CNCs, Na-CNCs, and Cat-CNCs to form full-coverage films. The surface coverage of the films was confirmed prior to and after CP-AFM experiments. CNC film thickness is approximately 40 nm as determined previously [160].

3.5.2.2 Salt Solutions

Solutions of NaCl and $CaCl_2$ at ionic strengths of 0.1 mM, 10 mM and 100 mM were made using purified water.

3.5.2.3 Surfactant Solutions

Solutions of CTAB, TX100, and SDS at 2 times and half the CMC of the respective surfactants where made using purified water. The CTAB solution was sonicated for 10 minutes at 25 °C to completely dissolve the surfactant.

4. Amplitude Modulated - Frequency Modulated Atomic Force Microscopy Measurements of Nanocellulose

4.1 Introduction

The mechanical properties for two types of nanocellulose, namely cellulose nanocrystals (CNCs) and cellulose nanofibrils (CNFs), were measured using amplitude modulated-frequency modulated AFM (AM-FM AFM). AM-FM AFM, as presented in Chapter 1 and 2, is a bimodal AFM technique that uses the first resonance of an AFM cantilever through amplitude modulation to image a sample surface while simultaneously using a higher frequency, typically the second resonance, through frequency modulation to generate a map of the sample material properties [129,131]. In this case, a map of the Young's modulus was generated on spin coated CNC and CNF films (on clean Si wafers) – this AFM imaging mode has not been used on nanocellulose materials before. Understanding the mechanical properties of reinforcing agents such as CNCs and CNFs is critical to the development of composites that take full advantage of nanomaterial properties. Thus this study is important as a primary step towards understand the potential of nanocellulose to impart strength to other materials through incorporation.

4.2 Mechanical Measurements of Nanocellulose Materials

AM-FM AFM was used to measure the transverse Young's modulus of CNCs and CNFs. An example measurement for CNCs is shown in Figure 4.1. A zoomed in cross-sectional analysis of the height, Figure 4.1a, and Young's modulus, Figure 4.1b, demonstrating the analysis of one CNC particle, is shown in Figure 4.1c and Figure 4.1d, respectively. The square and circle markers in the section graphs show the location of the

measurements and are identical in both the height image and the modulus map. The Young's modulus value is taken at the position that corresponds to the maximum height to reduce any measurement errors inherent to AFM imaging [58]. An average Young's modulus of 90 ± 20 GPa was measured by this method from 30 individual CNCs on three separate samples. The measured values were normalized to a reference Young's modulus of 160 GPa for Si [155] as is typically done for these types of measurements [9,129,131,161]. This is inline with values seen in the literature for CNCs which range from 50-130 GPa [48,78,162]. Part of the variability in values is because CNCs are derived from a variety of sources and measured using different techniques; in our case our CNCs are produced from cotton and are expected to have a modulus around 105 GPa [3].

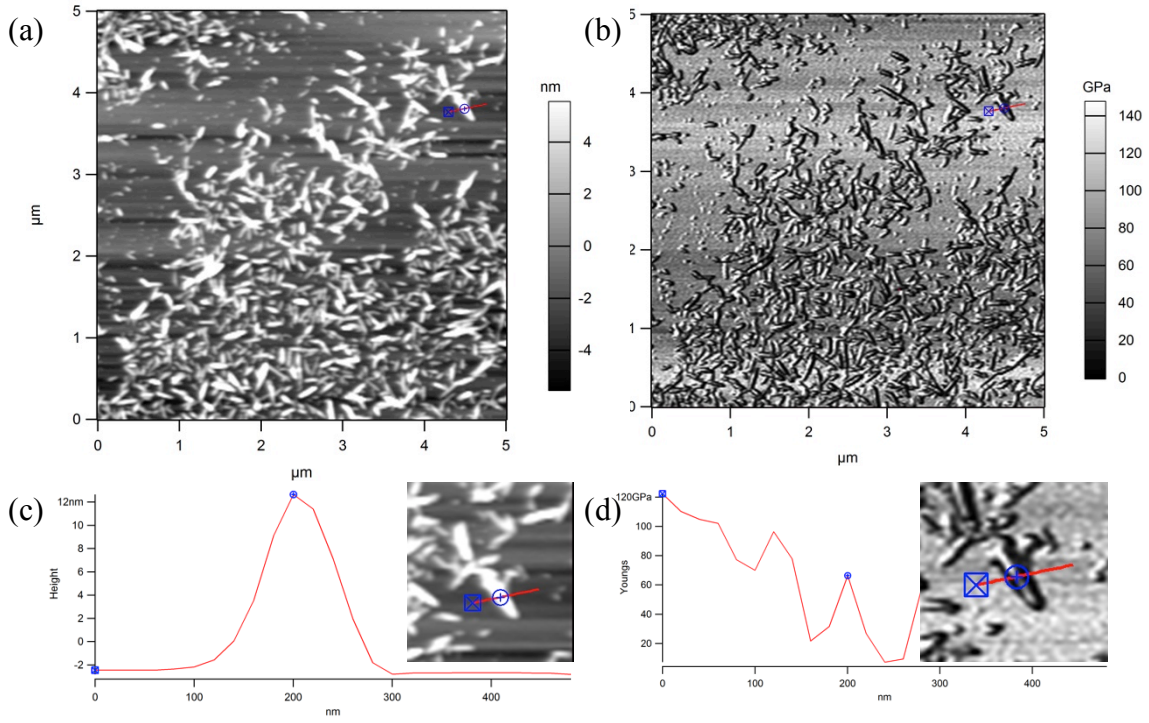

Figure 4.1: AM-FM AFM images of CNCs and corresponding section graphs to show a sample measurement: (a) AFM height image, (b) mechanical map showing the Young's modulus, (c) a section graph of the height image (d) a section graph of the Young's modulus with an inset of the zoomed in measurement location. The square and circle markers in the section graphs show the location of the measurements and are identical in both the height image and the modulus map. The Young's modulus was measured at the maximum particle height.

Figure 4.2 shows the distribution of Young's moduli obtained. Through this chart it can be seen that the Young's modulus is in the range of values reported in literature. Furthermore, outliers influence the data average but since the median, 88 GPa, is relatively close to the average we believe that the average is a good statistical representation of the measurements. These values correspond nicely with literature showing that AM-FM AFM is a relevant technique to accurately measure the modulus of CNCs.

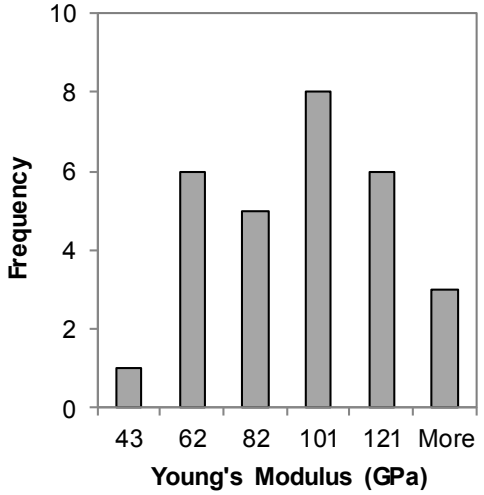

Figure 4.2: Histogram of CNC Young's modulus distribution as measured from 30 individual CNCs using AM-FM AFM.

Next, a mixture of CNCs and CNFs were spin coated together; as expected, the width of CNFs is smaller but they are longer and more flexible than CNCs and can be seen intertwined with CNCs in the lower left quadrant of the AFM image (Figure 4.3). The Young's modulus for CNFs was measured using the same method, where the height image in Figure 4.3a,c was used as a reference for the measurement of the Young's modulus in Figure 4.3b,d. The Young's modulus for the Si substrate and CNCs (determined from Figure 4.2) were used as reference to determine the Young's modulus

of CNFs. The average Young's modulus of 30 different CNFs from three separate samples was found to be 120 ± 30 GPa.

This modulus for CNFs is in line with values reported in the literature of 100-150 GPa for crystalline cellulose [162–164] but is a bit high considering that CNFs contain some amorphous cellulose alongside crystalline cellulose. Wagner et al. [165] used contact resonance atomic force microscopy (CR-AFM), a bimodal AFM technique similar to AM-FM AFM, and showed that applying the sphere cylinder contact model can give modulus values of 30 ± 10 GPa for CNCs and close to 80 ± 15 GPa for CNFs. Although these values are in the range of what was measured using AM-FM the averages are on lower end of values presented. A different AFM imaging mode that determines moduli, called Peak Force Quantitative Nanomechanical Property Imaging (QNM from Bruker), has also given lower moduli for CNCs than CNFs and in that work all values were in the 20-50 GPa range [166] which is fairly low and hence we believe AM-FM AFM is a more accurate method.

Determining the modulus for both types of nanocellulose in one image reduces variability from different AFM cantilevers, imaging parameters, and environmental conditions and makes the two values comparable, which cannot be said for many other mechanical measurement techniques. Figure 4.4 shows that the distribution of the modulus values is again broad but since the median of the data, 121 GPa is close to the average, it can be used as an accurate representation of the data.

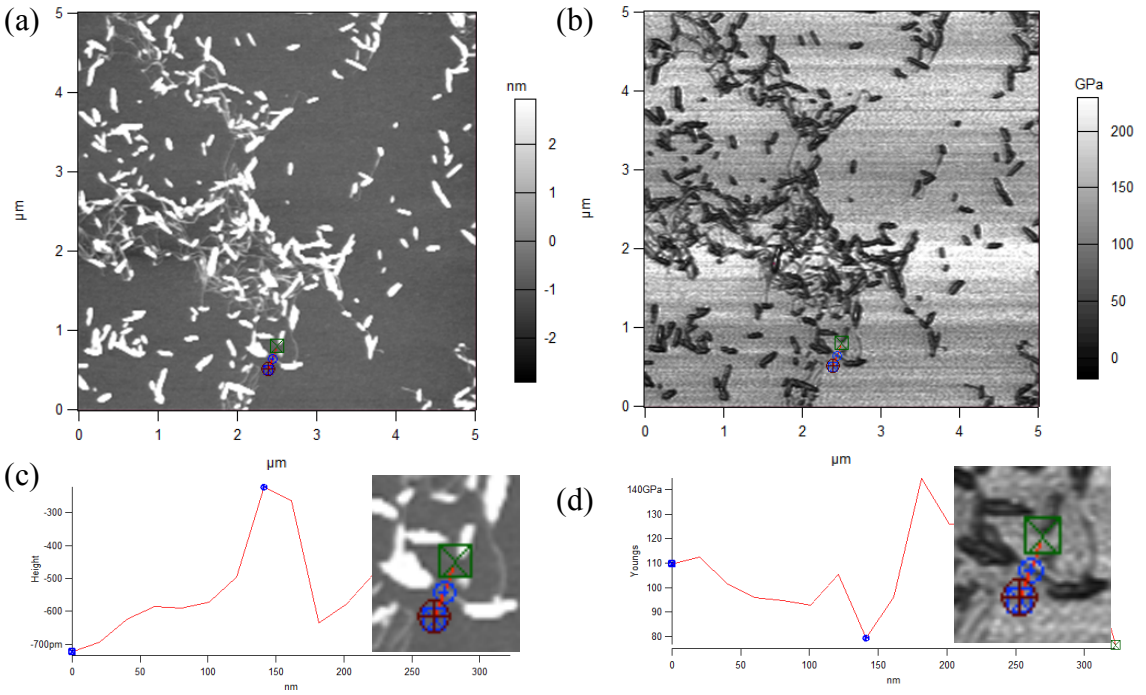

Figure 4.3: AM-FM AFM images of a mix of CNCs and CNFs and corresponding section graphs to show a sample measurement for CNFs: (a) AFM height image, (b) mechanical map showing the Young's modulus, (c) a section graph of the height image used showing the relative height of a single CNF. (d) a section graph of the Young's modulus with an inset of the zoomed measurement location. The square and circle markers in the section graphs show the location of the measurements and are identical in both the height image and modulus map showing that the Young's modulus was measured at maximum height.

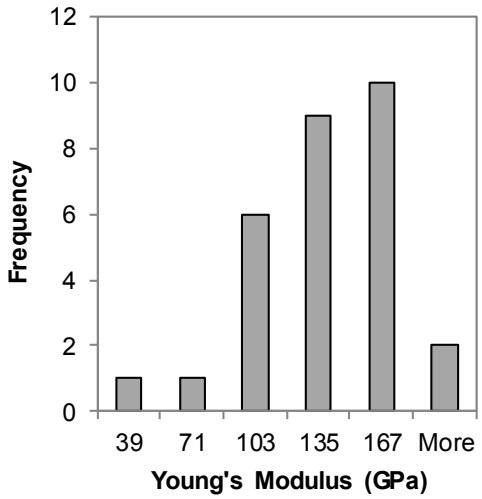

Figure 4.4: Histogram of CNF Young's modulus distribution as measured from 30 individual CNFs using AM-FM AFM.

4.3 Conclusions

These finding show that AM-FM AFM is an accurate and quick measurement tool for the determination of the Young's modulus of CNCs and CNFs. These measurements agree with modulus values in the literature implying that CNCs (90 ± 20 GPa) and CNFs (120 ± 30 GPa) have high stiffness, which is ideal for mechanical reinforcement. The AM-FM AFM technique has the potential to replace more tedious mechanical measurement methods, such as nanoindentation and dynamic mechanical analysis, and is more accurate than other AFM mechanical mapping modes reported to date.

5. Effect of Salt and Surfactants on Surface Forces in Nanocellulose Systems

5.1 Introduction

AFM in the colloid probe configuration lends itself well to understanding forces between materials of interest with extremely high precision. In this technique, a micron-sized particle probe is attached to an AFM cantilever, which is ramped perpendicular to a flat surface while cantilever deflection with respect to the distance traveled is monitored. As such, both attractive and repulsive forces in the piconewton range can be detected in air or liquid media. This chapter investigates the pre-contact interactions (i.e. *approach* force curves only) for silica-cellulose and cellulose-cellulose systems through AFM force experiments. This is done to focus on the forces between the probe and the surface as they come together without the influence of adhesion (which is measured upon *retraction* of the probe from the surface).

To investigate the pre-contact forces, two types of colloid probes were used: a silica colloid, which is smooth and negatively charged, and an amorphous cellulose colloid, which is relatively rough and uncharged (made by the viscose process) [150]. CNCs are anionic with surface sulfate half-ester groups with counterions that are either sodium ions (Na-CNCs) or protons (i.e. acid-from CNCs, H-CNCs) and in one series of measurements, CNCs were rendered cationic with surface grafted trimethylammonium groups (Cat-CNCs) [152]. The interactions between probes and spin coated CNC films were probed in salt and surfactant solution environments (a silicon wafer substrate was used as a control when needed). Salt solutions with ionic strengths of 0.1 mM, 10 mM and 100 mM for both NaCl (monovalent) and $CaCl_2$ (divalent) and surfactant solutions

with concentration of half (0.5×) and twice (2×) the critical micelle concentration (CMC) of CTAB (cationic), SDS (anionic) and TX100 (non-ionic) were used. The CMC of CTAB is 1 mM [90], SDS is 8.2 mM [98] and TX100 is 0.24 mM [100,101,103]. At least 50 force-distance curves were collected from three different regions on the CNC and Si surfaces and a minimum of 150 curves were processed from which representative curves were selected to display trends. An overlay of 100 force-separation curves is presented in Figure 5.1a to show the reproducibility of the measurements. Once the curves are shifted to "zero separation", (which is necessarily inferred in AFM measurements) these curves are indistinguishable, Figure 5.1b.

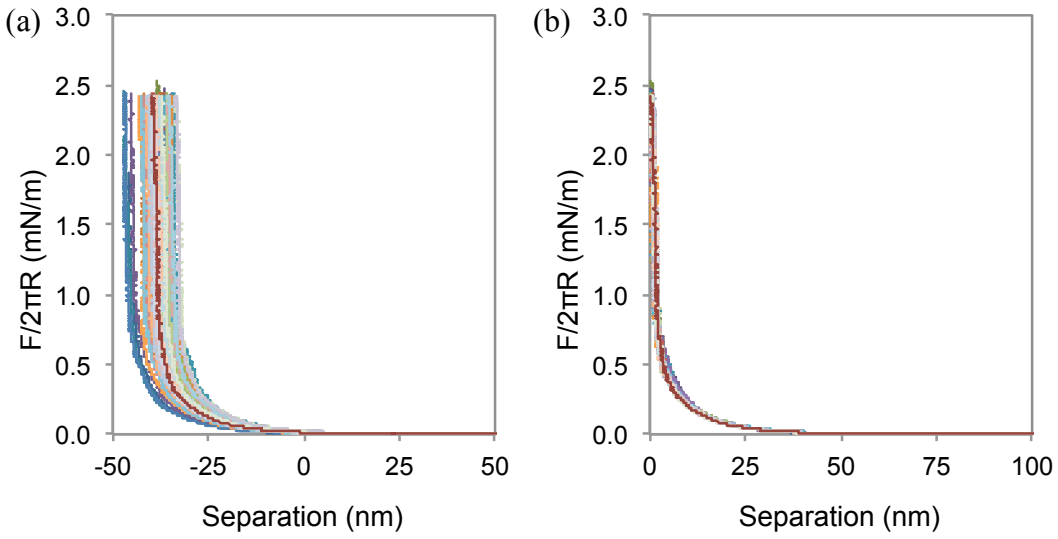

Figure 5.1: A set of 100 AFM approach force curves for a silica probe against a Na-CNC film in 0.1 mM NaCl solution showing the reproducibility of the measurements (curve shape specifically); (a) shows force curves before shifting to zero separation and (b) shows the mostly indistinguishable normalized curves.

While the AFM measurements were used to elucidate the interactions of salts and surfactants with CNC films, the same interactions were explored for CNCs in aqueous suspensions using NanoSight particle tracking analysis (NTA) and electrophoretic mobility (EM) to observe changes in CNC apparent diameter and surface potential,

respectively. These complimentary techniques suggest that what is observed by AFM can be extended to predict interactions in suspension.

By investigating the interactions of CNCs with silica and cellulose probes in the presence of salt and surfactant solutions it is possible to establish an understanding that can be used to tune the properties of composite materials and predict interactions of CNCs in emulsions, latexes, foams, gels, composite and biomedical materials. Specifically, AFM force measurements are useful for determining material compatibility and potentially predicting dispersibility of CNCs in various media and polymers. This understanding of pre-contact interactions will ideally help to streamline the development of new CNC-based materials.

5.2 Interactions between Silica Probes and Cellulose and Silica Surfaces

5.2.1 Salts

Using AFM force measurements, the pre-contact interactions between a silica probe and Na-form or H-form CNC films were measured in NaCl and $CaCl_2$ solutions. To understand the effect of salt concentration on the interactions, measurements were collected as a function of increasing ionic strength (0.1 mM, 10 mM and 100 mM). NaCl is a monovalent salt such that the ionic strength is equal to the salt concentration however, for the divalent salt $CaCl_2$, salt concentrations of 0.03 mM, 3 mM and 30 mM correspond to ionic strengths of 0.1 mM, 10 mM and 100 mM, respectively. The force curves collected in NaCl are displayed in Figure 5.2 (reminder: positive force = repulsion and negative force = attraction). In all cases, the force increases monotonically on approach; Na-CNC and H-CNC surfaces follow a similar trend whereby the onset of repulsion occurs at decreasing separations with increasing ionic strength. The CNC

counterion appears to have a small effect on pre-contact forces because the onset of repulsion and magnitude of forces are not identical for the two types of surfaces. Despite small difference, the force profiles indicate that electrostatic repulsive interactions between the anionic probe and anionic surface dominate under these conditions.

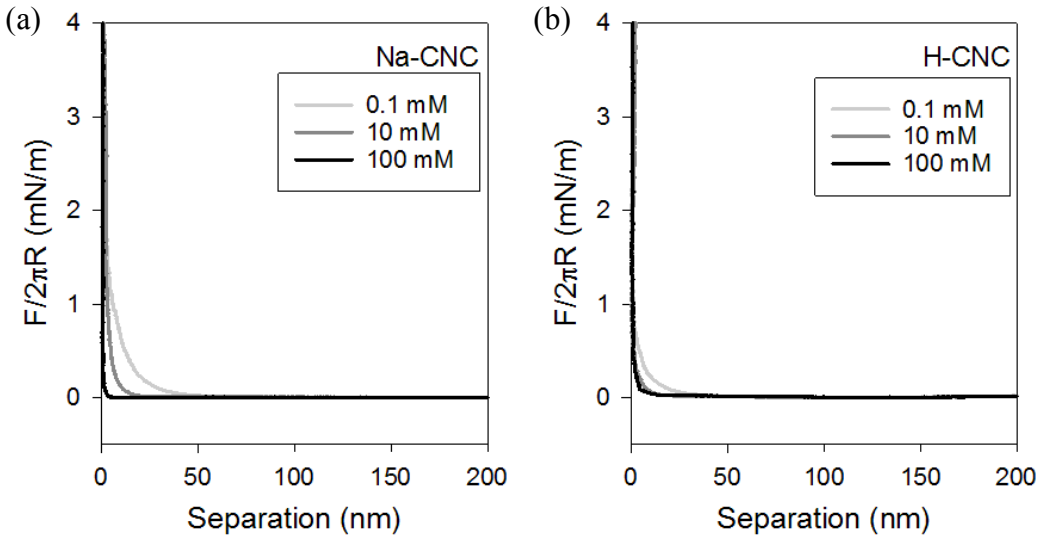

Figure 5.2: Representative AFM approach curves for a silica probe in 0.1 mM, 10 mM and 100 mM NaCl solutions against (a) Na-CNC and (b) H-CNC surfaces.

The divalent salt $CaCl_2$ was used to investigate the effect of valency on silica-CNC interactions. It is shown in Figure 5.3 that again electrostatic repulsion dominates for CNC surfaces. In some cases, the onset of repulsion decreases with increasing salt concentration (i.e. increased screening) as observed in NaCl, but not all data sets follow this trend. This may indicate that partial or full charge reversal is occurring at both the probe and the film surfaces. Since Ca^{2+} is divalent, the salt concentration required for the onset of charge reversal is less than for NaCl.

Charge reversal is a result of surface charge overcompensation by ions and generally occurs at higher salt concentrations (eg. <0.5 - 1 M for NaCl, 0.2 – 0.5 M for KCl, ~0.1 M for CsCl [167] and 40 mM for $MgCl_2$ [168]) but may occur here due to a

high *local* salt concentration near the film surface. Additionally, more acidic surfaces are expected to exhibit the onset of charge reversal at lower salt concentrations [167]. One explanation of Figure 5.3 is that H-CNC films exhibit charge reversal at lower salt concentrations (between 0.03 and 3 mM) but that the Na-CNC films exhibit charge reversal between 3 and 30 mM.

The effect of CNC counterion on pre-contact surface forces is related to how easily the counterion is displaced. According to reactivity series, the H^+ counterion is more easily displaced from the surface by other ions than the Na^+ counterion on Na-CNCs. As such, Ca^{2+} can displace H^+ on H-CNCs and not Na^+ on Na-CNCs, which may explain the difference in the force curves shown in Figure 5.3 (a) and (b) where charge reversal can be observed in H-CNCs before Na-CNCs.

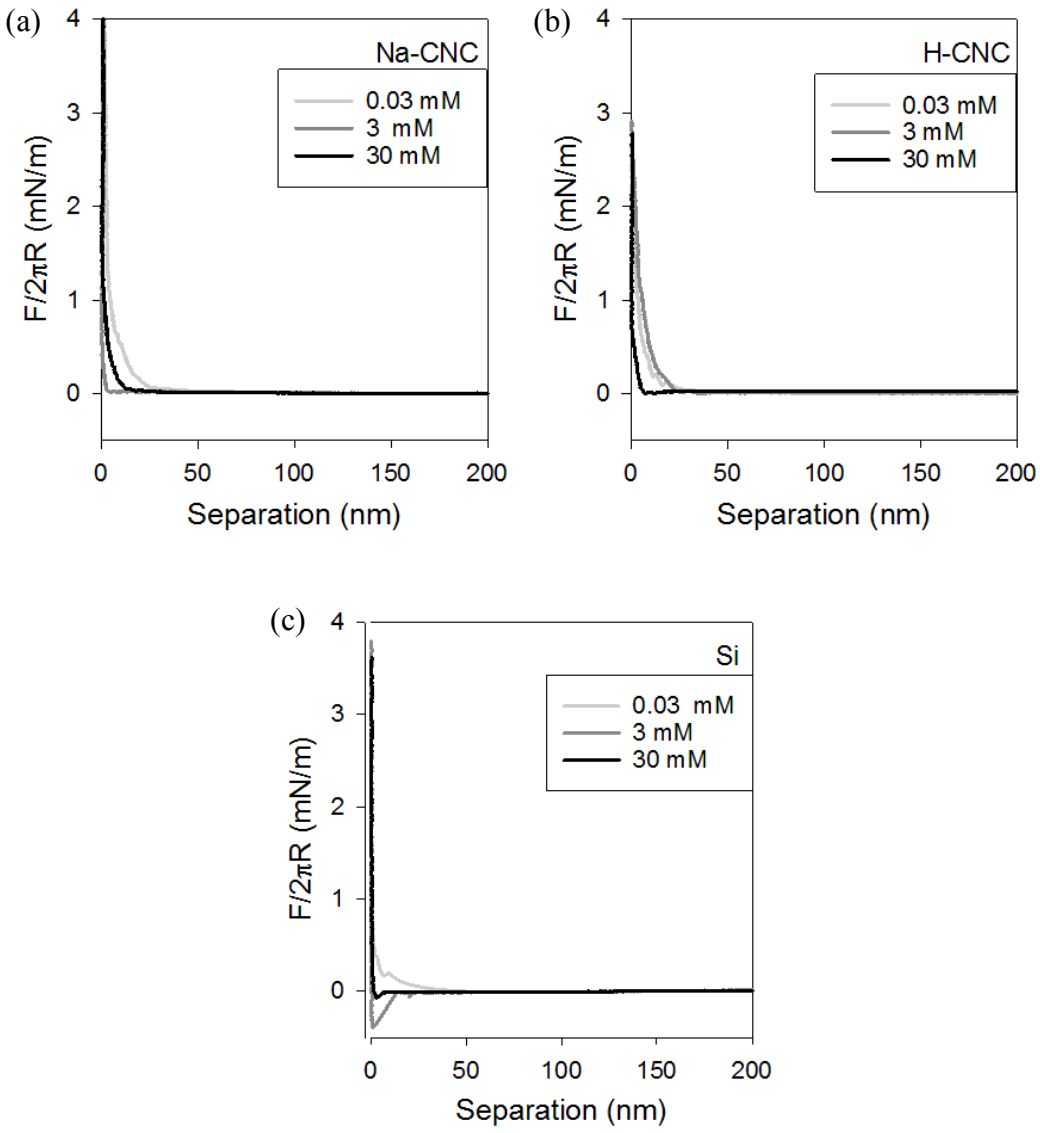

Figure 5.3: Representative AFM approach curves for a silica probe in 0.03 mM, 3 mM and 30 mM $CaCl_2$ solutions against (a) Na-CNC (b) H-CNC and (c) Si surfaces.

The Debye-Huckel approximation was used to estimate the Debye length in NaCl and $CaCl_2$ solutions. A larger Debye length indicates a lower ion concentration and vice versa. The natural logarithm of the force (which represents the interactions energy per unit area) versus separation was plotted, as shown in Figure 5.4 for a silica probe approaching a Na-CNC surface in a 0.1 mM NaCl and a 0.03 mM $CaCl_2$ environment. The curves were fit to a straight line between 10 nm and 30 nm of separation and the

Debye lengths were calculated from the negative inverse of the slope (Table 5.1). Debye lengths were not determined for ionic strengths above 0.1 mM because under such conditions the electrostatic repulsion is heavily screened until very close separations (<10 nm) making an accurate Debye length fitting difficult. In practice, the correlation coefficients (linear fit R^2 values) were generally less than 0.85 for ionic strengths over 0.1 mM and the fits are not shown here.

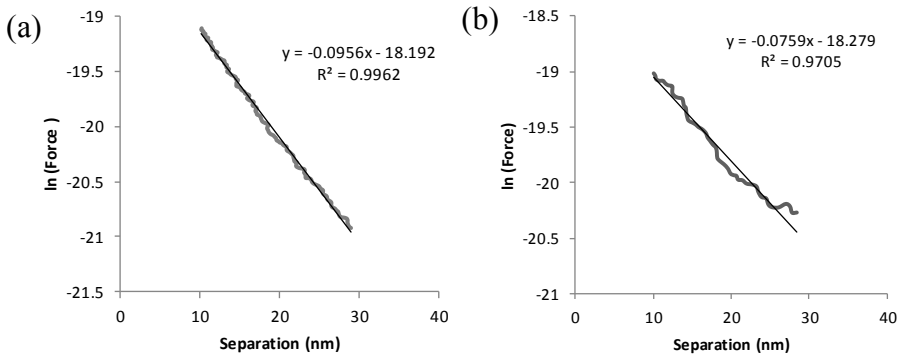

Figure 5.4: Estimation of the Debye length for a silica probe approaching a Na-CNC surface in (a) 0.1 mM NaCl and (b) 0.03 mM $CaCl_2$ environment using a linear fit applied to the curve between 10 nm and 30 nm of separation. Taking the negative inverse of the slope reveals a Debye length of 11 nm and 13.9 nm in NaCl and $CaCl_2$ solutions, respectively.

Table 5.1 shows that the Debye lengths varied minimally (9-15 nm) based on the salt type and CNC counterion. For example, the experimentally determined Debye lengths are 10.5 nm in 0.1 mM NaCl and 13.2 nm in 0.03 mM $CaCl_2$ for Na-CNC films. Theoretically, for an ionic strength of 0.1 mM, the Debye length is predicted to be 30 nm [135,169]. The measured and calculated Debye lengths are the same order of magnitude and discrepancies are attributed to the roughness of the spin coated CNC films, small ionic strength contributions from the CNC films themselves, and uncertainty in data fitting; regardless, these measurements lend themselves well to a comparison of the interactions of CNCs in NaCl and $CaCl_2$.

Table 5.1: A summary of measured Debye lengths for a silica probe approaching Na-CNC and H-CNC surfaces in 0.1 mM NaCl and 0.03 mM $CaCl_2$. The theoretical Debye length is 30 nm. Estimation of the Debye length from log-linear force curves using a linear fit as shown in Figure 5.4 in NaCl and in the Appendix Figure 5.17, Figure 5.18 in $CaCl_2$.

Surface Type	Salt and Concentration	Measured Debye Length (nm)
Na-CNC	**NaCl** (0.1 mM)	10.5
H-CNC	**NaCl** (0.1 mM)	14.7
Na-CNC	**$CaCl_2$** (0.03 mM)	13.2
H-CNC	**$CaCl_2$** (0.03 mM)	9.2

These force curves and Debye lengths are similar to those measured by Notley et al.[170] and Stiernstedt et al. [150] for model cellulose films, where increasing the ionic strength leads to screened electrostatic repulsion. Furthermore the addition of a divalent salt has been shown to increase interactions between CNCs [171] and can aid in the adsorption of proteins to CNC surfaces [172]. In our case it appears that in $CaCl_2$, charge reversal occurs for both Na-CNC and H-CNC surfaces but at a different onset. Thus it would be relevant to further investigate the interactions between CNCs (with different counterions) in a divalent salt environment.

5.2.2 Surfactants

Next, the interaction of three different surfactants (CTAB, SDS, and TX100) with three types of cellulose nanocrystals (Na-CNC, H-CNC, and Cat-CNC) was investigated. (Cat-CNCs are CNCs with a net cationic surface charge produced by a reaction of partially desulfated CNCs with epoxypropyltrimethylammonium chloride leading to CNCs with residual anionic sulfate half esters and cationic surface hydroxypropyltrimethlyammonium groups.) As expected, oppositely charged CNCs and surfactants were found to have a high affinity for each other but the interactions are not

entirely driven by electrostatics, hydrophobic interactions play a role as well [173]. In fact, we observed that while similarly charged surfactants and CNCs repelled each other, the neutral surfactant, TX100, adsorbed to most CNCs (except for H-CNCs). Many of the results presented below highlight differences in surfactant interactions with CNCs depending on the CNC counterion or the surfactant concentration.

EM and NTA were first used to test the effect of surfactant on CNCs in suspension and then AFM force measurements helped elucidate surfactant adsorption tendencies and surfactant structuring on CNC films. EM for CNCs in suspension (0.1 wt.%) is plotted as a function of increasing surfactant concentration in Figure 5.5a to measure the change in CNC surface potential. The surface potential at 0 mM surfactant is negative for Na-CNCs and H-CNCs and positive for Cat-CNCs and is expected to increase or decrease, respectively, with surfactant adsorption. Similarly, apparent diameter for CNCs in suspension (0.0001 wt.%) is plotted as a function of surfactant concentration in Figure 5.5b to track the changes in particle size – increasing particle size most likely indicates surfactant adsorption or CNC agglomeration.

For cationic CTAB, EM and NTA results show that electrostatics govern the majority of the interactions but the exact values vary considerably based on the type of CNC (Figure 5.5). Minimal change in surface potential and particle size was observed for Cat-CNCs with CTAB due to electrostatic repulsion. For anionic CNCs, the surface potential quickly increases to a plateau just above the CMC of CTAB for Na-CNCs but increases more linearly after an initial “lag” phase for H-CNCs (Figure 5.5a). From this we deduce that more CTAB adsorbs to Na-CNCs than H-CNCs and this is more apparent

at low surfactant concentrations. Similar interactions between Na-CNCs and CTAB have been observed using EM previously [113,173].

Interestingly, the increase in surface potential for Na-CNCs with surfactant addition follows the increase in particle size, however for H-CNCs the surface potential increases slower (i.e. requires higher surfactant concentrations) but the change in particle size is negligible (Figure 5.5b). This is likely due to different adsorption mechanisms (and bound surfactant morphologies), which stem from differences in the ability of CTAB to displace H^+ or Na^+, or due to the electrostatic/hydrophobic drive in solution for surfactants to adsorb vs. aggregate.

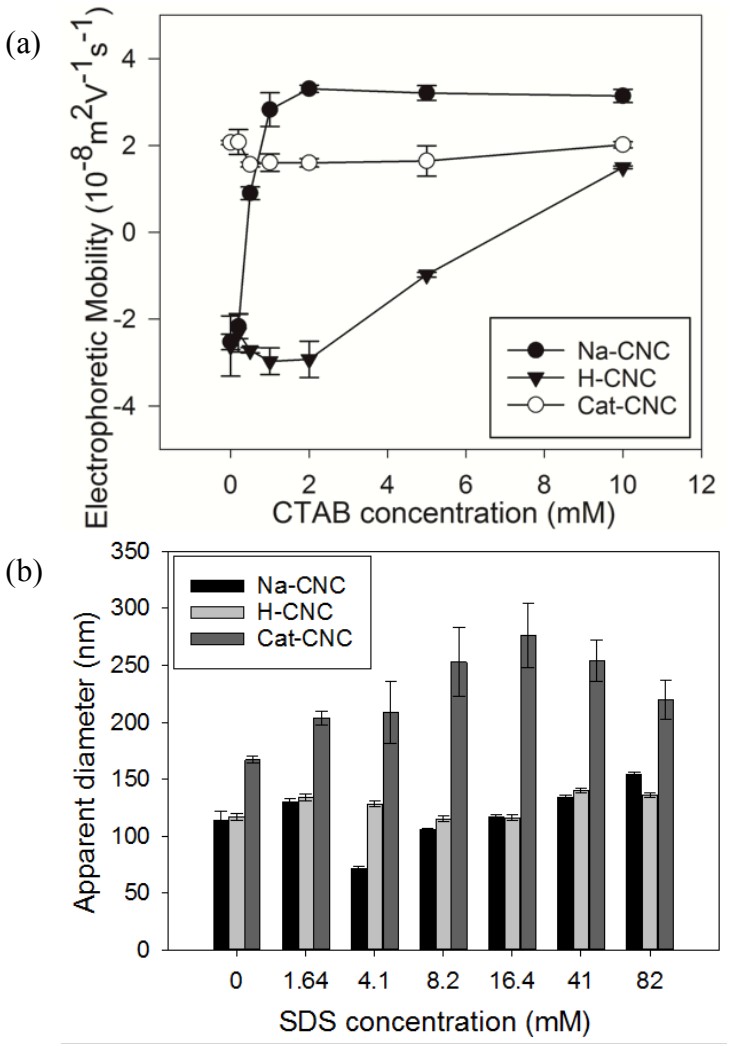

Figure 5.5: (a) Electrophoretic mobility and (b) "apparent" particle diameter measured by NanoSight for suspensions of Na-CNC, H-CNC and Cat-CNC with CTAB concentrations of a 0.2×, half, 2×, 5× and 10× the CMC with neat CNC suspensions as controls. Suspensions were diluted to the working concentrations of 0.1 wt.% CNC for EM and 0.0001 wt.% for NTA, the error bars are 95% confidence intervals.

According to the Hofmeister series, Na^+ promotes hydrophobic interactions more than H^+ [174]. We propose two (likely oversimplified) possibilities: (1) individual CTAB molecules adsorb onto CNCs and then hydrophobic "tail" interactions lead to more surfactant binding with the cationic surfactant "heads" pointed outwards (accounting for the positive surface potential shown in Figure 5.5a). The mechanism in (1) would imply significant adsorption at low surfactant concentrations and more uniform surface coverage, which might be more detectable as a particle size increase by NTA. The second

option (2) is that cationic surfactant aggregates (micelles, hemimicelles, etc.) adsorb to anionic CNCs directly leading to charge overcompensation, this mechanism would only occur above surfactant aggregation concentrations and could imply less uniform surface coverage which might not be detectable by NTA. Na-CNCs appear to follow (1) closer and H-CNCs follow (2). We attribute this to the fact that Na^+ counterions strengthen hydrophobic interactions such that surfactants adsorb to Na-CNC films due to electrostatics *and* hydrophobic interactions (potentially without displacing the Na^+ counterions), whereas for H-CNCs, the H^+ counterions are displaced by cationic CTAB molecules/aggregates [173,174].

The interactions of CTAB and CNCs were further investigated through AFM force measurements using a silica colloid probe. Spin coated CNC films were surrounded by a CTAB solution at 0.5× or 2× the CMC and pre-contact interactions were assessed from the AFM approach curves. Figure 5.6 shows that while the force increases monotonically as the probe approaches the surface (in all cases), the profiles are not typical of purely electrostatic interactions. In most cases the onset of repulsion occurs at smaller separations for higher surfactant concentrations implying that the charged surfactant contributes to the total ionic strength of species screening electrostatic interactions. However, there are additional features in some force curves, which imply soft surface contact of the probe with structures (i.e. surfactant aggregates) and steric interaction forces are detected near the surface. This “soft surface” is shown in the force curves as an initial limit to the decreasing separation (a bump in the curve), but upon the application of more force, a “jump” to contact with the hard surface is observed. An overlay of 20 consecutive force-separation curves is presented in Appendix Figure 5.21

to show the reproducibility of the measurements and the support existence of the steric features.

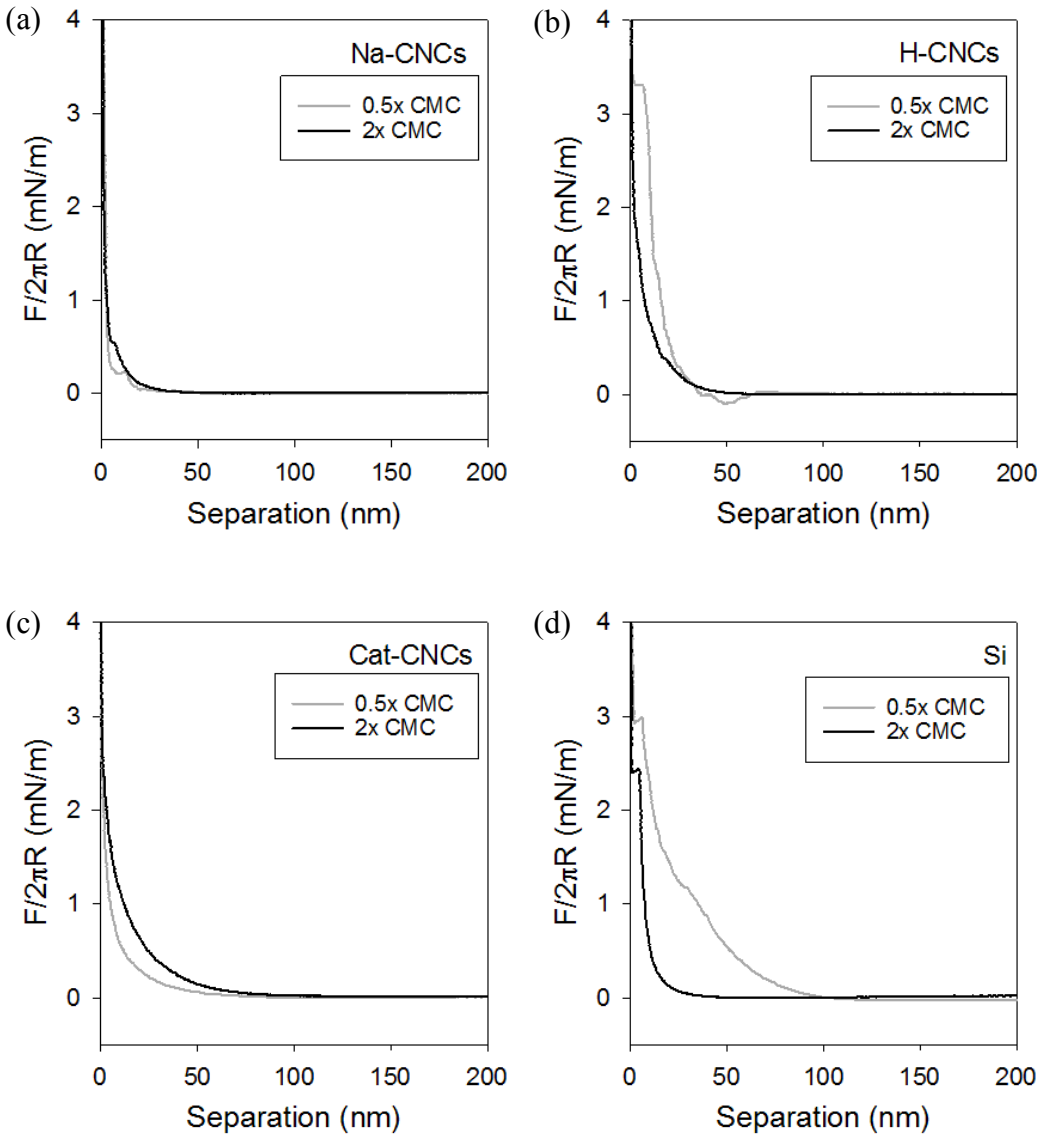

Figure 5.6: Representative AFM approach force curves for a silica probe in CTAB solutions above and below the surfactant CMC approaching (a) Na-CNC, (b) H-CNC, (c) Cat-CNC and (d) Si surfaces.

AFM force curves collected using a silica probe against the three types of CNC films and a Si wafer (control) show surfactant-cellulose affinities that support the EM and NTA results: bumps in the force curves near zero separation imply that there is adsorption of CTAB onto Na-CNCs, H-CNCs and the Si substrate (Figure 5.6a, b and d)

whereas the force profile indicates purely electrostatic repulsion for Cat-CNCs (Figure 5.6c, similar to that shown in Figure 5.2). The lack of bumps in Figure 5.6c indicates that there is insignificant surfactant adsorption to Cat-CNCs but that a cationic layer of CTAB is adsorbed on the silica probe leading to a cationic probe-cationic film interaction. The Debye lengths calculated for Cat-CNCs in CTAB are 15 nm and 17.9 nm at 0.5× and 2×CMC, respectively (Appendix Figure 5.21) which are close to theoretical values of 14 nm and 6.8 nm and discrepancies are due to the fact that due to the formation of micelles, the ionic strength is not strictly the same as the concentration of CTAB.

Figure 5.7 takes a closer look at the force curve "soft surface" features by zooming in at small separation distances and is intended to provide insight into the structuring and adsorption behavior of surfactants at the surfaces. All "soft surfaces" require a different amount of force to push through which is attributed to the stability and uniformity of the surfactant morphology. The jump-in distance is also shown to vary indicating that the features have different sizes. For Na-CNC (Figure 5.7a) in the presence of CTAB at 0.5×CMC, the bump in the force curve is at approximately 10 nm which corresponds to three times the length of a fully extended CTAB molecule [175]. Considering that there is also surfactant adsorbed on the probe, the feature in the force curve may be due to a bilayer of surfactant adsorbed on each surface (where the tails interpenetrate and thus a bilayer is less than 2 times the surfactant molecule size). This feature is very easy to push through, requiring 0.2 mN/m of force. At higher surfactant concentration (2×CMC) there is a competition between surfactant micellization and adsorption and it appears that as the probe and surface move towards each other only a

monolayer of surfactant remains bound in between. This is inferred from the smaller jump at approximately 2 nm (but this layer is harder to push through, 0.5 mN/m).

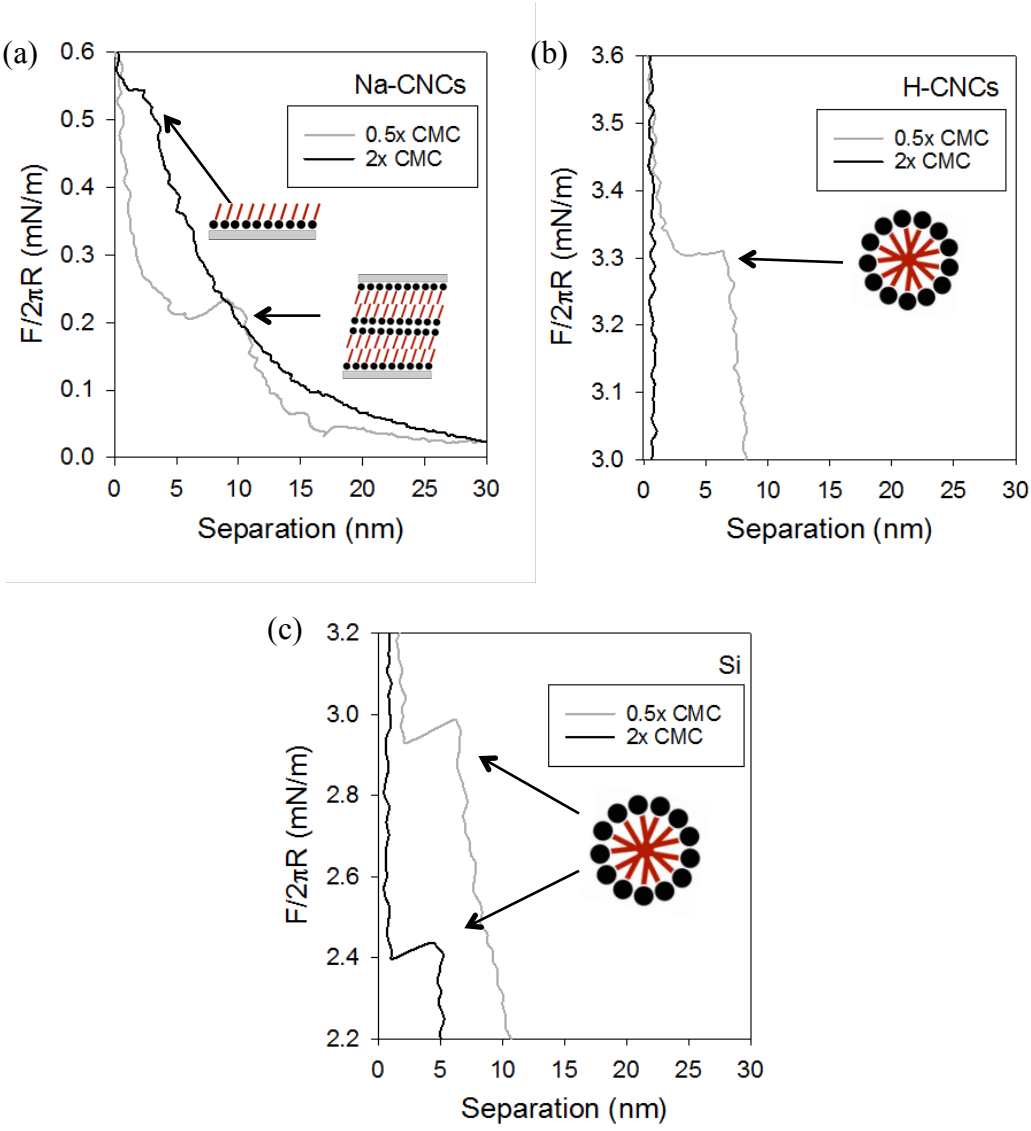

Figure 5.7: Enlarged images of the AFM approach curves for (a) Na-CNC, (b) H-CNC and (c) Si surfaces in CTAB solution above and below the surfactant CMC to highlight regions of surfactant structuring. Inset cartoons show suggested surfactant morphologies.

In Figure 5.7b for H-CNCs in CTAB at 0.5×CMC, the bump in the force curve is at approximately 6 nm which corresponds to the size of a CTAB micelle [176]. This highly ordered surfactant aggregate was found to require a significantly larger force (3.3 mN/m) to push through compared to the soft features observed on Na-CNC films. The

force is comparable to that measured by Vakarelski et al. [146] for a similar experiment with a silica probe against a silica surface in C_{12}TAB (which has the same molecular structure as CTAB but with a 12 carbon alkyl tail instead of CTAB's 16 carbon alkyl tail). The data from Vakarelski et al. is reproduced in Figure 5.8 for direct comparison to Figure 5.7c (Si surface) where the same results were obtained. The appearance of micelles below the CMC is not that surprising and has been reported previously in a review by Paria et al. [177] where similar ordering of micelles at the surface of cellulose and silica below the CMC have been observed by soft contact AFM imaging and adsorption studies. For H-CNC surfaces at 2× the CMC, no features in the force curves were observed indicating that micellization in solution overshadows adsorption and only weakly bound surfactant aggregates may be present. In general, the observations from AFM force curves support EM and NTA measurements and show that different surfactant morphologies are present depending on the surfactant concentration and the CNC counterion.

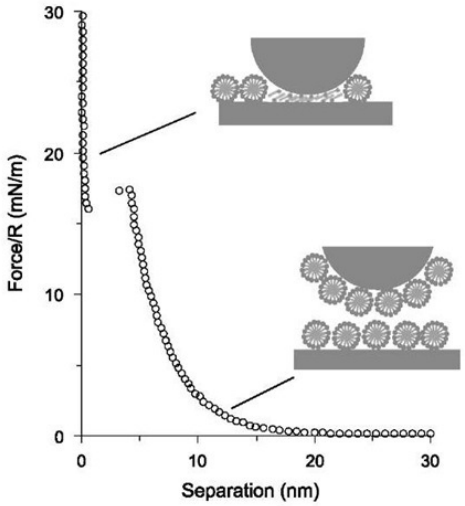

Figure 5.8: Reproduced AFM force curve data from reference [146] **showing a silica probe against a silica surface in the presence of C_{12}TAB. To make the Force/R values comparable to our work the y-axis values should be divided by 2π to give Force/2πR (i.e. their value of 18 mN/m corresponds to what we report as 3 mN/m).**

Similar to CTAB, anionic SDS also interacts most with oppositely charged CNC films, in this case, the Cat-CNCs (Figure 5.9). It is shown in Figure 5.9a through the EM experiments that Cat-CNCs switch from having a positive surface potential to negative with increasing SDS concentration. The isoelectric point occurs at 4.1 mM SDS, which is half the CMC of SDS. A similar result was shown by Prathapan et al. for Na-CNCs and SDS where the addition of SDS has no effect on the nanoparticle surface potential and the trend was insensitive to the addition of 10 mM NaCl [173]. Figure 5.9b shows that the apparent diameter of Cat-CNCs increases upon the addition of SDS, implying surfactant adsorption to CNCs, whereas Na-CNC and H-CNC particle size remains fairly constant in the presence of SDS. The size increase for Cat-CNCs with SDS is larger than would be expected from surfactant adsorption alone, however, and may be more a result of CNC agglomeration due to the surfactant and charge groups facilitating particle bridging. Analogous to Na-CNCs with CTAB, for Cat-CNCs in the presence of SDS, the onset of both particle size increase and surface potential sign change, occurs before the CMC – it appears that full charge compensation of the cationic CNC groups by SDS is easily achievable.

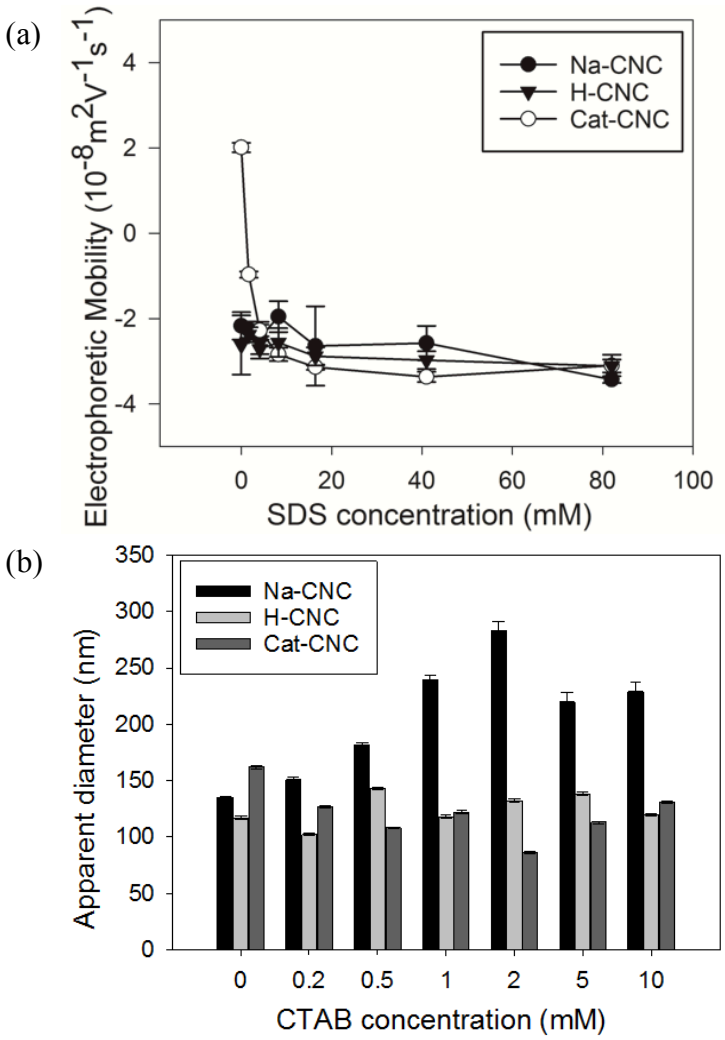

Figure 5.9: (a) Electrophoretic mobility and (b) "apparent" particle diameter measured by NanoSight for suspensions of Na-CNC, H-CNC and Cat-CNC with SDS concentrations of a 0.2×, half, 2×, 5× and 10× the CMC with neat CNC suspensions as controls. Suspensions were diluted to the working concentrations of 0.1 wt.% CNC for EM and 0.0001 wt.% for NTA, the error bars are 95% confidence intervals.

Like the EM and NTA results, the AFM force curves in Figure 5.10 imply that there is no strong interaction, adsorption or surfactant structuring near the surfaces of Na-CNC, H-CNC or Si surfaces in SDS solution (Figure 5.10a, 5.10b, and 5.10d, respectively). All force curves (except for Cat-CNC) show electrostatic repulsive force profiles between the anionic silica probe and anionic surfaces in the presence of anionic SDS. Again, SDS behaves as a salt in these situations screening electrostatics. The calculated Debye length for Na-CNCs in SDS is 6.6 nm and for H-CNC is 7.7 nm, which

are close to theoretical values of 4.7 nm and 2.4 nm, the linear fits for the Debye length are shown in the Appendix Figure 5.22.

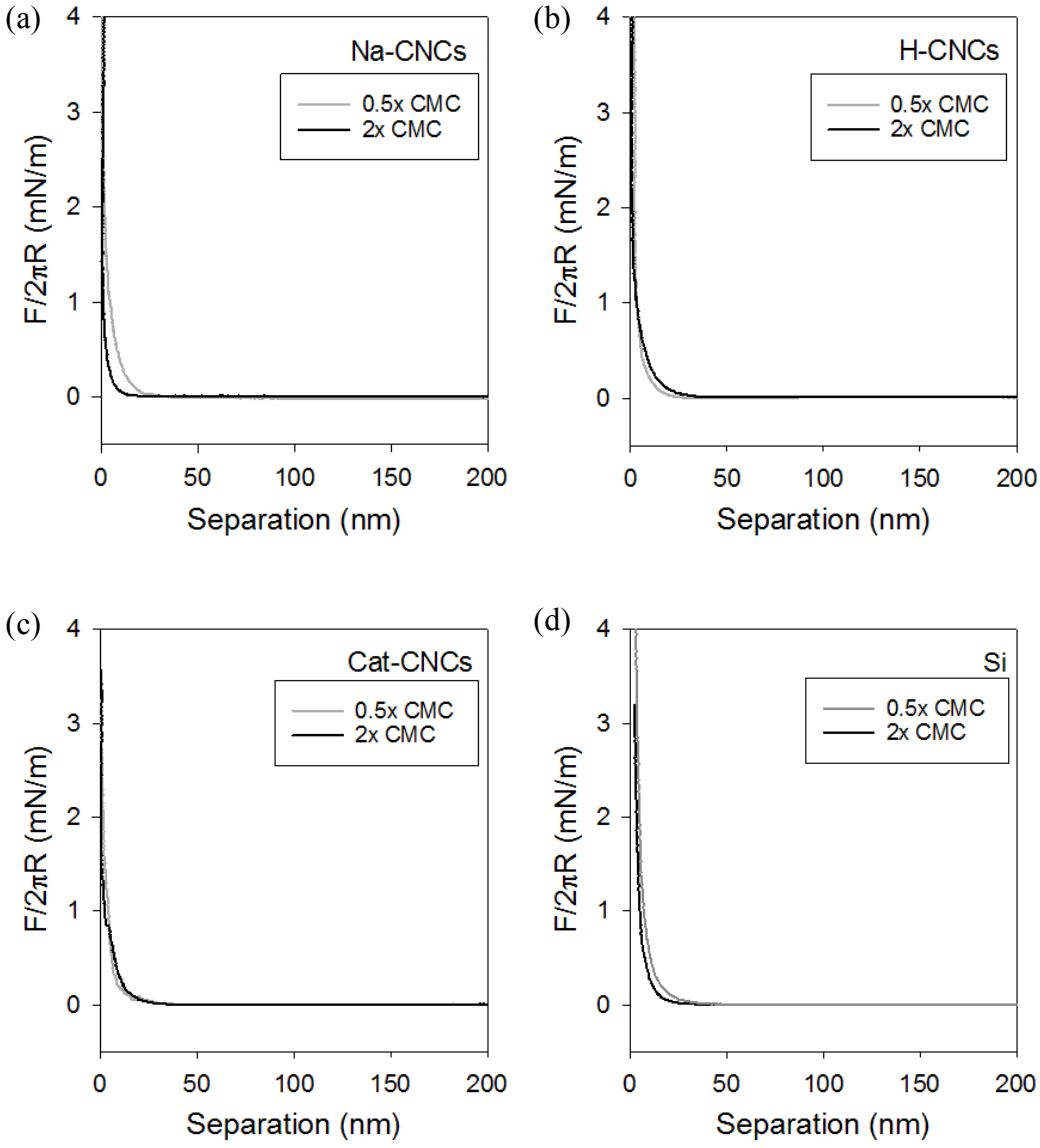

Figure 5.10: Representative AFM approach force cures for a silica probe against (a) Na-CNC, (b) H-CNC, (c) Cat-CNC and (d) Si surfaces in the presence of SDS solutions above and below the surfactant CMC.

On the other hand, Cat-CNC surfaces in SDS at 2× the CMC (Figure 5.10c) show the presence of soft surface features, which may be due to surfactant structuring. No surfactant structuring is observed below the CMC, which may be due to the small size of SDS molecules or complications arising from the Cat-CNC surface, which possesses both

anionic and cationic surface charge groups. The small jump near the zero of separation is highlighted in Figure 5.11 implying surfactant structuring of SDS on Cat-CNC films. This soft surface feature is approximately 1.5 nm wide, which is the size of a SDS micelle [178]. The small size of this steric feature is close to the resolution of the AFM force curves but did appear reproducibly in the data collected. The presence of adsorbed SDS micelles on Cat-CNC is consistent with EM and NTA experiments.

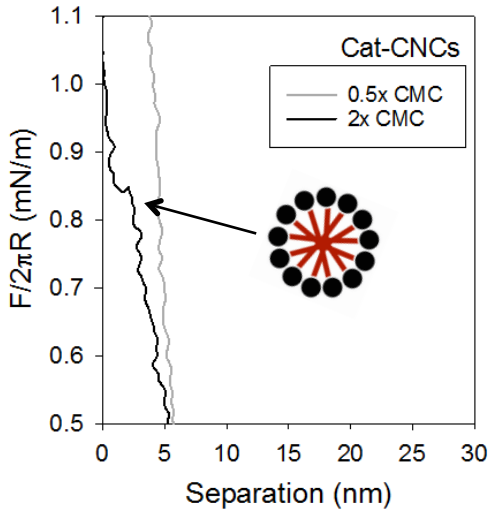

Figure 5.11: Enlarged image of the AFM approach curves for Cat-CNC surfaces in SDS solution environments above and below the surfactant CMC to highlight regions of surfactant structuring. Inset cartoon shows suggested surfactant morphology.

TX100 is a non-ionic surfactant and interacts differently with CNCs than the charged surfactants CTAB and SDS; the interactions are primarily hydrophobic in nature. Figure 5.12a shows that TX100 adsorbs to the surface of Na-CNCs and Cat-CNCs, which shields the surface charge and shifts the surface potential values towards zero. For H-CNCs there is no significant change in the surface potential indicating very little or no adsorption of TX100 to H-CNCs. Both Na^+ and Cl^- (counterion to Cat-CNCs) are ions that strengthen hydrophobic interactions based on the Hofmeister series, which implies that TX100 should prefer to adsorb to Na-CNCs and Cat-CNCs. Figure 5.12b shows that

the adsorption of TX100 to CNCs does not significantly change the apparent particle size. This is likely due to minimal (and non-uniform) adsorption and a "flatter" adsorption morphology of TX100 compared to charged surfactants on charged surfaces.

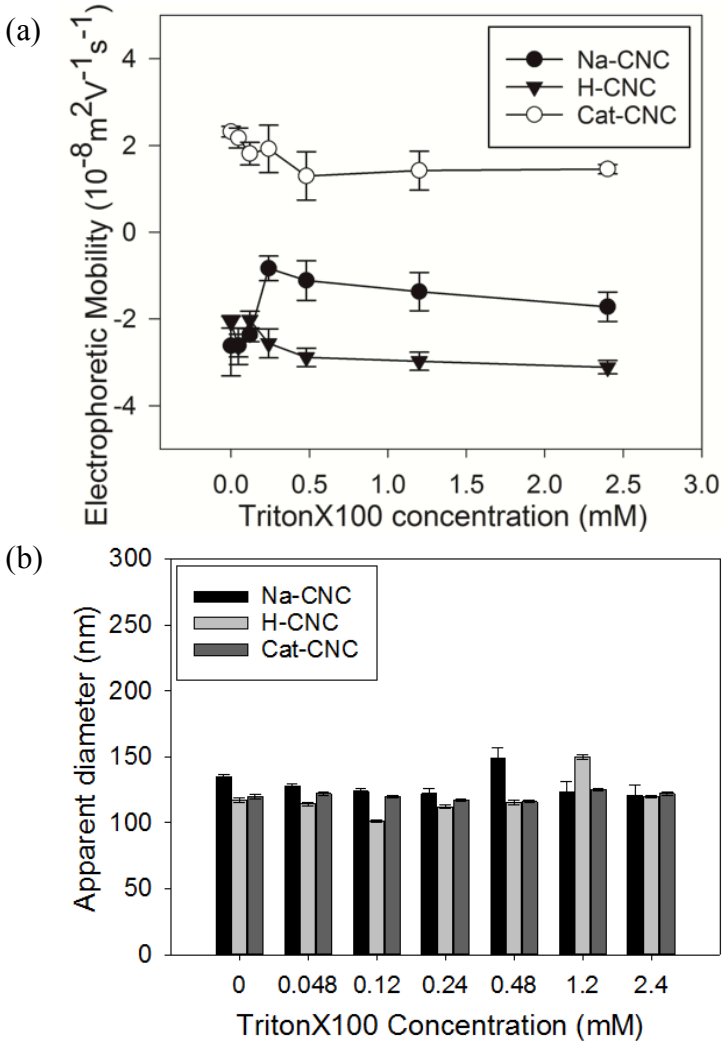

Figure 5.12: (a) Electrophoretic mobility and (b) "apparent" particle diameter measured by NanoSight for suspensions of Na-CNC, H-CNC and Cat-CNC with TX100 concentrations of a 0.2×, half, 2×, 5× and 10× the CMC with neat CNC suspensions as controls. Suspensions were diluted to the working concentrations of 0.1 wt.% CNC for EM and 0.0001 wt.% for NTA, the error bars are 95% confidence intervals.

AFM force measurements show similar affinities for TX100 to the surfaces as indicated by EM and NTA (Figure 5.13). No "soft contact" features are present on any CNC surfaces indicating that there are no surfactant aggregates and a flat sub-monolayer of TX100 would be difficult to detect by AFM. However, on silica surfaces, surfactant

structuring is present above and below the CMC, a zoomed in image of Figure 5.13d is shown in the Appendix Figure 5.23. The adsorption of surfactant aggregates, and the ability to detect them by AFM, may be enhanced on the molecularly smooth Si wafers (RMS surface roughness = 0.3 nm) compared with the rougher CNC surfaces (RMS surface roughness = 2.5 nm).

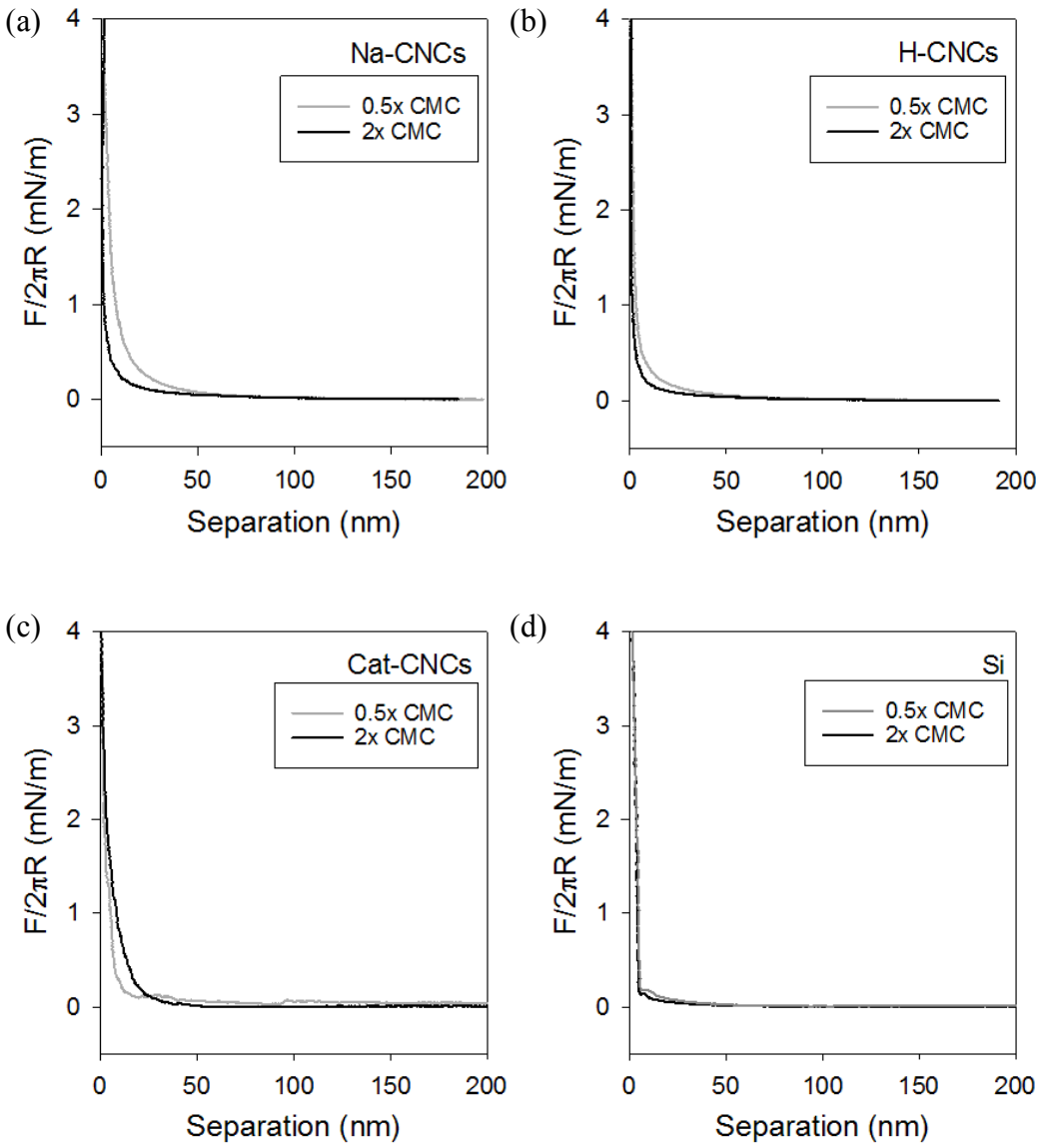

Figure 5.13: Representative approach force cures for the approach of a silica probe to Na-CNC, H-CNC, CAT-CNC and Si surfaces in the presence of TX100 solutions above and below the surfactant CMC.

Although TX100 is uncharged and does not contribute to the ionic strength of the media, it appears to screen some surface charge through adsorption. In Figure 5.13 this is manifested as less repulsion in the force curves at higher surfactant concentration. In fact, there is more surface charge screening (shown as a bigger shift between the gray and black curves) due to surfactant adsorption for Na-CNCs and Cat-CNCs when compared to the values for H-CNCs. This is consistent with the EM results that show a higher change in surface potential for Na-CNCs and Cat-CNCs than for H-CNCs. Furthermore these findings reinforce that the Na^+ counterion on CNCs promote hydrophobic interactions. This agrees with work by Zeng et al. that demonstrates how a neutral Si surface facilitates more adsorption of TX100 than a charged Si surface (shown by adsorption experiments that compare the concentration of surfactant in a solution before and after passing through a membrane) [179]. The adsorption is attributed to hydrogen bonding between the poly ethylene glycol chain on TX100 and the neutral SiOH moieties on the Si surface [179]. Furthermore it was shown that the addition of DTAB, a cationic surfactant similar to CTAB, increased the adsorption of TX100 as it binds preferentially to point charges on the Si surface and creates a more neutral surface for the adsorption of TX100 [179]. Thus we conclude that the lack of Na^+ at the surface of an H-CNC film leads to less TX100 adsorption both because it does not have a hydrophobic interaction "promoter" and presents itself as having more accessible surface charge groups in solution.

5.3 Interactions between Cellulose Probes and Cellulose and Silica Surfaces

All of the results above employ a silica probe because such probes are often favored in the literature due to low surface roughness, chemical inertness, lack of

dangling tails (which could lead to steric interactions), and known surface charge density [149]. However, as we aim to understand CNC-CNC interactions for composite applications a cellulose probe may offer more insight into the exact system of interest. Although our cellulose probes are regenerated cellulose spheres and not a crystalline rod-shaped particle we aim to deduce general trends nonetheless.

The force curves in Figure 5.14 and Figure 5.15 show that there is very little interaction of the cellulose probe with Na-CNCs, H-CNCs and Si surfaces in NaCl and $CaCl_2$, repulsion dominates, and ionic strength has a small effect. Increasing the salt concentration decreases the Debye length, shown as a shift of the vertical part of the force curve closer to the y-axis; this is comparable to what was observed by Notely et al. in AFM experiments using a cellulose probe against a silica surface [170]. It was furthermore expected, based on work by Nordgren et al., with similar neutral charge cellulose probes, that electrostatic interactions observed would be on a smaller scale than results using an Si probe [148].

There is notably significant noise in the force data in Figure 5.14 and Figure 5.15 induced by the roughness of the probe itself. For NaCl, the calculated Debye lengths from Figure 5.14 (shown in Appendix Figure 5.25) are almost identical to those with a silica probe (Table 5.1): In 0.1 mM NaCl the Debye lengths are 13.6 nm and 17.5 nm for Na-CNCs and H-CNCs, respectively (which is smaller than the theoretically predicted value of 30 nm). The Debye lengths could not be calculated accurately in $CaCl_2$. Again, the bumps in the force curves and the discrepancy in Debye length values are primarily attributed to the cellulose probe surface roughness.

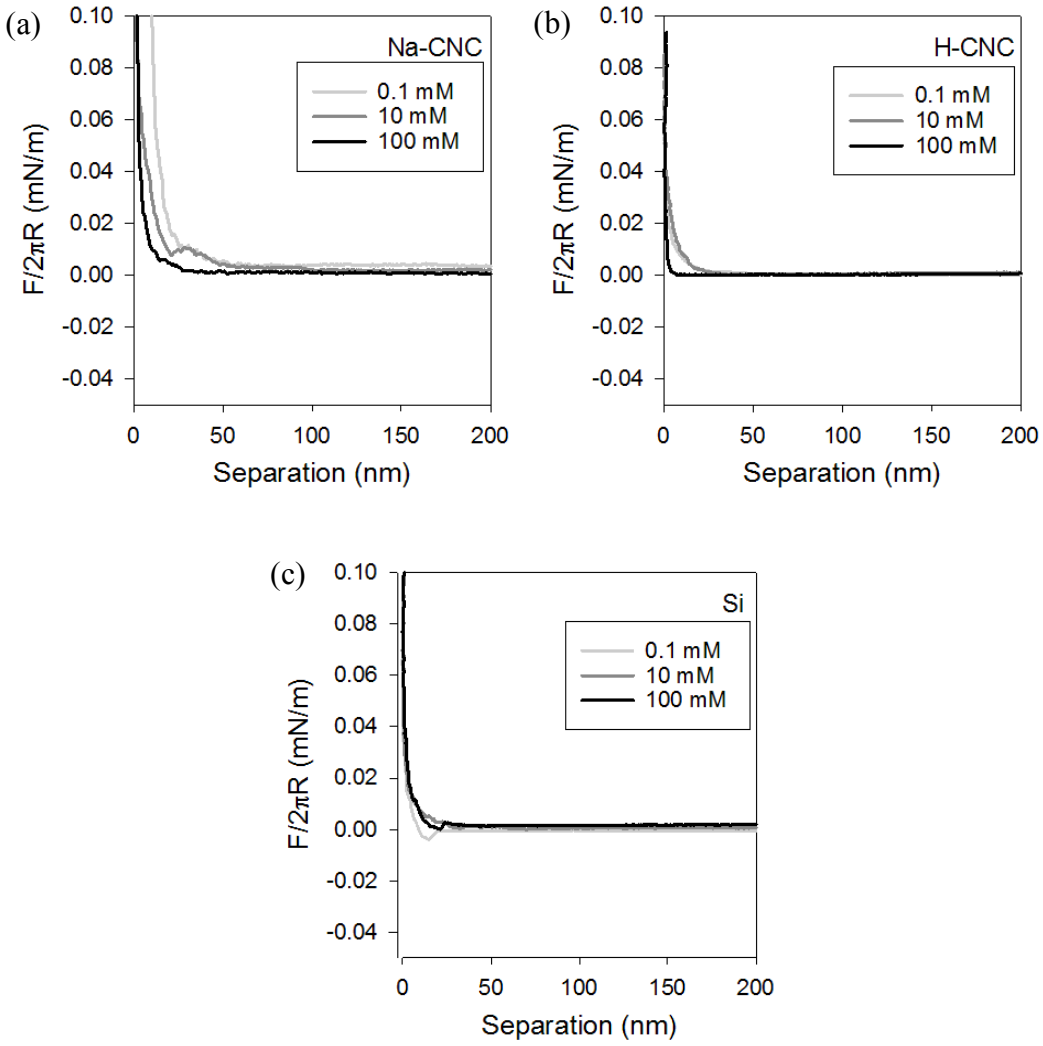

Figure 5.14: Representative AFM approach curves for a cellulose probe in 0.1 mM, 10 mM and 100 mM NaCl solutions against (a) Na-CNC, (b) H-CNC, and (c) Si surfaces.

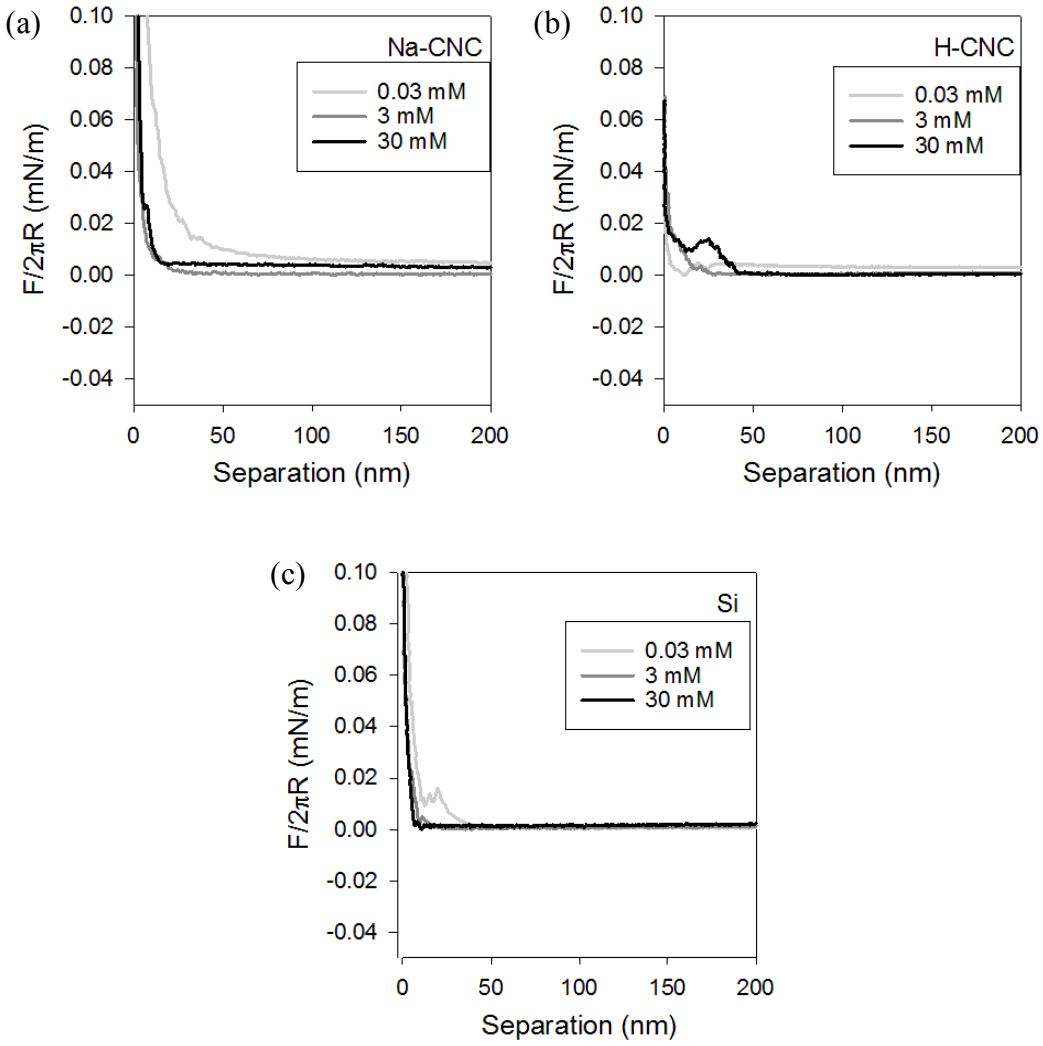

Figure 5.15: Representative AFM approach force curves for a cellulose probe in 0.03 mM, 3 mM and 30 mM $CaCl_2$ solutions against (a) Na-CNC, (b) H-CNC, and (c) Si surfaces.

Finally, cellulose probe-CNC force interactions in surfactant were collected to compare to silica probe data. As CTAB was shown in section 5.2.2 to have the greatest effect on anionic CNC interactions, we only investigated the interactions between the cellulose probe and CNCs in CTAB (SDS and TX100 experiments were omitted). Figure 5.16 shows that there is CTAB structuring at the surface in all cases below the CMC. Due to the surface roughness and neutral charge of the cellulose probe, the force needed to push through the surfactant structures is significantly lower than previously observed

with the silica probe (Figure 5.6 and Figure 5.7), and the morphology of the surfactant aggregates cannot be fully resolved. Nonetheless CTAB adsorption to Na-CNCs, H-CNCs and Si is detectable using a cellulose colloid probe.

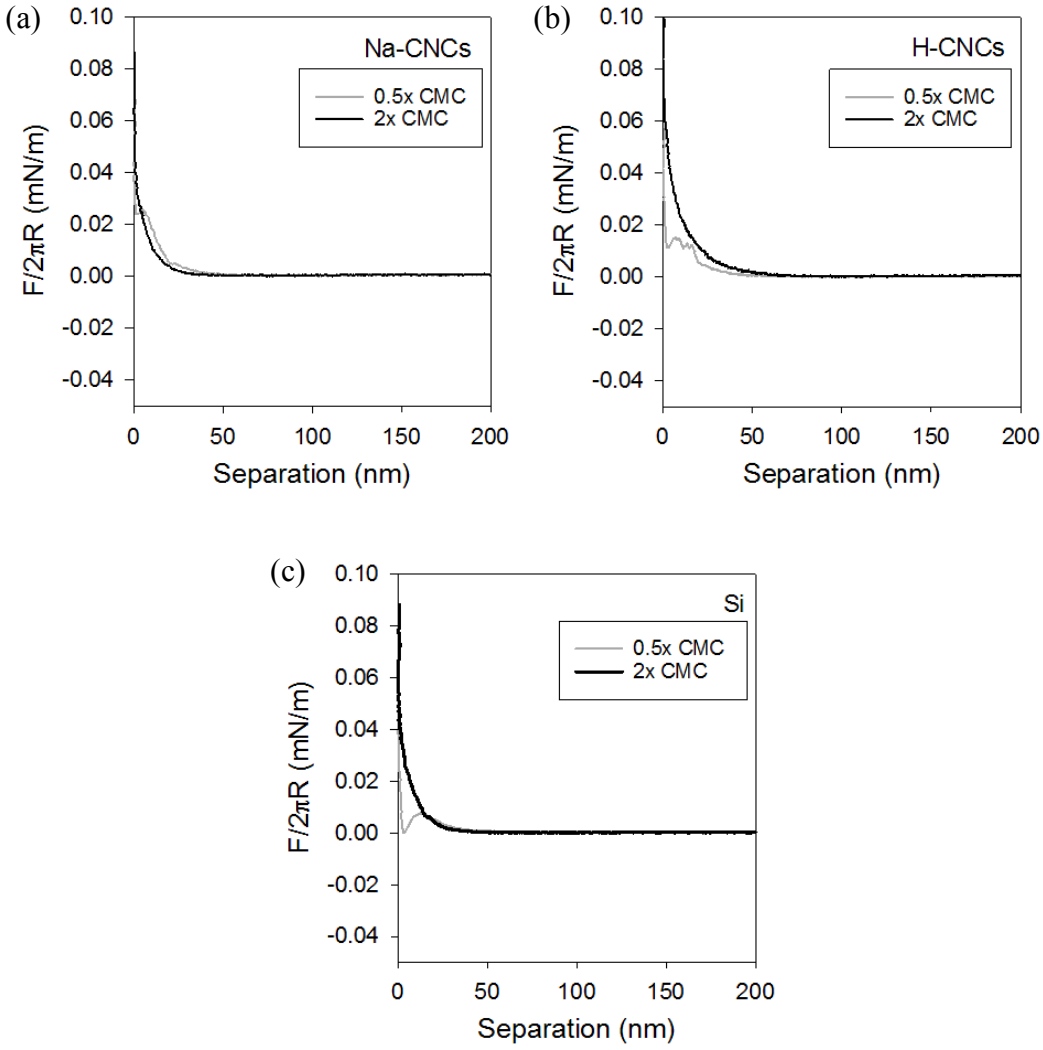

Figure 5.16: Representative AFM approach force cures for a cellulose probe against (a) Na-CNC, (b) H-CNC and (c) Si surfaces in the presence of CTAB above and below the surfactant CMC.

5.4 Conclusion

Through this investigation of CNCs with salts and surfactants, we have found that the nature of the salt/surfactant and the CNC counterion have a large effect on molecular interactions. Despite being anionic and very similar in charge density, Na-CNC and H-CNC surfaces behave differently from each other and from the Si substrate used as a control. The surface roughness of the probe and substrates affect the resolution and reproducibility of AFM force measurements as well as influence the morphology of adsorbed surfactants.

When comparing the interaction of Na-CNC and H-CNC with salts and surfactant, it is inferred that H^+ is more easily displaced by other counterions and Na^+ likely promotes hydrophobic interactions (in addition to electrostatic interactions). For example, we show that the exchange of H^+ to Na^+ leads to higher salt concentrations required for the onset of charge reversal. Electrostatic repulsion between anionic probes and anionic CNC surfaces in salt are measured, as expected, and the determined Debye lengths are on the right order of magnitude compared with theory.

In surfactant solutions, the surfactant charge and concentration, and CNC type and counterion, led to a variety of proposed adsorption morphologies. According to NTA only (i) CTAB with Na-CNCs and (ii) SDS with Cat-CNCs led to significantly larger particles despite the fact that all oppositely charged surfactant-CNC combinations showed that surfactant adsorption modified the surface potential. TX100 adsorbed to most CNC surfaces due to hydrophobic interactions. Monolayer and bilayer surfactant morphologies are inferred from AFM force curves for Na-CNCs with CTAB and micelle adsorption is observed in H-CNCs with CTAB and Cat-CNCs with SDS systems, which

highlights the intricacies of surfactant interactions. These measurements just begin to elucidate the competing factors at play with surfactants and CNCs such as electrostatic, steric and hydrophobic interactions, ion reactivity and the drive for micellization. In conclusion, since the CNC surface charge and counterion has such a large effect on molecular interactions, it is important to consider (and report the starting material specifications in publications) when looking at the interaction of CNCs and potential composite materials.

5.5 Appendix

5.5.1 Silica Probe Interaction in Salt Solutions

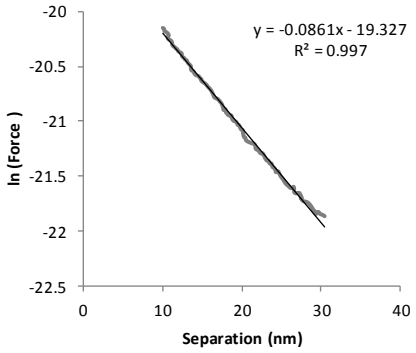

Figure 5.17: Estimation of the Debye length for a silica probe approaching a H-CNC surface in 0.1 mM NaCl using a linear fit applied to the curve between 10 nm and 30 nm of separation.

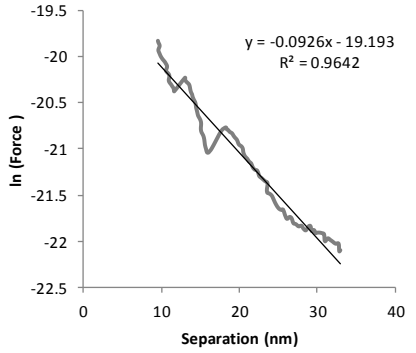

Figure 5.18: Estimation of the Debye length for a silica probe approaching a H-CNC surface in 0.03 mM $CaCl_2$ using a linear fit applied to the curve between 10 nm and 30 nm of separation.

5.5.2 Silica Probe Interactions in Surfactant Solutions

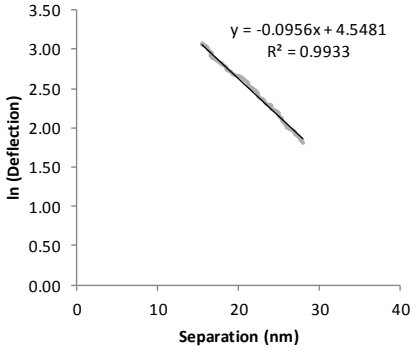

Figure 5.19: Estimation of the Debye length for a silica probe approaching a H-CNC surface in a 2× CMC CTAB environment using a linear fit applied to the curve between 10 nm and 30 nm of separation.

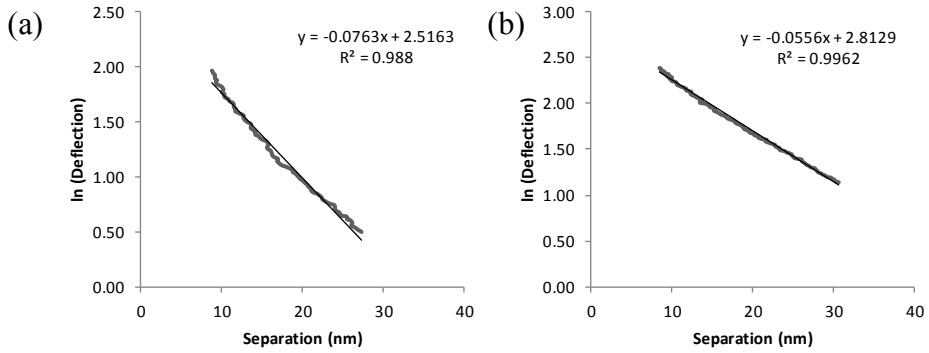

Figure 5.20: Estimation of the Debye length for a silica probe approaching a Cat-CNC surfaces in (a) 0.5× CMC and (b) 2× CMC CTAB environment using a linear fit applied to the curve between 10 nm and 30 nm of separation.

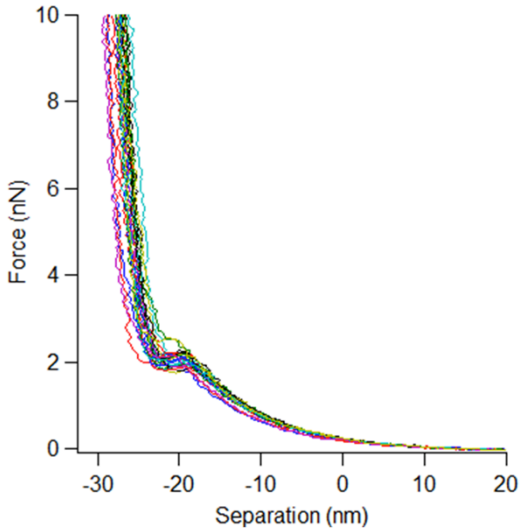

Figure 5.21: A set of 20 approach force curves for Na-CNC surrounded by CTAB solution at 2× CMC. It is evident from these measurements that the jump from contact with a soft surface to a hard surface can be measured reproducibly by colloid probe AFM force measurements.

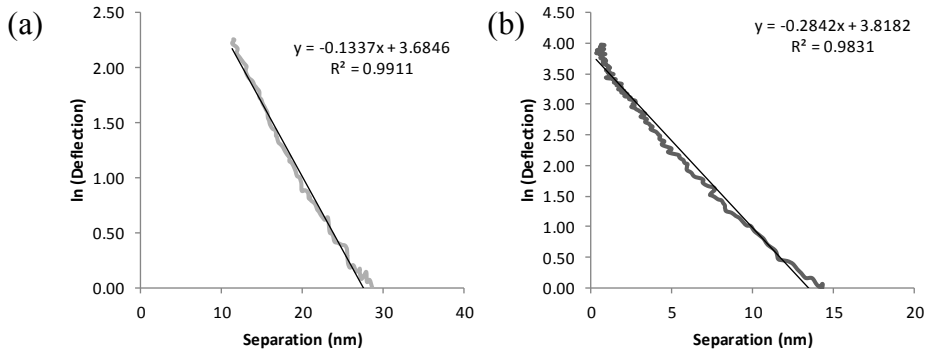

Figure 5.22: Estimation of the Debye length for a silica probe approaching a Na-CNC surface in (a) 0.5× and (b) 2× the CMC of SDS environment using a linear fit applied to the curve between 10 nm and 30 nm of separation.

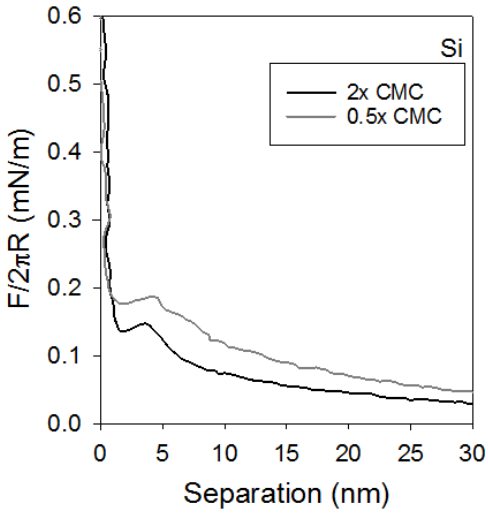

Figure 5.23: Enlarged image of the approach curves for Si surfaces in TX100 above and below the surfactant CMC to show regions of surfactant structuring.

5.5.3 Cellulose Probe Interactions with Salt

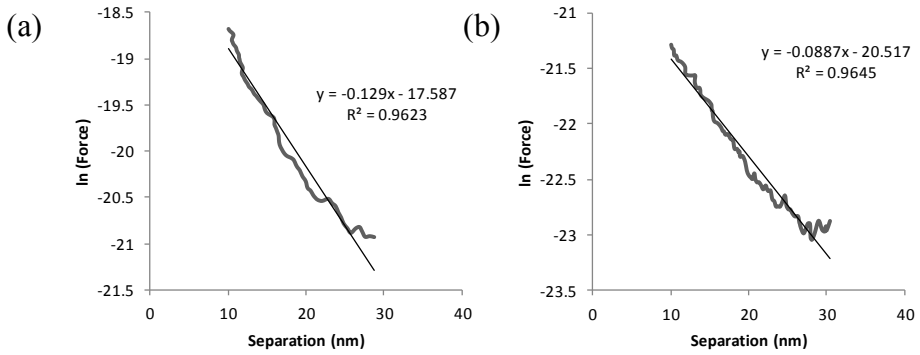

Figure 5.24: Estimation of the Debye length for a cellulose probe approaching (a) Na-CNC and (b) H-CNC surfaces in 0.1 mM NaCl using a linear fit applied to the curve between 10 nm and 50 nm of separation.

6. Adhesion in Nanocellulose Systems Measured by Colloid Probe AFM

6.1 Introduction

In the previous chapter the pre-contact forces from an AFM probe moving towards a spin-coated CNC film (i.e., *approach* curves) were discussed. In this chapter the *retraction* of a probe from those same surfaces is shown. It will be discussed how the pre-contact forces and surfactant morphologies inferred in Chapter 5 affect adhesion, or the lack there-of, upon the retraction of the probe away from the surface.

AFM colloid probe force measurements were done where the probe and surface were immersed in either salt or surfactant solutions. The two salts used were monovalent NaCl at molar concentrations of 0.1 mM, 10 mM, and 100 mM and divalent $CaCl_2$ at the equivalent ionic strength, which corresponds to molar concentrations of 0.03 mM, 3 mM and 30 mM. Surfactant solutions used were made at concentrations of half (0.5×) and double (2×) the CMC. Where the CMC of CTAB is 1 mM, SDS is 8.2 mM and TX100 is 0.24 mM. Overall, CNC adhesion is affected by the liquid environment and surfactants have a strong ability to compatibilize surfaces and increase adhesion which is significant in CNC nanocomposite design.

6.2 Interactions between Silica Probes and Cellulose and Silica Surfaces

6.2.1 Salts

The effect of salt on silica-cellulose adhesion was investigated by looking at the retraction portion of the same AFM force curves discussed in Chapter 5. Due to the charged nature of the CNCs and silica surfaces, salt will screen electrostatic repulsion, which may increase adhesive interactions. It was shown in Chapter 5 that the increase in

salt concentration increased the screening of electrostatic repulsion. It is thus expected that increasing salt concentration will increase the adhesion as it is widely accepted that the addition of salt can lead to destabilization of DLVO forces and the aggregation of particles in a suspension. Ideally, studying the interactions between a probe and a film offers insight into colloidal interactions in suspension but furthermore may be useful for understanding CNC coatings.

In addition to salt altering pre-contact surface forces between silica/cellulose probes and CNC surfaces, Chapter 5 showed that the type of counterion on CNCs, either H^+ or Na^+ had a larger influence on surface interactions than expected. Similarly, the liquid environment around this system and counterions affected adhesion (i.e., post-contact forces). An example of a retraction force curve is shown in Figure 6.1. The adhesion is manifested as a dip below the zero-force line (y axis) followed by a "jump" in the curve back to zero force. The "jump" occurs at the separation (x axis position) where the force exerted by the retracting cantilever is sufficient to overcome the force of adhesion between the probe and surface. Multiple bumps in the force curve upon retraction are characteristic of various detachment events or conformational changes, and often such curves are used to look at protein/DNA unfolding, single molecule forces or adhesives with multiple contact points between the adhesive and the probe [180].

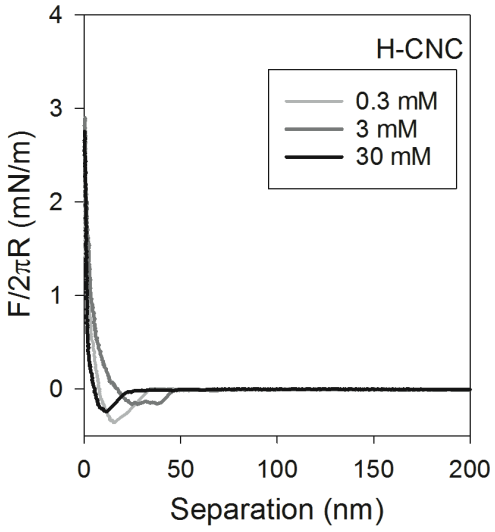

Figure 6.1: Representative retraction force curves for a silica probe against a H-CNC surface in the presence of $CaCl_2$ (0.03 mM, 3 mM and 30 mM) showing that adhesion in present in this system and manifests as a dip in the curve below zero force.

For statistical relevance, approximately 150 retraction force curves, taken in three different locations on the substrate, were collected for each probe-film-solution combination. Figure 6.1 shows a representative AFM force curve and the distribution of data amongst 150 force curves is similar to that presented in Chapter 5 Figure 5.1. The average adhesion (area under the curve), normalized by the probe radius, was determined from all force curves and compiled into a bar graph, as shown in Figure 6.2.

Figure 6.2 shows that with a silica probe, as the NaCl concentration increases, there is a decrease in adhesion for Na-CNC and H-CNC surfaces. For the silica surface, the opposite is seen whereby there is an increase in adhesion with increasing ionic strength (expected theoretically and from previous literature). This difference between the adhesion results for CNC surfaces and silica surfaces indicates that the interactions are not purely due to surface charge. Appendix Figure 6.7 shows the corresponding AFM force curves for CNC and silica surfaces in the presence of NaCl solution.

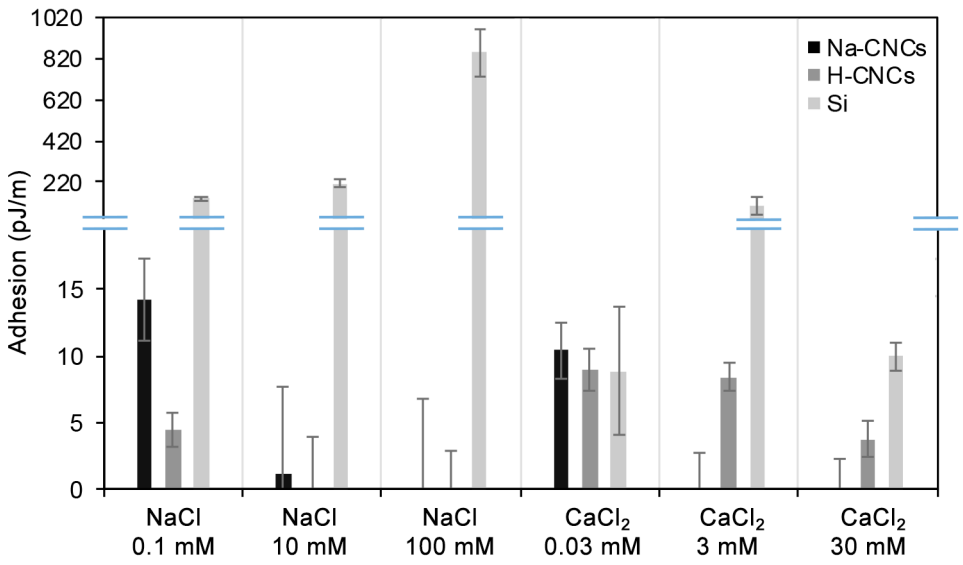

Figure 6.2: Average adhesion measured by AFM between a silica probe and CNC or silica surfaces in the presence of NaCl (0.1 mM, 10 mM and 100 mM) and $CaCl_2$ (0.03 mM, 3 mM and 30 mM – equivalent ionic strengths to NaCl). It is shown that for CNC surfaces in the presence of NaCl there is a decrease in adhesion with the increase of salt, but the reverse is observed for Si surfaces. In the presence of $CaCl_2$ it is shown that there may be ionic bridging for H-CNC and Si surfaces. Each bar is an average of at least 150 measurements; representative AFM force curves are shown in Appendix Figure 6.7 for NaCl and Figure 6.8 for $CaCl_2$. The error bars are one standard deviation of the average values.

A similar trend is observed in $CaCl_2$ where the adhesion between the silica probe and CNC surfaces decreases with an increase in $CaCl_2$ concentration. However, the adhesion for H-CNCs in the presence of $CaCl_2$ is higher than Na-CNC, which is the reverse of what was observed in NaCl. The H-CNC surface follows a trend similar to a Si surface where in both, adhesion peaks at 3 mM and then drops at 30 mM. This increase in adhesion may be due to ionic bridging induced by Ca^{2+} between the Si probe with H-CNC and Si surfaces. The AFM force curves on retraction for Na-CNC, H-CNC and Si surfaces are shown in the Appendix Figure 6.8, where the effects of bridging are shown in Appendix Figure 6.8b, a double dip in the curve indicates multiple adhesion events. The lack of adhesion in the case of the Na-CNC surface suggests that ionic bridging may be hindered, which as discussed in Chapter 5 may be due to ionic shielding by Na^{+}. Thus the difference in adhesion for Na-CNC and H-CNC in the presence of either NaCl or

$CaCl_2$ is not due to the surface charge but more the counterion associated with the surface.

The silica-silica adhesion results shown in Figure 6.2 are consistent with previous literature and are used as an internal control measurement; in NaCl adhesion increases with ionic strength because there is less repulsion but the trend is more convoluted in $CaCl_2$ because of the divalent nature of Ca^{2+} and bridging possibilities. Similarly this trend has been shown by Troncoso et al. [147] where increasing ionic strength increases the adhesion between silica probes and silica surfaces due to an increase in surface tension. On the contrary, it is shown by Dishon et al. that at high salt concentrations of 0.5-1 M NaCl (note: much higher than tested here), there is repulsion between a silica AFM probe and a silica surface attributed to the charge reversal at the surfaces, which leads to decreasing adhesion values with increasing salt concentration. In the same study, it was also shown that the decrease in the pH of the salt solution, from 5.5 to 4 by the addition of HCl, also decreases adhesion and shifts the onset of the charge reversal to a lower salt concentration [167].

For CNC surfaces it was observed that on retraction, the adhesion between the silica probe and Na-CNC or H-CNC decreased as the amount of NaCl increased, this is similar to the study by Dishon et al. mentioned above. Specifically, it is shown in Figure 6.2 that upon an increase in the salt concentration, the adhesion decreases more for H-CNC surfaces than Na-CNCs. The local acidity at the surface of CNCs where Na-CNC are neutralized and H-CNCs are not, may be a possible cause for the difference in adhesion.

Although the ionic strength of the NaCl and $CaCl_2$ solutions is the same for both salts, $CaCl_2$ solutions are shown to increase adhesion for silica-silica systems to a lesser degree than NaCl. For the silica probe with CNC and silica surfaces, it is observed that the addition of $CaCl_2$ initially results in very similar adhesion in Na-CNCs (11 ± 2 pJ/m), H-CNCs (9 ± 2 pJ/m) and Si (9 ± 4 pJ/m), but upon the increase of the $CaCl_2$ concentration the Na-CNC adhesion drops to 0 pJ/m whereas H-CNC adhesion is shown to stay fairly consistent, 8 ± 1 pJ/m for a $CaCl_2$ concentration of 3 mM and starts to drop thereafter reaching 4 ± 1 pJ/m by a $CaCl_2$ concentration of 30 mM. The higher adhesion between silica and H-CNCs may be due to ionic bridging induced by divalent Ca^{2+} which has been shown previously to occur on CNC surfaces [172,181]. In the case of Na-CNCs, the presence of the Na^+ ion hinders Ca^{2+} bridging as Na^+ is preferred at the surface over Ca^{2+}, as shown in studies pertaining to ion displacement [182]. Additionally, charge reversal as mentioned in Chapter 5, may be occurring at lower ionic strengths in the Na-CNC sample due to the combination of both Na^+ and Ca^{2+} present at the surface. For the silica surface, the adhesion increases to 100 ± 40 pJ/m at a concentration of 3 mM and then drops to 10 ± 1 pJ/m by 30 mM, which indicates that there is a threshold for ion bridging between 3 and 30 mM $CaCl_2$.

It is observed through these AFM force measurements that the effect of salt and its behaviour is more complicated than expected particularly when considering differences due to CNC counterion and surfaces that may have local surface acidity, i.e., due to sulfate half esters. The counterion affects how the surface interacts with other molecules and how the surface presents itself to the environment. Overall, the Na^+

counterion at the surface leads to a larger decrease in adhesion with increasing salt concentration than the H^+ counterion.

6.2.2 Surfactants

Interactions between a silica probe and different CNC surfaces (H-CNCs, Na-CNCs and Cat-CNCs) in the presence of surfactants, CTAB, SDS and TX100, were studied to understand the effect of surfactant type and concentration on adhesion. Based on the findings of Vakarelski et al. for silica-silica systems, we hypothesize that the presence of micelles and other surfactant morphologies (inferred from approach curves) will increase the adhesion for cellulose systems as well [146].

In Figure 6.3 it is shown that high adhesion values were measured for systems where surfactant structuring was observed in the Chapter 5 approach curves. For H-CNCs in the presence of cationic CTAB, the highest adhesion is measured at 0.5×CMC (110 ± 10 pJ/m), which is where higher order surfactant structures, likely micelles, were proposed from the AFM force data (Chapter 5, Figure 5.7b). For H-CNCs at 2×CMC CTAB there is no surfactant structuring and less adhesion (4 ± 1 pJ/m). The CNC systems with the strongest indication of surfactant structuring in Chapter 5 were H-CNCs at 0.5×CMC CTAB, Na-CNC at 2×CMC CTAB, and Cat-CNCs at 2×CMC SDS, which have the highest adhesion values in Figure 6.3.

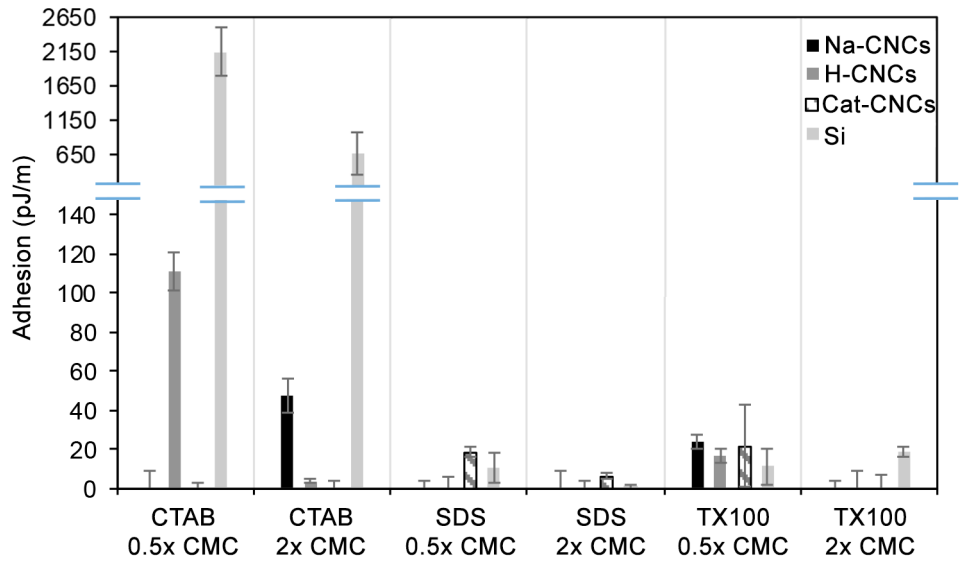

Figure 6.3: Average adhesion (pJ/m) measured by AFM between silica probes and H-CNC, Na-CNC, Cat CNCs and Si surfaces in the presence of surfactant solutions at half and twice the respective CMC of CTAB, SDS, and TX100. It is shown that maximum adhesion for CNCs can be achieved using H-CNCs in the presence of 0.5×CMC CTAB. Each bar is an average of at least 150 adhesion measurements, representative curves shown in Appendix Figure 6.9 for CTAB, Figure 6.10 for SDS and Figure 6.11 for TX100. The error bars are the standard deviation of the average values.

Looking at adhesion in CTAB in more detail, our results tend to agree with the literature. Lui et al. similarly showed through AFM force measurements that the presence of CTACl (CTAB with Cl^- as the counterion instead of Br^-) micelles at the surface of polymer films and Si increased adhesion [183]. For Na-CNCs in CTAB, it is shown that the adhesion values measured are higher where surfactant bi/multilayer formation was inferred, 2×CMC CTAB (50 ± 9 pJ/m), than where a thin surfactant layer is proposed, 0.5×CMC (~ 0 pJ/m). This again links structured surfactant at the surface of CNCs to the promotion of adhesion. We can use the silica-silica system as an internal control where in the approach curves (Figure 5.7c) micelles are encountered in the presence of CTAB at both concentrations and this leads to very high adhesion in the retraction curves, i.e., 2100 ± 400 and 600 ± 300 pJ/m (Figure 6.3). The higher adhesion generally observed for the silica surface is likely related to the smooth surface (root-mean-square roughness of 0.3 nm over 1 μm) and that structure of surfactants on the surface is more uniform and

covers surface charge more effectively. For Cat-CNCs the lack of CTAB interactions as presented in Chapter 5 translates to no adhesion. In all cases that show a lack of higher order surfactant structuring, little adhesion is measured.

In anionic SDS, H-CNCs and Na-CNCs were shown to have no surfactant adsorption and thus there is no adhesion (Figure 6.3). Oppositely charged Cat-CNCs were shown to have some interaction with SDS with apparent micelle formation at 2×CMC thus the surfactant is available to promote adhesion (6 ± 2 pJ/m). Higher adhesion (18 ± 3 pJ/m) is observed at 0.5×CMC, which, much like CTAB with H-CNCs, may be due to higher order surfactant structuring. In SDS 2×CMC, micelles lead to a high concentration of surfactant at the surface, which is repelled by both the anionic probe and the residual anionic charges at the Cat-CNC surface. Bremmell et al. saw a similar result where AFM adhesion measurements for a silica probe and an anionic polyelectrolyte surface in the presence of sodium dodecylbenzenesulfonate (SDbS, an anionic surfactant similar to SDS) was higher below the CMC [184]. The higher adhesion was attributed to partial surfactant micelles at the polyelectrolyte surface coming together and forming structured micelles, whereas the lower adhesion above the CMC was attributed to the repulsion of the probe and surface due to dense surfactant coating leading to the coming together of like charged surfaces as shown in Figure 6.4 [184].

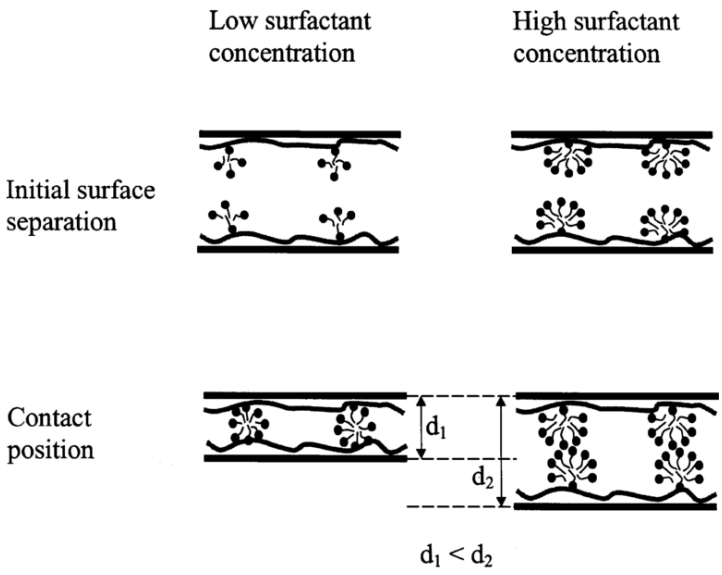

Figure 6.4: Proposed interaction of SDbD micelles upon the approach of a silica probe towards a cationic polyelectrolyte surface in the presence of SDbS solutions below and above the CMC. It is suggested that at low surfactant concentrations partial micelles come together to form complete micelles leading to an adhesive force whereas at high surfactant concentrations surfactant micelles already present at the surface result in a lack of adhesion. Figure reproduced from [184].

Uncharged TX100 is shown to interact similarly with all the surfaces tested. While no surfactant structuring was observed in the approach curves, the surfactant seems to coat all surfaces effectively screening electrostatic repulsion. In 0.5×CMC TX100, consistent (and non zero) adhesion is shown in Figure 6.3 irrespective of the surface type: 24 ± 4 pJ/m for Na-CNCs, 17 ± 3 pJ/m for H-CNCs, 21 ± 20 pJ/m for Cat-CNCs and 11 ± 9 pJ/m for Si. Above the CMC, it is shown that there is negligible adhesion for CNC surfaces, which may be due to the preference for formation of micelles in free solution rather than the surfactant adsorption at the surface.

As expected, the presence of micelles at surfaces leads to higher adhesion when compared to less structured surfactant morphologies such as bi/multilayers and monolayers on the surface. (We note that micelles may actually be hemi-micelles and other similar aggregate structures, and are dynamic and constantly exchanging molecules with the surroundings, but the AFM measurements indicate a feature on the same size

scale as a micelle, hence the use of the term). In systems where we infer a lack of surfactant adsorption at the surface, very minimal to no adhesion was measured, as was the cases of Cat-CNC with CTAB, anionic CNCs with SDS, and all CNCs with TX100. Thus to tailor adhesion, it is proposed that surface charge as well as counterion type are as important as the amount of surfactant present.

6.3 Interactions between Cellulose Probes and Cellulose and Silica Surfaces

6.3.1 Salts

The silica probe represents a smooth model surface with known/unchanging properties such as surface charge density. However, a cellulose probe is more representative of the interactions we are truly interested in. That is, in CNC or CNF nanocomposites what are the governing forces between cellulose particles? This work employs a regenerated cellulose sphere with a diameter of ~30 μm as the probe. This cellulose probe is uncharged and is primarily amorphous cellulose in contrast to anionic and highly crystalline cellulose I CNCs. As such, the probe is expected to be much less influenced by ionic strength.

Figure 6.5 shows that all adhesion values are lower with the cellulose probe vs. the silica probe (Figure 6.3) with larger variations in data (represented by the larger error bars). Adhesion is shown to be generally higher in the presence of $CaCl_2$ compared to NaCl, which may be due to ionic bridging between the AFM cellulose probe and the surface. In Chapter 5, Na-CNC results show that the Na^+ counterion hinders the adsorption of Ca^{2+} to Na-CNC surfaces. Thus for Na-CNCs in 0.03 mM $CaCl_2$ the adhesion measurements are of a similar magnitude to Na-CNCs in 0.1 mM NaCl - essentially no adhesion. For H-CNCs and Si it is shown that adhesion values are

consistent as $CaCl_2$ concentration increases, the lack of Na^+ at the surface allows Ca^{2+} to interact with the surfaces to facilitate ion bridging even at low salt concentrations.

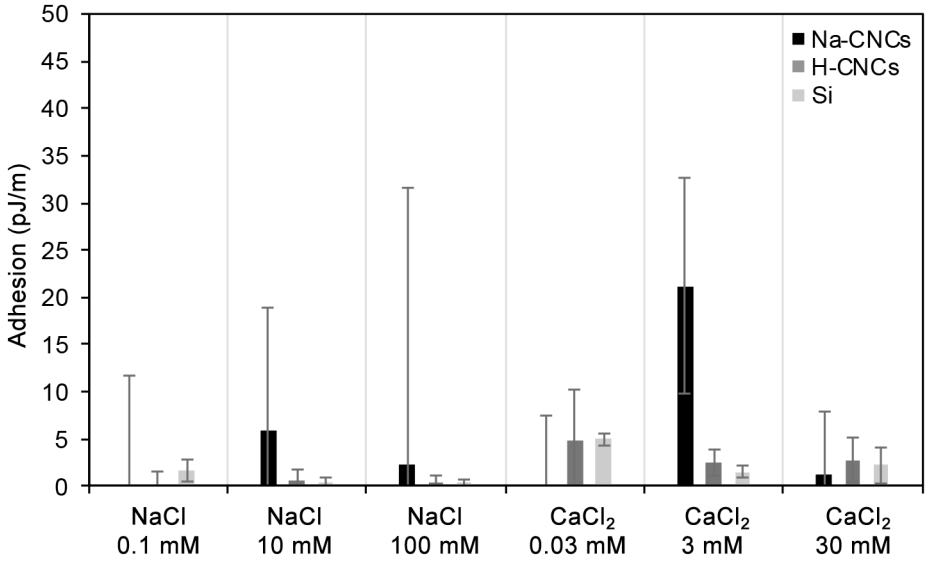

Figure 6.5: Average adhesion (pJ/m) measured by AFM between cellulose probes and H-CNCs surfaces, Na-CNC surfaces, and Si wafer surfaces in the presence of NaCl solutions at a concentration of 0.1 mM, 10 mM and 100 mM and the ionic strength equivalent of $CaCl_2$ of 0.03 mM, 3 mM and 30 mM. Each bar is an average of at least 150 adhesion measurements, representative curves shown in Appendix Figure 6.12 for NaCl and Figure 6.13 for $CaCl_2$. The error bars are the standard deviation of the average values.

Upon the increase of salt concentration to 10 mM for NaCl and 3 mM $CaCl_2$, there is a large increase in adhesion for Na-CNC, which may be due to the interactions of $CaCl_2$ with the probe rather than the Na-CNC surface. Charge reversal due to high ion concentration at the surface may explain the dip in adhesion seen for H-CNCs and Si and the increase in adhesion for Na-CNCs at 3 mM $CaCl_2$. As such at 30 mM $CaCl_2$ the salt concentration may be high enough to screen all surface charges leading to adhesion values for Na-CNC similar to H-CNCs. Since Ca^{2+} can facilitate ion bridging and is more easily hydrated than Na^+, according to reactivity series as discussed in Chapter 5, the adhesion in the presence of $CaCl_2$ is stronger. H-CNC surfaces are again observed to behave similar to silica surfaces where a low ion concentration is needed to screen surface charges. Thus it can be concluded that the effects of salt depend on the CNC

counterion and that low concentrations of salt promote adhesion and high concentrations result in charge reversal on the CNC surfaces.

A linear least squares model was used to compare the effect of probe type on the average adhesion for the different CNC surfaces in solutions with varying ionic strength. A three factor system, coded as – and + respectively for each parameter, comparing adhesion in terms of: salt concentration (SC) at –(0.1 mM) and +(100 mM); cellulose type (CT), either –(H-CNCs) or +(Na-CNCs); and probe type (PT), either –(cellulose) or +(silica), was used. The average adhesion values for each parameter were used as the input. The model results for measurements in NaCl are shown in Table 6.1. The model output is used to show what parameters have the most effect on adhesion. A positive coefficient value indicates an increase in the average adhesion when moving from a parameter coded as – and going to a +, i.e., going from a CT: –(H-CNC) to CT:+(Na-CNC) increases adhesion on average by 1.47 units.

The model coefficients in Table 6.1 show that the increase in ionic strength decreases adhesion (shown by the negative sign of the coefficient) whereas the use of a Na-CNC surface or a silica probe increases adhesion. Changing the salt concentration in conjunction with probe type (SC:PT) has the most effect on adhesion (largest coefficient) where decreasing the salt concentration and changing the probe to cellulose decreases adhesion by an average of 2.68 units for either CNC film type. From this analysis it is indicated that to maximize adhesion it is beneficial to have low salt concentration, Na-CNCs and a silica probe.

Table 6.1: Least squares model coefficient results for force measurements done in NaCl solution concentration (SC) of 0.1 mM and 100 mM on cellulose surfaces (CT) H-CNCs and Na-CNCs with cellulose and silica probes (PT). The code was run in R using average adhesion values as inputs for a three factor system: salt concentration (SC): - [0.1 mM], + [100 mM], cellulose type (CT): - [H-CNCs], + [Na-CNCs], and probe type (PT): -[Cellulose], + [Silica].

Parameters	(Intercept)	SC	CT	PT
Model output coefficients	2.6875	-1.9975	1.4725	1.9975
Interacting Parameters	SC:CT	SC:PT	CT:PT	SC:CT:PT
Model output coefficients	-0.9875	-2.6875	0.9875	-1.4725

Similarly Table 6.2 shows the model results in $CaCl_2$ solution and it is observed that changing the SC has the most effect. It is shown that for $CaCl_2$ that a H-CNC surface is more beneficial to adhesion than having a Na-CNC surface as going from a CT: –(H-CNC) to CT: +(Na-CNC) increases adhesion on average by -1.07 units which corresponds to a decrease in adhesion.

Table 6.2: Least squares model coefficient results for force measurements done in $CaCl_2$ salt solution concentration (SC) of 0.1 mM and 100 mM on cellulose surfaces (CT) H-CNCs and Na-CNCs with cellulose and silica probes (PT). The code was run in R using average adhesion values as inputs for a two factorial system: salt concentration (SC): - [0.1 mM], + [100 mM], cellulose type (CT): - [H-CNCs], + [Na-CNCs], and probe type (PT): - [Cellulose], + [Silica].

Parameters	(Intercept)	SC	CT	PT
Model output coefficients	3.9800	-2.0650	-1.0775	1.7875
Interacting Parameters	SC:CT	SC:PT	CT:PT	SC:CT:PT
Model output coefficients	-0.2325	-1.8375	0.5100	-1.0650

A direct comparison of Tables 6.1 and 6.2 shows that the highest adhesion in the systems studied is by the use of a silica probe and a Na-CNC surface in the presence of low NaCl concentration. These models can be used to give a good approximation of salt-CNC interactions but they do not account for physical anomalies such as differences in

surface roughness, as shown in the cellulose probe data in Figure 6.5 for Na-CNC at 3 mM $CaCl_2$, which should be considered when using such models. This anomaly is attributed to the cellulose probe and not the Na-CNC surface.

6.3.2 Interactions with CTAB

Since cationic CTAB with anionic CNCs was found to have the most influence on adhesion, we chose to measure AFM retraction curves in these systems only to compare to the silica probe results. As with the salt experiments, it was expected that the cellulose probe–CNC film interactions in the presence of surfactants would be similar to what was presented using the silica probe. To the contrary, CTAB did not improve adhesion between a cellulose probe and CNC surfaces as shown in Figure 6.5 (which compares cellulose probe on the left to the silica probes on the right). In Chapter 5, Figure 5.16 it was also implied that structuring of surfactants near the surface was less apparent/regular and required less force to rupture with the cellulose probe compared to the silica probe which is consistent with the discussion above that concludes that more surfactant structuring near a surface leads to higher adhesion. There is no significant difference in the adhesion measured for Na-CNC compared to H-CNC with the cellulose probe, however, as discussed previously, the silica substrate displayed the highest adhesion. Again this supports that surface roughness, presented in Appendix Figure 6.14 as bumpy force curves, is one of the primary factors that controls both pre-contact and adhesive forces (and the precision to which they can be measured) in colloid probe AFM experiments.

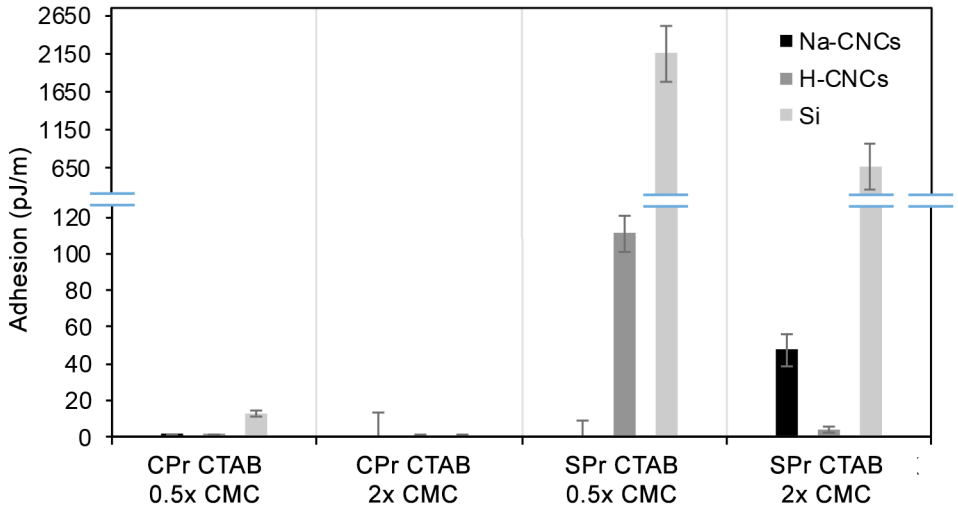

Figure 6.6: A comparison of average adhesion (pJ/m) measuremed by AFM for cellulose probes (denoted by CPr) and silica probes (denoted by SPr) between surfaces of and H-CNCs, Na-CNC, and Si surfaces in the presence of CTAB solutions at half and twice the CMC. Each bar is an average of at least 150 adhesion measurements, representative curves shown in Appendix Figure 6.14 for cellulose probe and Figure 6.9 for Si probe. The error bars are the standard deviation of the average values.

The addition of surfactants has been shown in literature to aid in the better incorporation of CNCs into polymer matrixes [10–12]. Ljungberg et al. [10,11] have shown that the use of BNA (an anionic surfactant) to encapsulate CNCs increased the dispersion of CNCs in polypropylene blends giving better mechanical properties than the incorporation of neat CNCs and polymer grafted CNCs. Additionally, a higher elongation at break was shown for a polypropylene blend with surfactant coated CNCs than neat polypropylene. Similarly the study was done by Bondeson et al. [12] linking the addition of BNA surfactant to increased dispersion of CNCs in polylactic acid. Although, the studies by Ljungberg et al. and Bondeson et al. use hydrophobic solvents (toluene and chloroform) to encourage the encapsulation of CNCs with surfactant, the increased dispersion of CNCs and increased mechanical strength reinforces the finding of higher adhesion in the presence of surfactant at CNCs surfaces as shown in Figure 6.3 and Figure 6.5. The results in chapters 5 and 6 suggest that cationic surfactants may offer better dispersion since they interact more with CNC surfaces and result in more adhesion

than anionic surfactants. The study by Nagalakshmaiah et al. [13] using CTAB to compatiblize CNCs with a polypropylene matrix shows that the addition of CTAB along with CNCs rather than neat CNCs results in an additional increase in the elongation at break of the polymer blend from 15.4 % with CNCs to 109 % for CNCs added with CTAB. A comparison of the work by Ljungberg et al. and Nagalakshmaiah et al. suggests that the elongation at break is higher when CTAB is used rather than BNA, but a conclusion cannot be made, as there are differences in CNC preparation and polymer blending methods.

6.4 Conclusions

It is shown that the interactions observed in Chapter 5 have a corresponding influence on the adhesion discussed in this chapter. AFM force measurements indicate that the CNC counterion type has a significant effect on how the CNC surfaces interact with other molecules. Although adhesion in the presence of salt decreased for both Na-CNCs and H-CNCs, the Na^+ counterion on Na-CNCs results in a larger decrease in adhesion with increasing salt concentration. Maximum adhesion is observed by the use of a silica probe and a Na-CNC surface in the presence of low NaCl concentration. For surfactants, the presence of surfactant structuring inferred in Chapter 5 is shown to correlate well with high adhesion values. Systems that exhibited no surfactant structuring at the CNC surface have negligible adhesion whereas systems that exhibited micelle morphology (H-CNC 0.5×CMC CTAB, Cat-CNCs 2×CMC SDS) have relatively high adhesion. Systems that exhibited bi/multilayer structures (Na-CNC at both CTAB concentrations) have intermediate adhesion, where more layers of surfactant correspond to less adhesion. CTAB (and likely other cationic surfactants) with H-CNCs at low

concentrations are the most effective at compatibilization or increasing adhesion. Measurements done using a cellulose probe showed a similar trend for both salt and surfactant interactions but due to the roughness of the probe and variability in data it is difficult to draw significant conclusions.

6.5 Appendix

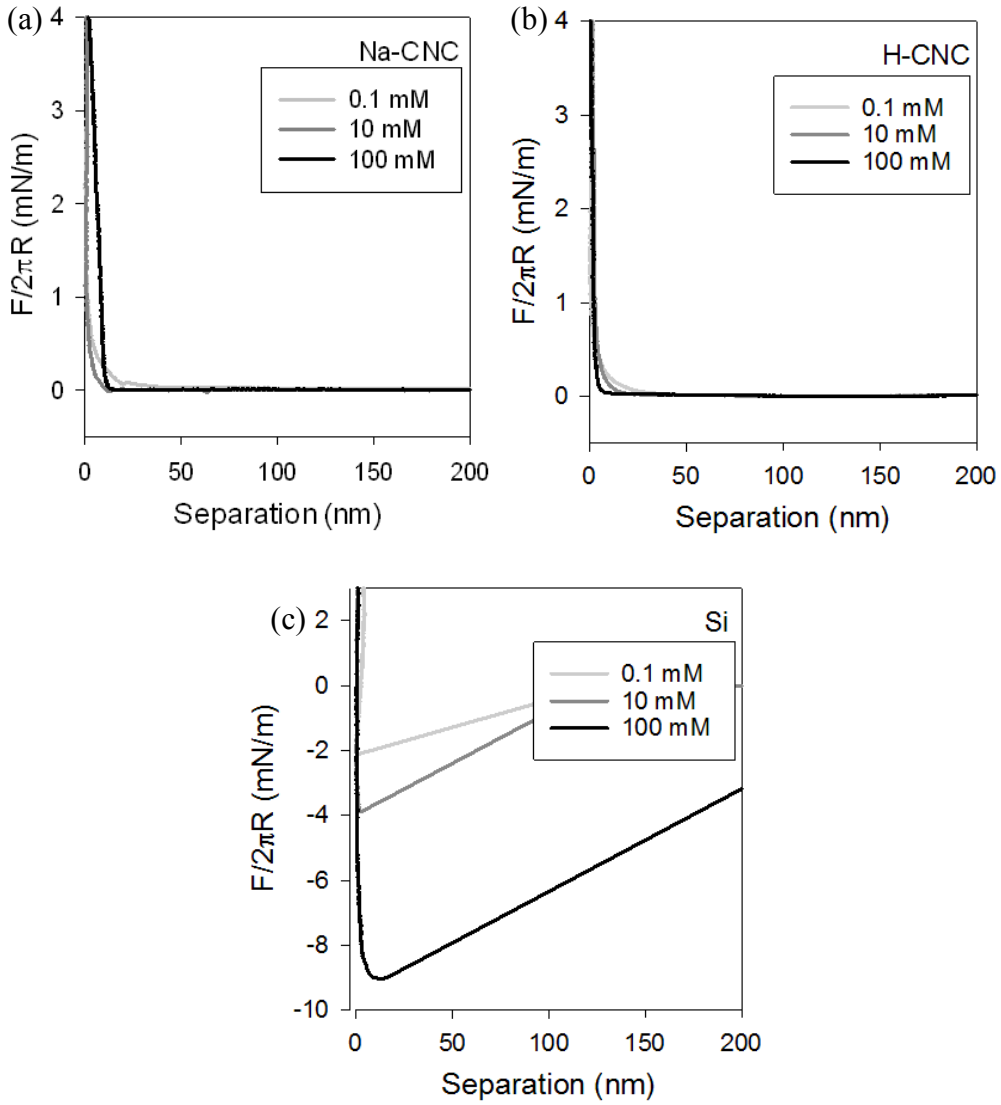

Figure 6.7: Retraction force curves for a silica probe retracting from (a) Na-CNC, (b) H-CNC, and (c) Si surfaces in the presence of 0.1 mM, 10 mM and 100 mM NaCl solutions.

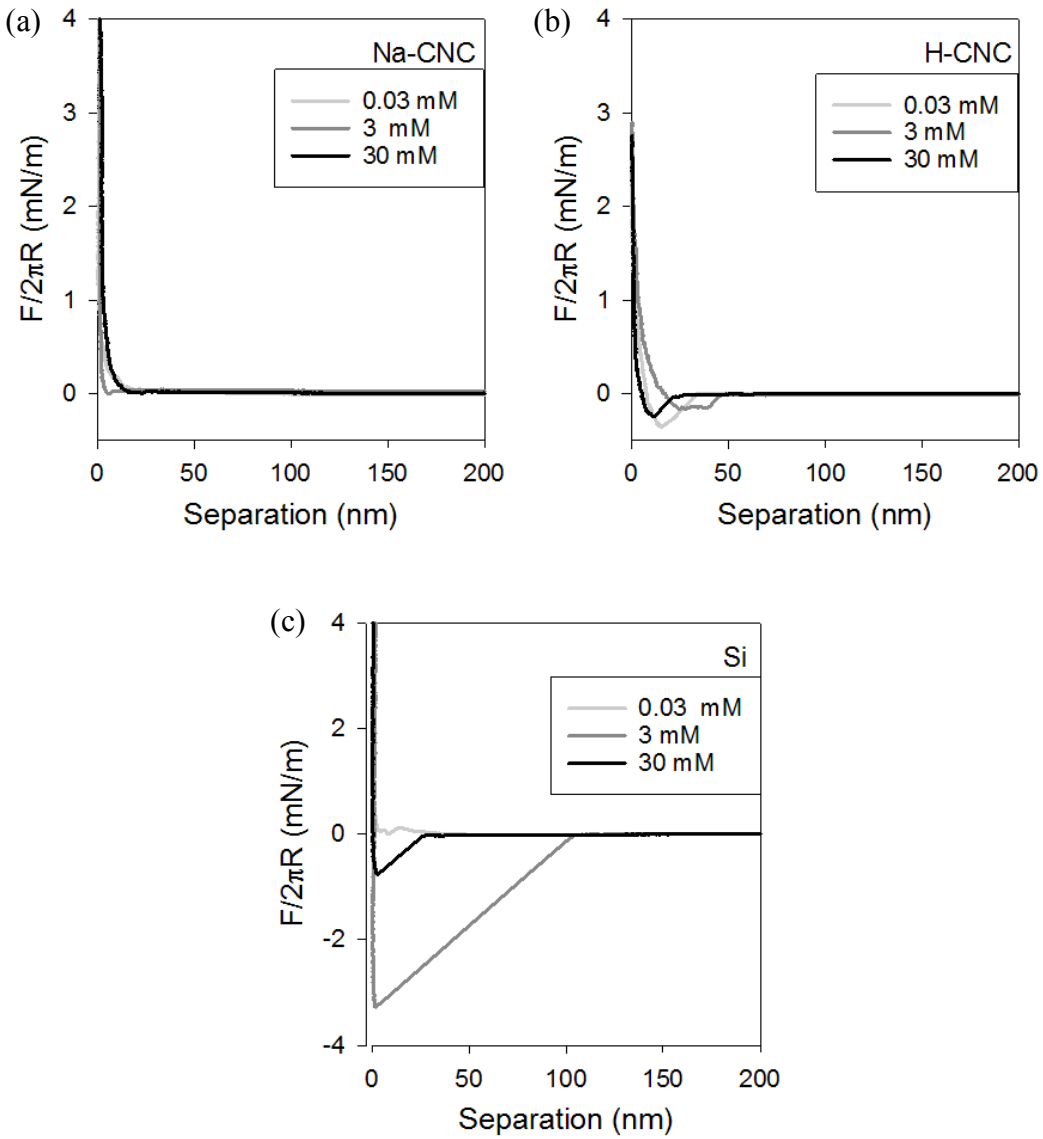

Figure 6.8: Retraction force curves for a silica probe retracting from (a) Na-CNC, (b) H-CNC, and (c) Si surfaces in the presence of 0.03 mM, 3 mM and 30 mM $CaCl_2$ solutions.

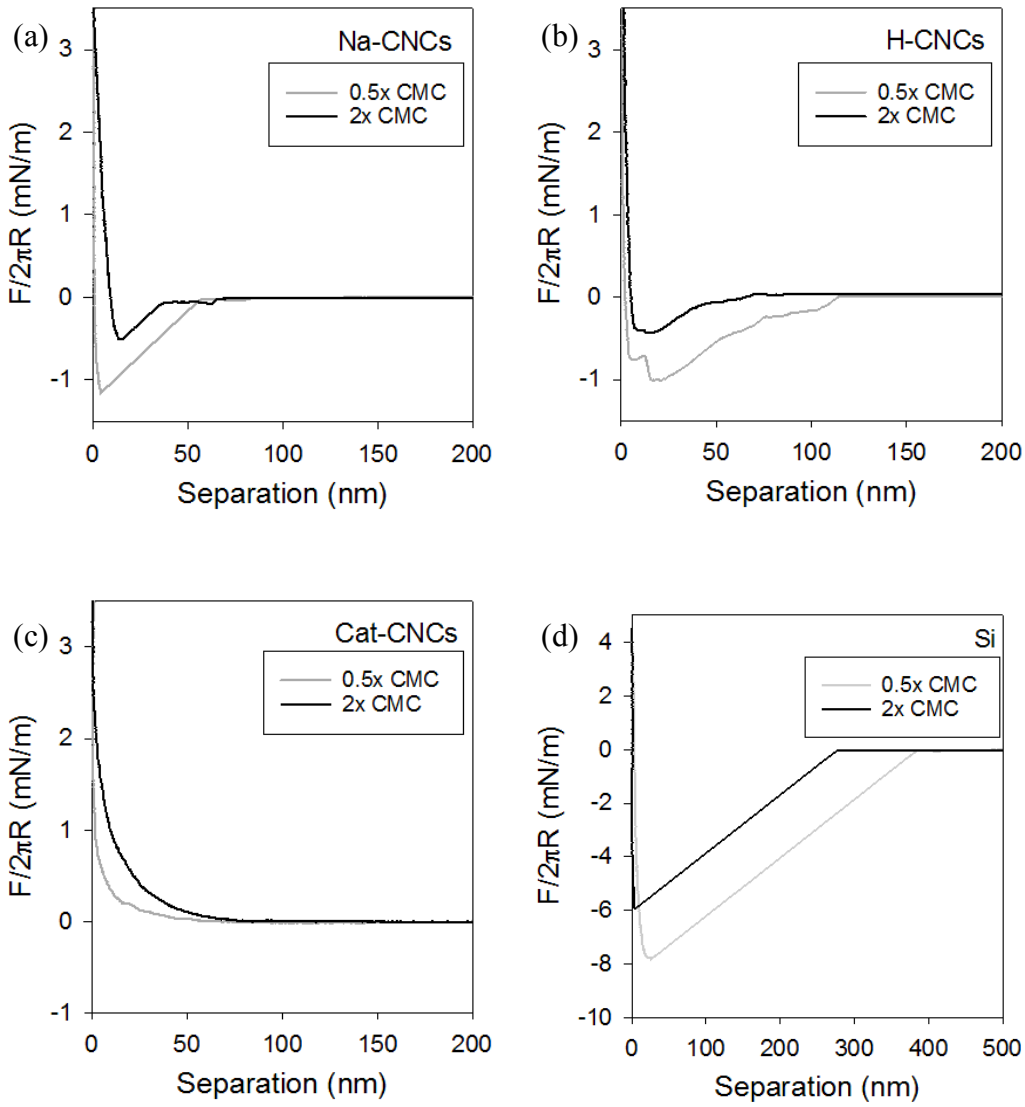

Figure 6.9: Retraction force curves for a silica probe retracting from (a) Na-CNC, (b) H-CNC, (c) Cat-CNC and (d) Si surfaces in the presence of 0.5x and 2x CMC CTAB solutions.

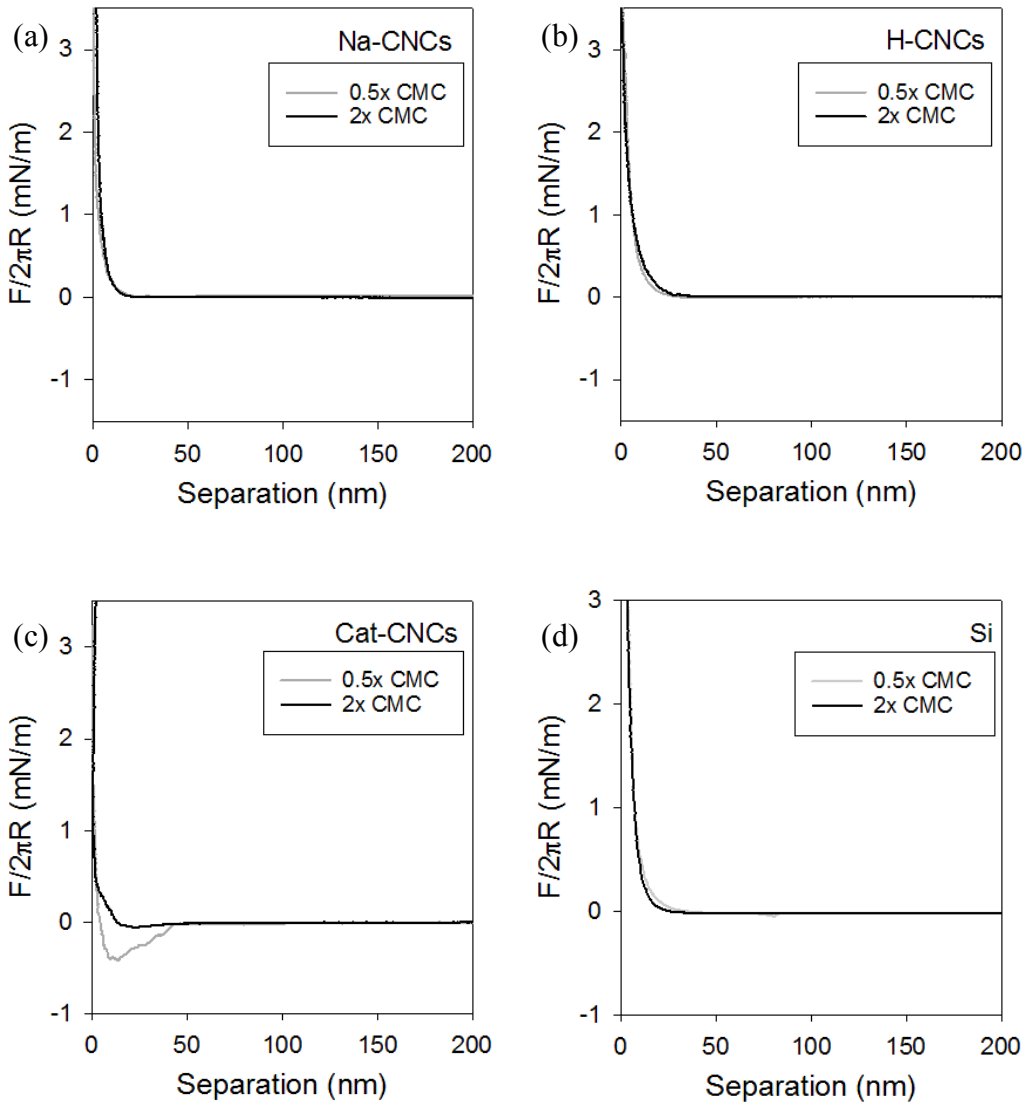

Figure 6.10: Retraction force curves for a silica probe retracting from (a) Na-CNC, (b) H-CNC, (c) Cat-CNC and (d) Si surfaces in the presence of 0.5x and 2x CMC SDS solutions.

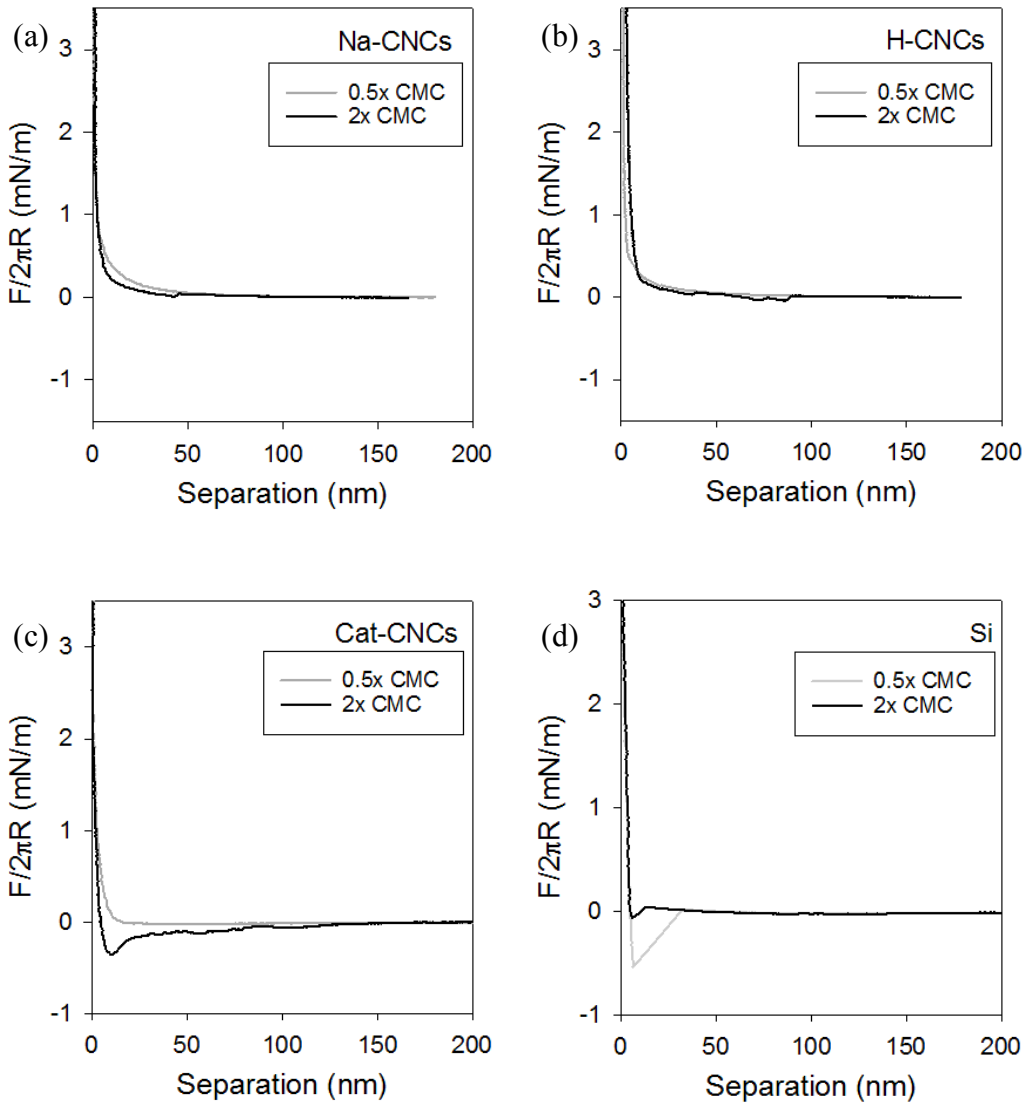

Figure 6.11: Retraction force curves for a silica probe retracting from (a) Na-CNC, (b) H-CNC, (c) Cat-CNC and (c) Si surfaces in the presence of 0.5× and 2× CMC TX100 solutions.

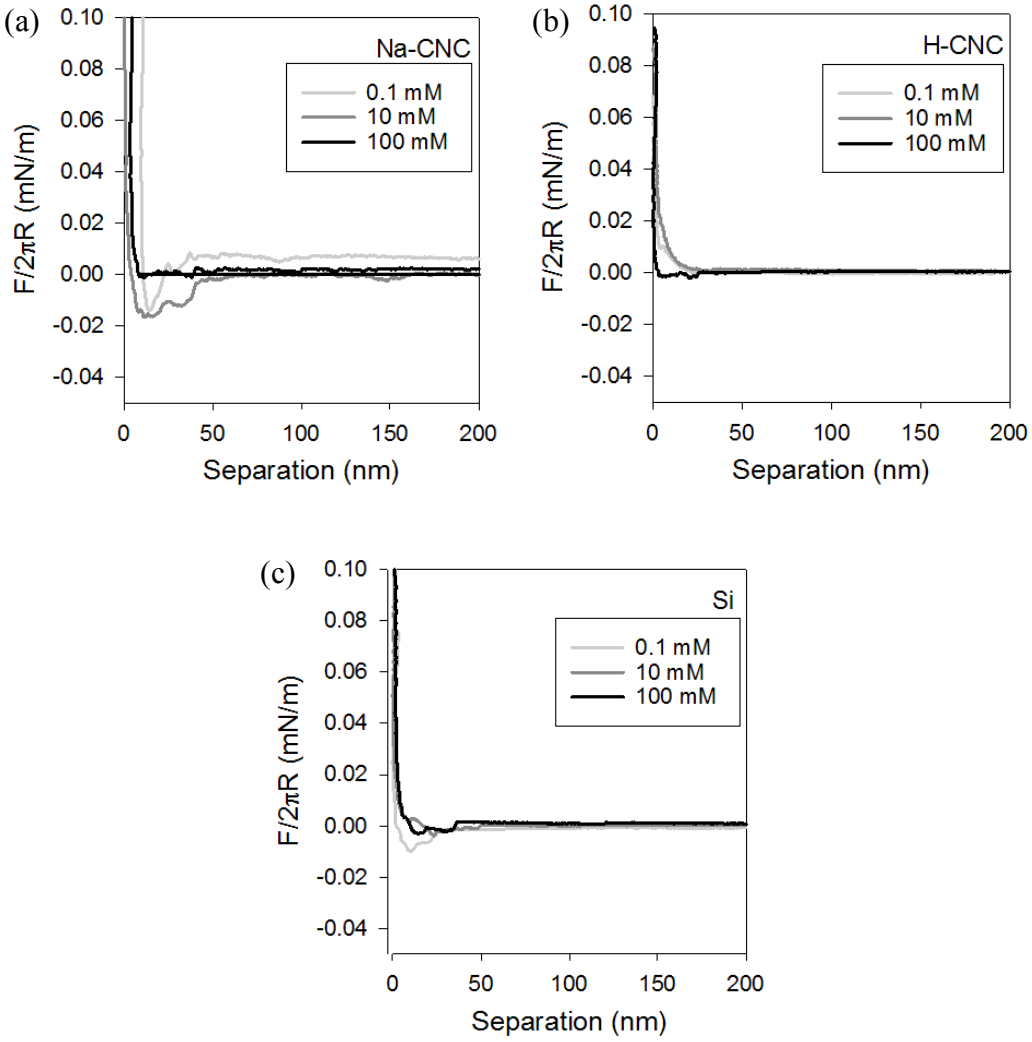

Figure 6.12: Retraction force curves for a cellulose probe retracting from (a) Na-CNC, (b) H-CNC, and (c) Si surfaces in the presence of 0.1 mM, 10 mM and 100 mM NaCl solutions.

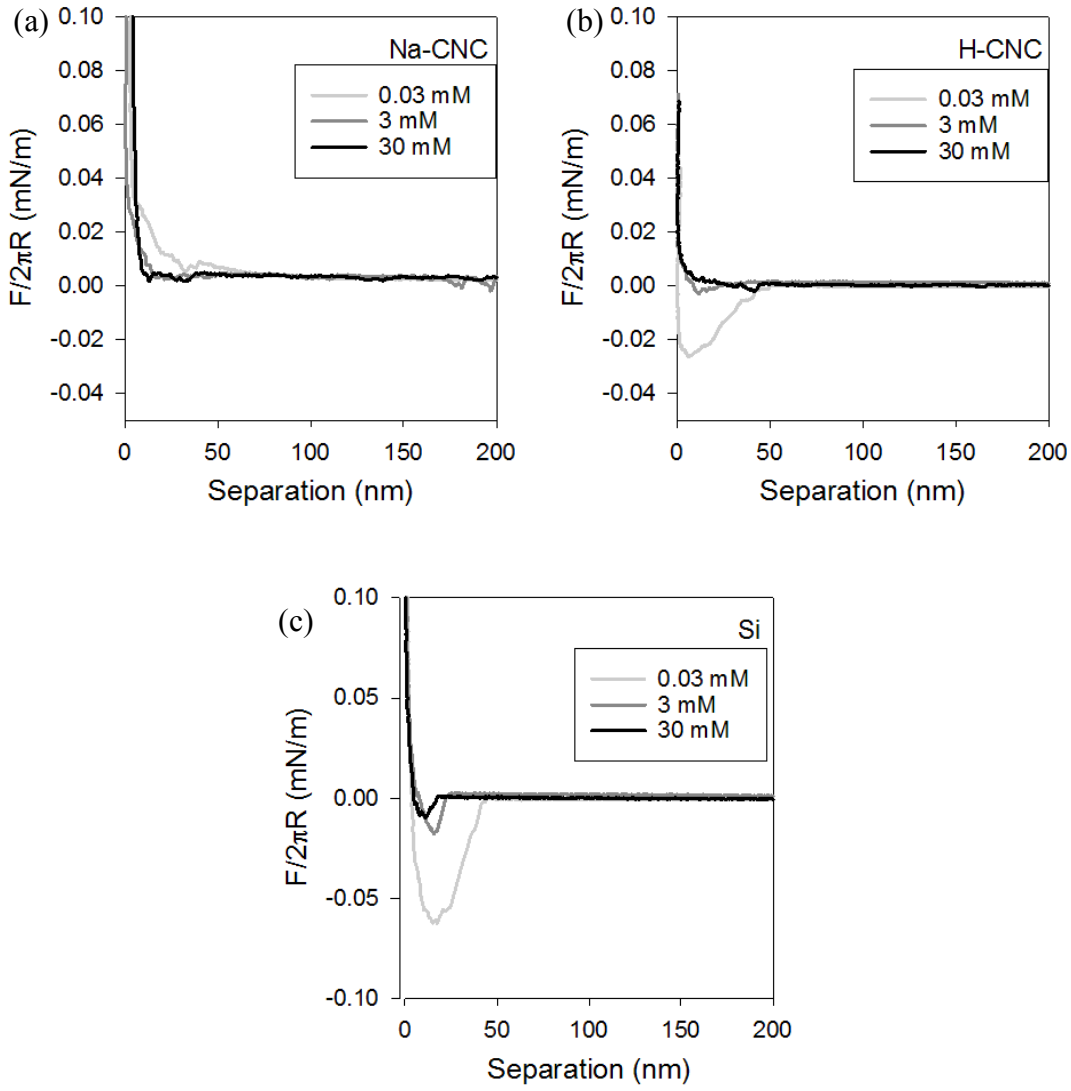

Figure 6.13: Retraction force curves for a cellulose probe retracting from (a) Na-CNC, (b) H-CNC, and (c) Si surfaces in the presence of 0.03 mM, 3 mM and 30 mM $CaCl_2$ solutions.

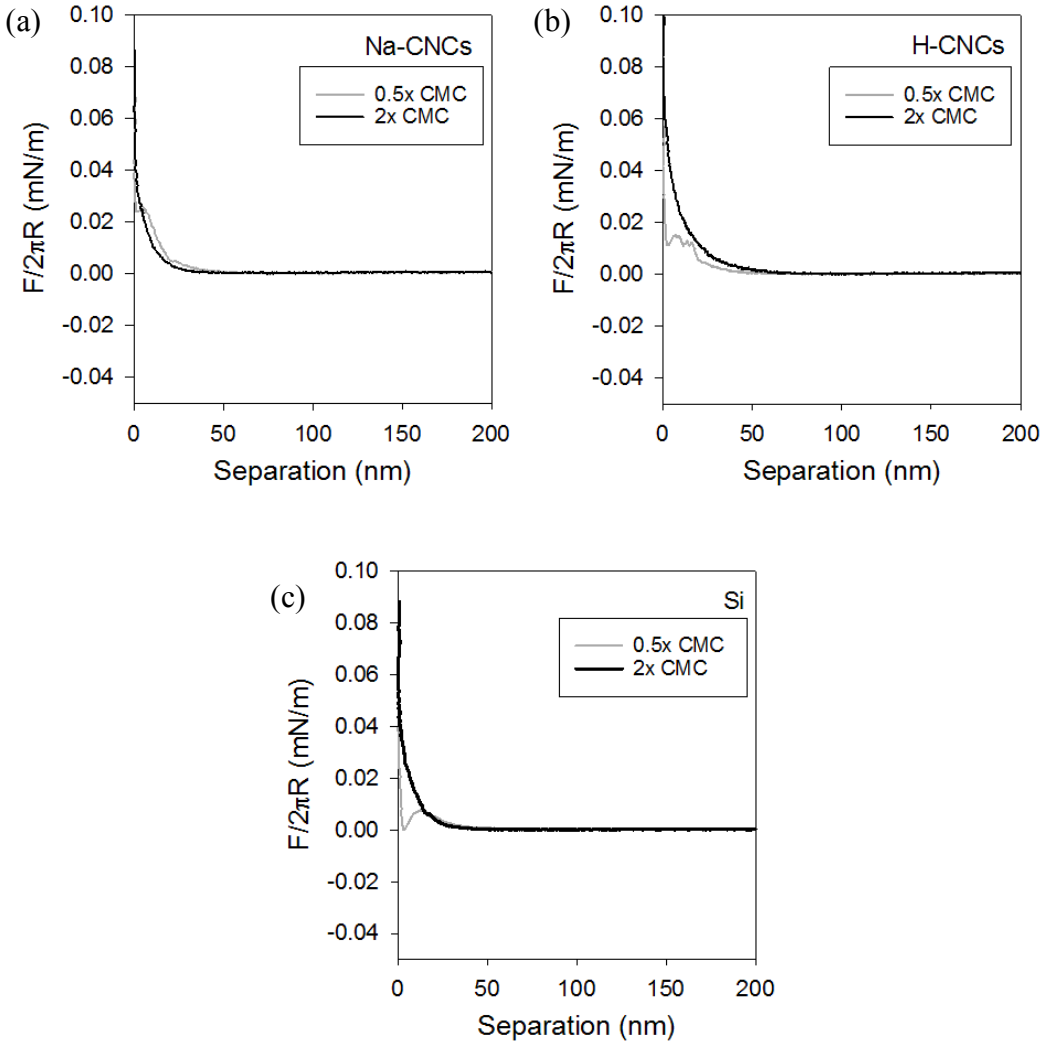

Figure 6.14: Retraction force curves for a cellulose probe retracting from (a) Na-CNC, (b) H-CNC, (c) Cat-CNC and Si surfaces in the presence of 0.5× and 2× CMC CTAB solutions.

Code for DOE:

The following code was run in R (version 3.3) using RStudio (version 0.99.902) to develop a least squares model where c is the resultant adhesion measurements for six factors tested.

```
x <- c(-1, +1)
design <- expand.grid(C=x, T=x, S=x)
SC <- design$C
CT <- design$T
PT <- design$S
y <- c(4.84, 2.72, 0, 1.21, 8.94, 3.73, 10.4, 0)
mod.full <- lm( y ~ SC*CT*PT )
mod.full
```

7. Conclusions and Recommendations

7.1 Conclusions

The Young's modulus of nanocellulose (both CNCs and CNFs) was successfully measured using AM-FM AFM mechanical mapping. Next, the pre-contact surface force interactions for CNC films were measured using colloid probe AFM, showing that the CNC counterion type has a significant effect on the interactions in both salt and surfactant solutions. Particle sizing and electrophorectic mobility corroborated the surfactant interactions observed by colloid probe AFM force measurements on approach. On retraction of the probe from the CNC surface, low salt concentrations and surfactant structuring resulted in high adhesion.

This is the first report of using AM-FM AFM to measure the Young's modulus of CNCs and CNFs giving values of 90 ± 20 GPa and 120 ± 30 GPa, respectively. These values are in good agreement with the literature. This shows that the AM-FM AFM technique is relevant for the measurement of crystalline nanoparticles and that CNCs and CNFs have mechanical properties that should lend well to mechanical reinforcing applications.

The counterion type on CNCs (Na^+ versus H^+) has a significant effect on how CNCs interact with an opposing surface (silica or cellulose probe) in the presence of salts and surfactants. Colloid probe AFM, particle size and electrophorectic mobility showed that there is more interaction of surfactants with oppositely charged CNC surfaces, but also that there is more interaction with Na-CNCs than with H-CNCs. The sodium counterion appears to promote hydrophobic interactions in addition to electrostatic interactions leading to loose/disordered surfactant aggregate structures at the CNC

surfaces. Conversely, for H-CNCs and Cat-CNCs with CTAB and SDS, respectively, electrostatically adsorbed micelles at the CNC surface are inferred and lead to high colloid probe-CNC adhesion. This indicates that since the counterion type has such a drastic effect on surface forces that it is imperative that it be taken into consideration during experiment and material design and at the very minimum, be reported in the literature as to whether Na^+ or H^+ form CNCs were used.

The knowledge gained via these fundamental measurements can be used to guide future work with cellulose nanomaterials, specifically related to the compatibilization of CNCs and CNFs using salts and surfactants. Both CNCs and CNFs have a high potential as mechanical reinforcing agents due to their stiffness, as demonstrated here by AM-FM AFM. The understanding of the pre-contact interactions and adhesion based on the counterion type can be applied to future formulation design for the production of nanocomposites, foams, emulsion, latexes, gels and biomedical devices containing CNCs.

7.2 Recommendations

This work opens the door to many new studies that can now be envisioned using the findings from Chapters 4 to 6 as a basis:

1. AM-FM AFM can be further used to measure the mechanical properties of composite materials made using nanocellulose. Mapping the modulus of composite materials can be used to show the distribution of nanocellulose fibres themselves and how they affect the mechanical properties of the composites. As this is a new AFM mode, very little work has been shown in the literature on reinforced polymer composites.

2. Colloid probe AFM can be used to further investigate the interactions of CNCs both Na-CNCs and H-CNCs with different salts, in particular KCl and $MgCl_2$. The use of KCl and $MgCl_2$ will give a better understanding of how the reactivity series and Hofmeister series can be used to predict salt CNC interaction. As K^+ has a smaller atomic radius and is more reactive than Na^+, it will show the effects of salt on CNCs further and may help explain the differences between Na-CNCs and H-CNCs. As Mg^{2+} is less reactive than Ca^{2+}, $MgCl_2$ may also support findings in Chapter 5 that show decreased interactions of CNCs with less reactive salts. Colloid probe AFM can also be used to measure the different interaction of CNCs based on the counterion type with counterions other than Na^+ and H^+ such as Ca^{2+}.
3. The interactions of CNCs in salt and surfactant solutions should also be investigated with CNCs made using acids other than sulfuric acid, such as phosphoric acid and hydrochloric acid, as this gives different CNC surface chemistries and pKa's. These different pKa's would allow a comparison of effect based mainly on particle acidity.
4. Comparing mechanical properties of CNC nanocomposites made using H-CNC and Na-CNC with surfactants (and assessing the CNC dispersion) could be used to test the findings in Chapter 6. Currently the literature rarely differentiates between H-CNC and Na-CNC when reporting the formulation of composites. A thorough investigation based on the effects of salt/surfactant addition on adhesion will likely show that there is a need to report the CNC counterion and that counterions offer an additional way to tune CNC nanocomposite properties.

8. References

[1] Dufresne, A. *Nanocellulose: From Nature to High Performance Tailored Materials.*; Walter De Gruyter Inc, 2012.

[2] Dufresne, A.; Belgacem, M. N. Cellulose-Reinforced Composites: From Micro-to Nanoscale. *Polímeros Ciência e Tecnol.* **2010**, *20* (1), 1–10.

[3] Habibi, Y.; Lucia, L. a; Rojas, O. J. Cellulose Nanocrystals: Chemistry, Self-Assembly, and Applications. *Chem. Rev.* **2010**, *110* (6), 3479–3500.

[4] Rojas, O. J.; Montero, G. A.; Habibi, Y. Electrospun Nanocomposites from Polystyrene Loaded with Cellulose Nanowhiskers. *J. Appl. Polym. Sci.* **2009**, *113* (2), 927–935.

[5] Missoum, K.; Belgacem, M.; Bras, J. Nanofibrillated Cellulose Surface Modification: A Review. *Materials (Basel).* **2013**, *6* (5), 1745–1766.

[6] Kim, J.; Montero, G.; Habibi, Y.; Hinestroza, J. P.; Genzer, J.; Argyropoulos, D. S.; Rojas, O. J. Dispersion of Cellulose Crystallites by Nonionic Surfactants in a Hydrophobic Polymer Matrix. *Polym. Eng. Sci.* **2009**, *49* (10), 2054–2061.

[7] Jalili, N.; Laxminarayana, K. A Review of Atomic Force Microscopy Imaging Systems: Application to Molecular Metrology and Biological Sciences. *Mechatronics* **2004**, *14*, 907–945.

[8] Ralston, J.; Larson, I.; Rutland, M. W.; Feiler, A. a.; Kleijn, M. Atomic Force Microscopy and Direct Surface Force Measurements (IUPAC Technical Report). *Pure Appl. Chem.* **2005**, *77* (12), 2149–2170.

[9] Garcia, R.; Proksch, R. Nanomechanical Mapping of Soft Matter by Bimodal Force Microscopy. *Eur. Polym. J.* **2013**, *49* (8), 1897–1906.

[10] Klemm, D.; Heublein, B.; Fink, H.-P. P.; Bohn, A. Cellulose: Fascinating Biopolymer and Sustainable Raw Material. *Angew. Chemie - Int. Ed.* **2005**, *44* (22), 3358–3393.

[11] Asghar, A.; Abdul Samad, Y.; Singh Lalia, B.; Hashaikeh, R. PEG Based Quasi-Solid Polymer Electrolyte: Mechanically Supported by Networked Cellulose. *J. Memb. Sci.* **2012**, *421–422*, 85–90.

[12] Zugenmaier, P. *Crystalline Cellulose and Cellulose Derivatives*; 2008.

[13] Moon, R. J.; Martini, A.; Nairn, J.; Simonsen, J.; Youngblood, J. Cellulose Nanomaterials Review: Structure, Properties and Nanocomposites. *Chem. Soc. Rev.* **2011**, *40* (7), 3941–3994.

[14] Hon, D. N. S. Cellulose: A Random Walk along Its Historical Path. *Cellulose* **1994**, *1*, 1–25.

[15] Peng, B. L.; Dhar, N.; Liu, H. L.; Tam, K. C. Chemistry and Applications of Nanocrystalline Cellulose and Its Derivatives: A Nanotechnology Perspective. *Can. J. Chem. Eng.* **2011**, *89* (5), 1191–1206.

[16] Klemm, D.; Kramer, F.; Moritz, S.; Lindström, T.; Ankerfors, M.; Gray, D.; Dorris, A. Nanocelluloses: A New Family of Nature-Based Materials. *Angew. Chemie Int. Ed.* **2011**, *50* (24), 5438–5466.

[17] Roman, M. Toxicity of Cellulose Nanocrystals: A Review. *Ind. Biotechnol.* **2015**, *11* (1), 25–33.

[18] Carpenter, A. W.; De Lannoy, C. F.; Wiesner, M. R. Cellulose Nanomaterials in Water Treatment Technologies. *Environ. Sci. Technol.* **2015**, *49* (9), 5277–5287.

[19] Abitbol, T.; Rivkin, A.; Cao, Y.; Nevo, Y.; Abraham, E.; Ben-Shalom, T.; Lapidot, S.; Shoseyov, O. Nanocellulose, a Tiny Fiber with Huge Applications. *Curr. Opin. Biotechnol.* **2016**, *39* (I), 76–88.

[20] Yang, X.; Cranston, E. D. Chemically Cross-Linked Cellulose Nanocrystal Aerogels with Shape Recovery and Superabsorbent Properties. *Chem. Mater.* **2014**.

[21] Yang, X.; Bakaic, E.; Hoare, T.; Cranston, E. D. Injectable Polysaccharide Hydrogels Reinforced with Cellulose Nanocrystals: Morphology, Rheology, Degradation, and Cytotoxicity. *Biomacromolecules* **2013**, *14* (12), 4447–4455.

[22] Chau, M.; De France, K. J.; Kopera, B.; Machado, V. R.; Rosenfeldt, S.; Reyes, L.; Chan, K. J. W.; Förster, S.; Cranston, E. D.; Hoare, T.; et al. Composite Hydrogels with Tunable Anisotropic Morphologies and Mechanical Properties. *Chem. Mater.* **2016**, acs.chemmater.6b00792.

[23] De France, K. J.; Chan, K. J. W. W.; Cranston, E. D.; Hoare, T. R. Enhanced Mechanical Properties in Cellulose Nanocrystal-Poly(oligo Ethylene Glycol Methacrylate) Injectable Nanocomposite Hydrogels through Control of Physical and Chemical Cross-Linking. *Biomacromolecules* **2016**, acs.biomac.5b01598.

[24] Hubbe, M.; Rojas, O.; Lucia, L.; Sain, M. Cellulosic Nanocomposites: A Review. *BioResources* **2008**, *3*, 929–980.

[25] Shopsowitz, K. E.; Hamad, W. Y.; MacLachlan, M. J. Chiral Nematic Mesoporous Carbon Derived from Nanocrystalline Cellulose. *Angew. Chem. Int. Ed. Engl.* **2011**, *50* (46), 10991–10995.

[26] Capron, I.; Cathala, B. Surfactant-Free High Internal Phase Emulsions Stabilized by Cellulose Nanocrystals. *Biomacromolecules* **2013**, *14* (2), 291–296.

[27] Mohanta, V.; Madras, G.; Patil, S. Layer-by-Layer Assembled Thin Films and Microcapsules of Nanocrystalline Cellulose for Hydrophobic Drug Delivery. *ACS Appl. Mater. Interfaces* **2014**, *6* (22), 20093–20101.

[28] Jorfi, M.; Foster, E. J. Recent Advances in Nanocellulose for Biomedical Applications. *J. Appl. Polym. Sci.* **2015**, *132* (14), 1–19.

[29] Camarero-Espinosa, S.; Rothen-Rutishauser, B.; Weder, C.; Foster, E. J. Directed Cell Growth in Multi-Zonal Scaffolds for Cartilage Tissue Engineering. *Biomaterials* **2016**, *74*, 42–52.

[30] Jabbour, L.; Bongiovanni, R.; Chaussy, D.; Gerbaldi, C.; Beneventi, D. Cellulose-Based Li-Ion Batteries: A Review. *Cellulose* **2013**, *20* (4), 1523–1545.

[31] Yang, X.; Shi, K.; Zhitomirsky, I.; Cranston, E. D. Cellulose Nanocrystal Aerogels as Universal 3D Lightweight Substrates for Supercapacitor Materials. *Adv. Mater.* **2015**.

[32] Belbekhouche, S.; Bras, J.; Siqueira, G.; Chappey, C.; Lebrun, L.; Khelifi, B.; Marais, S.; Dufresne, A. Water Sorption Behavior and Gas Barrier Properties of Cellulose Whiskers and Microfibrils Films. *Carbohydr. Polym.* **2011**, *83* (4), 1740–1748.

[33] Kedzior, S. A.; Graham, L.; Moorlag, C.; Dooley, B. M.; Cranston, E. D. Poly(methyl Methacrylate)-Grafted Cellulose Nanocrystals: One-Step Synthesis, Nanocomposite Preparation, and Characterization. *Can. J. Chem. Eng.* **2016**, *9999* (MAY).

[34] Goetz, L.; Mathew, A.; Oksman, K.; Gatenholm, P.; Ragauskas, A. J. A Novel Nanocomposite Film Prepared from Crosslinked Cellulosic Whiskers. *Carbohydr. Polym.* **2009**, *75* (1), 85–89.
[35] Kalia, S.; Dufresne, A.; Cherian, B. M.; Kaith, B. S.; Avérous, L.; Njuguna, J.; Nassiopoulos, E. Cellulose-Based Bio- and Nanocomposites: A Review. *Int. J. Polym. Sci.* **2011**, *2011*, 1–35.
[36] Petersen, N.; Gatenholm, P. Bacterial Cellulose-Based Materials and Medical Devices: Current State and Perspectives. *Appl. Microbiol. Biotechnol.* **2011**, *91* (5), 1277–1286.
[37] Eichhorn, S. J.; Dufresne, A.; Aranguren, M.; Marcovich, N. E.; Capadona, J. R.; Rowan, S. J.; Weder, C.; Thielemans, W.; Roman, M.; Renneckar, S.; et al. *Review: Current International Research into Cellulose Nanofibres and Nanocomposites*; 2010; Vol. 45.
[38] Iguchi, M.; Yamanaka, S.; Budhiono, A. Bacterial Cellulose — a Masterpiece of Nature's Arts. *J. Mater. Sci.* **2000**, *35*, 261–270.
[39] Salas, C.; Nypelö, T.; Rodriguez-Abreu, C.; Carrillo, C.; Rojas, O. J. Nanocellulose Properties and Applications in Colloids and Interfaces. *Curr. Opin. Colloid Interface Sci.* **2014**, *19* (5), 383–396.
[40] Siró, I.; Plackett, D. Microfibrillated Cellulose and New Nanocomposite Materials: A Review. *Cellulose* **2010**, *17* (3), 459–494.
[41] Saito, T.; Kimura, S.; Nishiyama, Y.; Isogai, A. Cellulose Nanofibers Prepared by TEMPO-Mediated Oxidation of Native Cellulose. *Biomacromolecules* **2007**, *8* (8), 2485–2491.
[42] Wågberg, L.; Decher, G.; Norgren, M.; Lindström, T.; Ankerfors, M.; Axnäs, K. The Build-up of Polyelectrolyte Multilayers of Microfibrillated Cellulose and Cationic Polyelectrolytes. *Langmuir* **2008**, *24* (3), 784–795.
[43] Paakko, M.; Ankerfors, M.; Kosonen, H.; Nykanen, A.; Ahola, S.; Osterberg, M.; Ruokolainen, J.; Laine, J.; Larsson, P. T.; Ikkala, O.; et al. Enzymatic Hydrolysis Combined with Mechanical Shearing and High-Pressure Homogenization for Nanoscale Cellulose Fibrils and Strong Gels. *Biomacromolecules* **2007**, *8* (6), 1934–1941.
[44] Österberg, M.; Cranston, E. D. Special Issue on Nanocellulose- Editorial. *Nord. Pulp Pap. Res. J.* **2014**, *29* (1).
[45] Per, S. Commercial Break-through in MFC Processing. *Commercial break-through in MFC processing*. FiberLean, Imerys Mineral AB: Munich 2014.
[46] *The Global Market for Nanocellulose to 2024*, 13th ed.; Future Markets, Inc.: Edinburg, UK, 2016.
[47] Cellulforce http://www.celluforce.com (accessed Jul 8, 2016).
[48] Dufresne, A. Nanocellulose: A New Ageless Bionanomaterial. *Mater. Today* **2013**, *16* (6), 220–227.
[49] *Cellulose Fibers: Bio- and Nano-Polymer Composites*; Kalia, S., Kaith, B. S., Kaur, I., Eds.; Springer Berlin Heidelberg: Berlin, Heidelberg, 2011.
[50] Bee, S.; Hamid, A.; Lee, H. V; Hamid, S. B. A.; Zain, S. K. Conversion of Lignocellulosic Biomass to Nanocellulose : Structure and Chemical Process Conversion of Lignocellulosic Biomass to Nanocellulose : **2015**, *2014* (July).

[51] Lagerwall, J. P. F.; Schütz, C.; Salajkova, M.; Noh, J.; Hyun Park, J.; Scalia, G.; Bergström, L. Cellulose Nanocrystal-Based Materials: From Liquid Crystal Self-Assembly and Glass Formation to Multifunctional Thin Films. *NPG Asia Mater.* **2014**, *6* (1), e80.
[52] Beck, S.; Bouchard, J.; Berry, R. Dispersibility in Water of Dried Nanocrystalline Cellulose. *Biomacromolecules* **2012**, *13*, 1486–1494.
[53] Camarero Espinosa, S.; Kuhnt, T.; Foster, E. J.; Weder, C. Isolation of Thermally Stable Cellulose Nanocrystals by Phosphoric Acid Hydrolysis. *Biomacromolecules* **2013**, *14* (4), 1223–1230.
[54] Orelma, H.; Filpponen, I.; Johansson, L. S.; Österberg, M.; Rojas, O. J.; Laine, J. Surface Functionalized Nanofibrillar Cellulose (NFC) Film as a Platform for Immunoassays and Diagnostics. *Biointerphases* **2012**, *7* (1–4), 1–12.
[55] Abitbol, T.; Cranston, E. D. Chiral Nematic Self-Assembly of Cellulose Nanocrystals in Suspensions and Solid Films. In *Handbook of Green Materials*; WORLD SCIENTIFIC, 2014; pp 37–56.
[56] Habibi, Y. Key Advances in the Chemical Modification of Nanocelluloses. *Chem. Soc. Rev.* **2014**, *43* (5), 1519–1542.
[57] Dufresne, A. *Nanocellulose: Potential Reinforcement in Composites*; 2012; Vol. 2.
[58] Wagner, R.; Moon, R.; Pratt, J.; Shaw, G.; Raman, A. Uncertainty Quantification in Nanomechanical Measurements Using the Atomic Force Microscope. *Nanotechnology* **2011**, *22* (45), 455703.
[59] Cranston, E. D.; Gray, D. G. Formation of Cellulose-Based Electrostatic Layer-by-Layer Films in a Magnetic Field. *Sci. Technol. Adv. Mater.* **2006**, *7* (4), 319–321.
[60] Li, D.; Liu, Z.; Al-Haik, M.; Tehrani, M.; Murray, F.; Tannenbaum, R.; Garmestani, H. Magnetic Alignment of Cellulose Nanowhiskers in an All-Cellulose Composite. *Polym. Bull.* **2010**, *65* (6), 635–642.
[61] Habibi, Y. Key Advances in the Chemical Modification of Nanocelluloses. *Chem. Soc. Rev.* **2014**, *43* (5), 1519–1542.
[62] Abitbol, T.; Marway, H.; Cranston, E. D. Surface Modification of Cellulose Nanocrystals with Cetyltrimethylammonium Bromide. *Nord. Pulp Pap. Res. J.* **2014**, *29* (1), 46–57.
[63] Bonini, C.; Heux, L.; Cavaillé, J.-Y. Y.; Lindner, P.; Charles Dewhurst; Terech‖, P.; Dewhurst, C.; Terech, P. Rodlike Cellulose Whiskers Coated with Surfactant: A Small-Angle Neutron Scattering Characterization. *Langmuir* **2002**, *18* (8), 3311–3314.
[64] Dhar, N.; Au, D.; Berry, R. C.; Tam, K. C. Interactions of Nanocrystalline Cellulose with an Oppositely Charged Surfactant in Aqueous Medium. *Colloids Surfaces A Physicochem. Eng. Asp.* **2012**, *415*, 310–319.
[65] Heux, L.; Chauve, G.; Bonini, C. Nonflocculating and Chiral-Nematic Self-Ordering of Cellulose Microcrystals Suspensions in Nonpolar Solvents. *Langmuir* **2000**, *16* (21), 8210–8212.
[66] Salajkova, M.; Berglund, L. a.; Zhou, Q.; Salajková, M.; Berglund, L. a.; Zhou, Q. Hydrophobic Cellulose Nanocrystals Modified with Quaternary Ammonium Salts. *J. Mater. Chem.* **2012**, *22* (37), 19798.

[67] Peng, B.; Han, X.; Liu, H.; Berry, R. C.; Tam, K. C. Interactions between Surfactants and Polymer-Grafted Nanocrystalline Cellulose. *Colloids Surfaces A Physicochem. Eng. Asp.* **2013**, *421*, 142–149.

[68] Padalkar, S.; Capadona, J. R.; Rowan, S. J.; Weder, C.; Won, Y. H.; Stanciu, L. a.; Moon, R. J. Natural Biopolymers: Novel Templates for the Synthesis of Nanostructures. *Langmuir* **2010**, *26* (11), 8497–8502.

[69] Petersson, L.; Kvien, I.; Oksman, K. Structure and Thermal Properties of Poly(lactic Acid)/cellulose Whiskers Nanocomposite Materials. *Compos. Sci. Technol.* **2007**, *67* (11–12), 2535–2544.

[70] Nagalakshmaiah, M.; El Kissi, N.; Dufresne, A. Ionic Compatibilization of Cellulose Nanocrystals with Quaternary Ammonium Salt and Their Melt Extrusion with Polypropylene. *ACS Appl. Mater. Interfaces* **2016**, *8* (13), 8755–8764.

[71] Kan, K. H. M.; Li, J.; Wijesekera, K.; Cranston, E. D. Polymer-Grafted Cellulose Nanocrystals as pH-Responsive Reversible Flocculants. *Biomacromolecules* **2013**, *14* (9), 3130–3139.

[72] Habibi, Y.; Goffin, A.-L.; Schiltz, N.; Duquesne, E.; Dubois, P.; Dufresne, A. Bionanocomposites Based on Poly(ε-Caprolactone)-Grafted Cellulose Nanocrystals by Ring-Opening Polymerization. *J. Mater. Chem.* **2008**, *18* (41), 5002.

[73] Yi, J.; Xu, Q.; Zhang, X.; Zhang, H. Temperature-Induced Chiral Nematic Phase Changes of Suspensions of poly(N,N-Dimethylaminoethyl Methacrylate)-Grafted Cellulose Nanocrystals. *Cellulose* **2009**, *16* (6), 989–997.

[74] Zoppe, J. O.; Habibi, Y.; Rojas, O. J.; Venditti, R. A.; Johansson, L. S.; Efimenko, K.; ??sterberg, M.; Laine, J. Poly(N -Isopropylacrylamide) Brushes Grafted from Cellulose Nanocrystals via Surface-Initiated Single-Electron Transfer Living Radical Polymerization. *Biomacromolecules* **2010**, *11* (10), 2683–2691.

[75] Kloser, E.; Gray, D. G. Surface Grafting of Cellulose Nanocrystals with Poly(ethylene Oxide) in Aqueous Media. *Langmuir* **2010**, *26* (16), 13450–13456.

[76] Sun, B.; Zhang, M.; Hou, Q.; Liu, R.; Wu, T.; Si, C. Further Characterization of Cellulose Nanocrystal (CNC) Preparation from Sulfuric Acid Hydrolysis of Cotton Fibers. *Cellulose* **2015**.

[77] Boluk, Y.; Danumah, C. Analysis of Cellulose Nanocrystal Rod Lengths by Dynamic Light Scattering and Electron Microscopy. *J. Nanoparticle Res.* **2013**, *16* (1), 2174.

[78] Lahiji, R. R.; Xu, X.; Reifenberger, R.; Raman, A.; Rudie, A.; Moon, R. J. Atomic Force Microscopy Characterization of Cellulose Nanocrystals. *Langmuir* **2010**, *26* (6), 4480–4488.

[79] Beck-Candanedo, S.; Roman, M.; Gray, D. G. Effect of Reaction Conditions on the Properties and Behavior of Wood Cellulose Nanocrystal Suspensions. *Biomacromolecules* **2005**, *6* (2), 1048–1054.

[80] Liu, D.; Chen, X.; Yue, Y.; Chen, M.; Wu, Q. Structure and Rheology of Nanocrystalline Cellulose. *Carbohydr. Polym.* **2011**, *84* (1), 316–322.

[81] Stroobants, a; Lekkerkerker, H.; Odijk, T. Effect of Electrostatic Interaction on the Liquid Crystal Phase Transition in Solutions of Rodlike Polyelectrolytes. *Macromolecules* **1986**, *19* (18), 2232–2238.

[82] Kaushik, M.; Putaux, J. L.; Fraschini, C.; Chauve, G.; Moores, A. Transmission Electron Microscopy for the Characterization of Cellulose Nanocrystals. *Transm. Electron Microsc. Intech* **2015**, 129–163.
[83] Ahvenainen, P.; Kontro, I.; Svedstrom, K. Comparison of Sample Crystallinity Determination Methods by X-Ray Diffraction for Challenging Cellulose I Materials. *Cellulose* **2016**, *23* (2), 1073–1086.
[84] Hasani, M.; Cranston, E. D.; Westman, G.; Gray, D. G. Cationic Surface Functionalization of Cellulose Nanocrystals. *Soft Matter* **2008**, *4* (11), 2238.
[85] Beck, S.; Method, M.; Bouchard, J. General Procedure for Determining Cellulose Nanocrystal Sulfate Half-Ester Content by Conductometric Titration. *Cellulose* **2015**, *22* (1), 101–116.
[86] Abitbol, T.; Kloser, E.; Gray, D. G. Estimation of the Surface Sulfur Content of Cellulose Nanocrystals Prepared by Sulfuric Acid Hydrolysis. *Cellulose* **2013**, *20* (2), 785–794.
[87] Edgar, C. D.; Gray, D. G. Smooth Model Cellulose I Surfaces from Nanocrystal Suspensions. *Cellulose* **2003**, *10* (4), 299–306.
[88] Holmberg, K.; Jonsson, B.; Kronberg, B.; Lindman, B. *Surfactants and Polymers in Aqueous Solution*, Second.; John Wiley and Sons, Ltd: West Sussex, 2003.
[89] Rosen, M. J.; Kunjappu, J. T. *Surfactants and Interfacial Phenomena*; John Wiley and Sons, Ltd: Hoboken, New Jersey, 2012.
[90] Patel, V.; Dharaiya, N.; Ray, D.; Aswal, V. K.; Bahadur, P. PH Controlled Size/shape in CTAB Micelles with Solubilized Polar Additives: A Viscometry, Scattering and Spectral Evaluation. *Colloids Surfaces A Physicochem. Eng. Asp.* **2014**, *455* (1), 67–75.
[91] Soler-Illia, G. J. D. A. A.; Sanchez, C.; Lebeau, B.; Patarin, J. Chemical Strategies to Design Textured Materials: From Microporous and Mesoporous Oxides to Nanonetworks and Hierarchical Structures. *Chem. Rev.* **2002**, *102* (11), 4093–4138.
[92] Hu, Z.; Cranston, E. D.; Ng, R.; Pelton, R. Tuning Cellulose Nanocrystal Gelation with Polysaccharides and Surfactants. *Langmuir* **2014**.
[93] Zeng, G.; Fu, H.; Zhong, H.; Yuan, X.; Fu, M.; Wang, W.; Huang, G. Co-Degradation with Glucose of Four Surfactants, CTAB, Triton X-100, SDS and Rhamnolipid, in Liquid Culture Media and Compost Matrix. *Biodegradation* **2007**, *18* (3), 303–310.
[94] Quennouz, N.; Hashmi, S. M.; Choi, H. S.; Kim, J. W.; Osuji, C. O. Rheology of Cellulose Nanofibrils in the Presence of Surfactants. *Soft Matter* **2015**.
[95] Becker, L. C.; Bergfeld, W. F.; Belsito, D. V.; Hill, R. a.; Klaassen, C. D.; Liebler, D.; Marks, J. G.; Shank, R. C.; Slaga, T. J.; Snyder, P. W.; et al. Safety Assessment of Trimoniums as Used in Cosmetics. *Int. J. Toxicol.* **2012**, *31* (6 Suppl), 296S–341S.
[96] Susan, P.; Lynn, W. *Final Report on the Safety Assessment of Cetrimonium Chloride, Cetrimonium Bromide, and Steartrimonium Chloride*; 1997; Vol. 16.
[97] Dreaden, E. C.; Alkilany, A. M.; Huang, X.; Murphy, C. J.; El-Sayed, M. a. The Golden Age: Gold Nanoparticles for Biomedicine. *Chem. Soc. Rev.* **2012**, *41* (7), 2740.

[98] Yoshii, N.; Okazaki, S. A Molecular Dynamics Study of Structural Stability of Spherical SDS Micelle as a Function of Its Size. *Chem. Phys. Lett.* **2006**, *425* (1–3), 58–61.
[99] Singer, M. M.; Tjeerdema, R. S. Reviews of Environmental Contamination and Toxicology: Continuation of Residue Reviews; Ware, G. W., Ed.; Springer New York: New York, NY, 1993; pp 95–149.
[100] De Nicola, A.; Kawakatsu, T.; Rosano, C.; Celino, M.; Rocco, M.; Milano, G. Self-Assembly of Triton X-100 in Water Solutions: A Multiscale Simulation Study Linking Mesoscale to Atomistic Models. *J. Chem. Theory Comput.* **2015**, *11* (10), 4959–4971.
[101] Robson, R.; Dennis, E. The Size, Shape, and Hydration of Nonionic Surfactant Micelles. Triton X-100. *J. Phys. Chem.* **1977**, *81* (11), 1075–1078.
[102] Paradies, H. H. Shape and Size of a Non-Ionic Surfactant Micelle - Triton X-100 in Aqueous-Solution. *J. Phys. Chem.* **1980**, *84*, 599–607.
[103] Myers, D. *Surfactant Science and Technology*; Wiley: Hoboken, New Jersey, 2005.
[104] Hawrelak, M.; Bennett, E.; Metcalfe, C. The Environmental Fate of the Primary Degradation Products of Alkylphenol Ethoxylate Surfactants in Recycled Paper Sludge. *Chemosphere* **1999**, *39* (5), 745–752.
[105] Borchardt, J. K. The Use of Surfactants in de-Inking Paper for Paper Recycling. *Curr. Opin. Colloid Interface Sci.* **1997**, *2* (4), 402–408.
[106] Smith, M. J.; Rao, V. K.; Shanklin, G. L. Method of Treating a Papermaking Furnish for Making Soft Tissue. 5,785,813, 1998.
[107] Osborn, T. W. Soft, Absorbent Tissue Paper. 1982, pp 1–4.
[108] Tiitu, M.; Laine, J.; Serimaa, R.; Ikkala, O. Ionically Self-Assembled Carboxymethyl Cellulose/surfactant Complexes for Antistatic Paper Coatings. *J. Colloid Interface Sci.* **2006**, *301* (1), 92–97.
[109] Penfold, J.; Tucker, I.; Petkov, J.; Thomas, R. K. Surfactant Adsorption onto Cellulose Surfaces. *Langmuir* **2007**, *23* (16), 8357–8364.
[110] Mata, J.; Patel, J.; Jain, N.; Ghosh, G.; Bahadur, P. Interaction of Cationic Surfactants with Carboxymethylcellulose in Aqueous Media. *J. Colloid Interface Sci.* **2006**, *297* (2), 797–804.
[111] Alila, S.; Boufi, S.; Belgacem, M. N.; Beneventi, D. Adsorption of a Cationic Surfactant onto Cellulosic Fibers I. Surface Charge Effects. *Langmuir* **2005**, *21* (18), 8106–8113.
[112] Hu, Z.; Patten, T.; Pelton, R.; Cranston, E. D. Synergistic Stabilization of Emulsions and Emulsion Gels with Water-Soluble Polymers and Cellulose Nanocrystals. *ACS Sustain. Chem. Eng.* **2015**, *3* (5), 1023–1031.
[113] Hu, Z.; Ballinger, S.; Pelton, R.; Cranston, E. D. Surfactant-Enhanced Cellulose Nanocrystal Pickering Emulsions. *J. Colloid Interface Sci.* **2014**, *439*, 139–148.
[114] Aloulou, F.; Boufi, S.; Belgacem, N.; Gandini, A. Adsorption of Cationic Surfactants and Subsequent Adsolubilization of Organic Compounds onto Cellulose Fibers. *Colloid Polym. Sci.* **2004**, *283* (3), 344–350.

[115] Syverud, K.; Xhanari, K.; Chinga-Carrasco, G.; Yu, Y.; Stenius, P. Films Made of Cellulose Nanofibrils: Surface Modification by Adsorption of a Cationic Surfactant and Characterization by Computer-Assisted Electron Microscopy. *J. Nanoparticle Res.* **2010**, *13* (2), 773–782.
[116] Elazzouzi-Hafraoui, S.; Putaux, J. L.; Heux, L. Self-Assembling and Chiral Nematic Properties of Organophilic Cellulose Nanocrystals. *J. Phys. Chem. B* **2009**, *113* (32), 11069–11075.
[117] Oksman, K.; Mathew, a. P.; Bondeson, D.; Kvien, I. Manufacturing Process of Cellulose Whiskers/polylactic Acid Nanocomposites. *Compos. Sci. Technol.* **2006**, *66* (15), 2776–2784.
[118] Ljungberg, N.; Bonini, C.; Bortolussi, F.; Boisson, C.; Heux, L.; Cavaillé. New Nanocomposite Materials Reinforced with Cellulose Whiskers in Atactic Polypropylene: Effect of Surface and Dispersion Characteristics. *Biomacromolecules* **2005**, *6* (5), 2732–2739.
[119] Bondeson, D.; Oksman, K. Polylactic Acid/cellulose Whisker Nanocomposites Modified by Polyvinyl Alcohol. *Compos. Part A Appl. Sci. Manuf.* **2007**, *38* (12), 2486–2492.
[120] Ljungberg, N.; Cavaillé, J. Y.; Heux, L. Nanocomposites of Isotactic Polypropylene Reinforced with Rod-like Cellulose Whiskers. *Polymer (Guildf).* **2006**, *47* (18), 6285–6292.
[121] Frka-Petesic, B.; Jean, B.; Heux, L. Unidirectional Orientation of Cellulose Nanocrystals in an Electric Field. In *ACS*; San Diego, CA, 2012.
[122] Bonini, C.; Heux, L.; Cavaillé, J.-Y.; Lindner, P.; Charles Dewhurst; Terech‖, P. Rodlike Cellulose Whiskers Coated with Surfactant: A Small-Angle Neutron Scattering Characterization. *Langmuir* **2002**, *18* (8), 3311–3314.
[123] Aloulou, F.; Boufi, S.; Beneventi, D. Adsorption of Organic Compounds onto Polyelectrolyte Immobilized-Surfactant Aggregates on Cellulosic Fibers. *J. Colloid Interface Sci.* **2004**, *280* (2), 350–358.
[124] Jackson, J. K.; Letchford, K.; Wasserman, B. Z.; Ye, L.; Hamad, W. Y.; Burt, H. M. The Use of Nanocrystalline Cellulose for the Binding and Controlled Release of Drugs. *Int. J. Nanomedicine* **2011**, *6*, 321–330.
[125] Binnig, G.; Quate, C. F. Atomic Force Microscope. *Phys. Rev. Lett.* **1986**, *56* (9), 930–933.
[126] Love, J. C.; Estroff, L. A.; Kriebel, J. K.; Nuzzo, R. G.; Whitesides, G. M. Self-Assembled Monolayers of Thiolates on Metals as a Form of Nanotechnology. *Chem. Rev.* **2005**, *105* (4), 1103–1169.
[127] Sinclair, J. D.; Soc, J. E.; Martin, Y.; Abraham, D.; Wickramasinghe, H. Corrosion Study of AA2024-T3 by Scanning Kelvin Probe Force Microscopy and In Situ Atomic Force Microscopy Scratching. *J. Electrochem. Soc.* **1998**, *145* (7).
[128] Garcia, R.; Herruzo, E. T. The Emergence of Multifrequency Force Microscopy. *Nat. Nanotechnol.* **2012**, *7* (4), 217–226.
[129] Ebeling, D.; Solares, S. D. Bimodal Atomic Force Microscopy Driving the Higher Eigenmode in Frequency-Modulation Mode: Implementation, Advantages, Disadvantages and Comparison to the Open-Loop Case. *Beilstein J. Nanotechnol.* **2013**, *4*, 198–207.

[130] Proksch, R. Multifrequency, Repulsive-Mode Amplitude-Modulated Atomic Force Microscopy. *Appl. Phys. Lett.* **2006**, *89* (11), 113121.
[131] Lamour, G.; Yip, C. K.; Li, H.; Gsponer, J. High Intrinsic Mechanical Flexibility of Mouse Prion Nanofibrils Revealed by Measurements of Axial and Radial Young's Moduli. *ACS Nano* **2014**, *8* (4), 3851–3861.
[132] Verwey, E. J. W.; Overbeek, J. T. G. Theory of the Stability of Lyophobic Colloids. *The Journal of physical and colloid chemistry*. 1947, pp 631–636.
[133] Derjaguin, B.; Landau, L. Theory of the Stability of Strongly Charged Lyophobic Sols and of the Adhesion of Strongly Charged Particles in Solutions of Electrolytes. *Prog. Surf. Sci.* **1948**, *43* (1–4), 30–59.
[134] Yasin, S.; Luckham, P. F.; Iqbal, T.; Feroze, N.; Zafar, M. Atomic Force Microscopy of Polymer Coated Graphitic Carbon Surfaces. *Soft Mater.* **2014**, *12* (4), 427–432.
[135] Israelachvili, J. *Intermolecular and Surface Forces, 1985*, Third Edit.; Academic Press Inc. (London) Ltd.: Walthman, MA, 2011.
[136] Butt, H. J.; Cappella, B.; Kappl, M. Force Measurements with the Atomic Force Microscope: Technique, Interpretation and Applications. *Surf. Sci. Rep.* **2005**, *59* (1–6), 1–152.
[137] Parsonage, E. Double Layer Capacitance of Poly (Acrylic Acid) at Metal/water Interfaces. *J. Colloid Interface Sci.* **1996**, *177* (177), 353–358.
[138] Buining, P.; Philipse, A. Phase Behavior of Aqueous Dispersions of Colloidal Boehmite Rods. *Langmuir* **1994**, *10* (7), 2106–2114.
[139] *Handbook of Adhesion Technology*; da Silva, L. F. M., Öchsner, A., Adams, R. D., Eds.; Springer Berlin Heidelberg: Berlin, Heidelberg, 2011.
[140] Kendall, K. *Molecular Adhesion and Its Applications: The Sticky Universe*; Kluwer Academic/ Plenum Publishers: New York, 2001.
[141] Krump, H.; Šimor, M.; Hudec, I.; Jaššo, M.; Luyt, A. S. Adhesion Strength Study between Plasma Treated Polyester Fibres and a Rubber Matrix. *Appl. Surf. Sci.* **2005**, *240* (1–4), 268–274.
[142] Vincent S.J., C.; Craig, V. S. J. An Historical Review of Surface Force Measurement Techniques. *Colloids Surfaces A Physicochem. Eng. Asp.* **1997**, *129–130*, 75–94.
[143] Fröberg, J. C.; Rojas, O. J.; Claesson, P. M. Surface Forces and Measuring Techniques. *Int. J. Miner. Process.* **1999**, *56* (1–4), 1–30.
[144] Ducker, W.; Senden, T.; Pashley, R. Direct Measurement of Colloidal Forces Using an Atomic Force Microscope. *Nature* **1991**, *353*.
[145] Roduit, C. Atomic Force Microscope and Cell Biology: The Mechanical Properties from the Membrane to the Interior of the Cell, Swiss Federal Institute of Technology Lausanne, 2009.
[146] Vakarelski, I.; Brown, S.; Rabinovich, Y.; Moudgil, B. Lateral Force Microscopy Investigation of Surfactant-Mediated Lubrication from Aqueous Solution. *Langmuir* **2004**, *20* (5), 1724–1731.
[147] Troncoso, P.; Saavedra, J. H.; Acuña, S. M.; Jeldres, R.; Concha, F.; Toledo, P. G. Nanoscale Adhesive Forces between Silica Surfaces in Aqueous Solutions. *J. Colloid Interface Sci.* **2014**, *424*, 56–61.

[148] Nordgren, N.; Lönnberg, H.; Hult, A.; Malmström, E.; Rutland, M. W. Adhesion Dynamics for Cellulose Nanocomposites. *ACS Appl. Mater. Interfaces* **2009**, *1* (10), 2098–2103.
[149] Cranston, E. D.; Gray, D. G.; Rutland, M. W. Direct Surface Force Measurements of Polyelectrolyte Multilayer Films Containing Nanocrystalline Cellulose. *Langmuir* **2010**, *26* (22), 17190–17197.
[150] Stiernstedt, J.; Nordgren, N.; Wågberg, L.; Brumer, H.; Gray, D. G.; Rutland, M. W. Friction and Forces between Cellulose Model Surfaces: A Comparison. *J. Colloid Interface Sci.* **2006**, *303* (1), 117–123.
[151] Lokanathan, A. R.; Uddin, K. M. A.; Rojas, O. J.; Laine, J. Cellulose Nanocrystal-Mediated Synthesis of Silver Nanoparticles: Role of Sulfate Groups in Nucleation Phenomena. *Biomacromolecules* **2014**, *15* (1), 373–379.
[152] Hasani, M.; Cranston, E. D.; Westman, G.; Gray, D. G. Cationic Surface Functionalization of Cellulose Nanocrystals. *Soft Matter* **2008**, *4* (11), 2238.
[153] White, B.; Banerjee, S.; Brien, S. O.; Turro, N. J.; Herman, I. P. Zeta-Potential Measurements of Surfactant-Wrapped Individual Single-Walled Carbon Nanotubes. **2007**, *2* (1), 13684–13690.
[154] Abitbol, T.; Palermo, A.; Moran-Mirabal, J. M.; Cranston, E. D. Fluorescent Labeling and Characterization of Cellulose Nanocrystals with Varying Charge Contents. *Biomacromolecules* **2013**, *14* (9), 3278–3284.
[155] Hopcroft, M. a; Nix, W. D.; Kenny, T. W. What Is the Young's Modulus of Silicon? *J. Microelectromechanical Syst.* **2010**, *19* (2), 229–238.
[156] *MFP-3D Manual Version 04_08*; Asylum Research: Santa Barbara, USA, 2008.
[157] Sader, J. E.; Chon, J. W. M.; Mulvaney, P. Calibration of Rectangular Atomic Force Microscope Cantilevers. *Rev. Sci. Instrum.* **1999**, *70* (10), 3967.
[158] Sader, J. Atomic Force Microscope Cantilevers (Calibration method of Sader) http://www.ampc.ms.unimelb.edu.au/afm/theory.html (accessed Mar 17, 2015).
[159] Hutter, J. L.; Bechhoefer, J. Calibration of Atomic-Force Microscope Tips. *Rev. Sci. Instrum.* **1993**, *64* (7), 1868–1873.
[160] Reid, M. S.; Villalobos, M.; Cranston, E. D. Cellulose Nanocrystal Interactions Probed by Thin Film Swelling for Nanocomposite Design. *Langmuir* **2015**, accepted.
[161] Ebeling, D.; Eslami, B.; Solares, S. D. J. Visualizing the Subsurface of Soft Matter: Simultaneous Topographical Imaging, Depth Modulation, and Compositional Mapping with Triple Frequency Atomic Force Microscopy. *ACS Nano* **2013**, *7* (11), 10387–10396.
[162] Nishino, T.; Takano, K.; Nakamae, K. Elastic Modulus of the Crystalline Regions of Cellulose Polymorphs. *J. Polym. Sci. Part B Polym. Phys.* **1995**, *33* (11), 1647–1651.
[163] Takagi, H.; Asano, A. Characterization Of "green" composites Reinforced by Cellulose Nanofibers. *Key Eng. Mater.* **2007**, *334–335 I*, 389–392.
[164] Azizi Samir, M. A. S.; Alloin, F.; Dufresne, A. Review of Recent Research into Cellulosic Whiskers, Their Properties and Their Application in Nanocomposite Field. *Biomacromolecules* **2005**, *6* (2), 612–626.

[165] Wagner, R.; Moon, R. J.; Raman, A. Mechanical Properties of Cellulose Nanomaterials Studied by Contact Resonance Atomic Force Microscopy. *Cellulose* **2016**.
[166] Usov, I.; Nyström, G.; Adamcik, J.; Handschin, S.; Schütz, C.; Fall, A.; Bergström, L.; Mezzenga, R. Understanding Nanocellulose Chirality and Structure-Properties Relationship at the Single Fibril Level. *Nat. Commun.* **2015**, *6* (May), 7564.
[167] Dishon, M.; Zohar, O.; Sivan, U. From Repulsion to Attraction and back to Repulsion: The Effect of NaCl, KCl, and CsCl on the Force between Silica Surfaces in Aqueous Solution. *Langmuir* **2009**, *25* (5), 2831–2836.
[168] Schneider, C.; Hanisch, M.; Wedel, B.; Jusufi, A.; Ballauff, M. Experimental Study of Electrostatically Stabilized Colloidal Particles: Colloidal Stability and Charge Reversal. *J. Colloid Interface Sci.* **2011**, *358* (1), 62–67.
[169] Olszewska, A.; Junka, K.; Nordgren, N.; Laine, J.; Rutland, M. W.; Österberg, M. Non-Ionic Assembly of Nanofibrillated Cellulose and Polyethylene Glycol Grafted Carboxymethyl Cellulose and the Effect of Aqueous Lubrication in Nanocomposite Formation. *Soft Matter* **2013**, *9* (31), 7448.
[170] Notley, S. M.; Eriksson, M.; Wågberg, L.; Beck-Candanedo, S.; Gray, D. G. Surface Force Measurements of Spin-Coated Thin Films with Different Crystallinity. *Langmuir* **2006**, *22* (7), 3154–3160.
[171] Chau, M.; Sriskandha, S. E.; Pichugin, D.; Thérien-Aubin, H.; Nykypanchuk, D.; Chauve, G.; Méthot, M.; Bouchard, J.; Gang, O.; Kumacheva, E. Ion-Mediated Gelation of Aqueous Suspensions of Cellulose Nanocrystals. *Biomacromolecules* **2015**, *16* (8), 2455–2462.
[172] Sato, T.; Ali, M. M.; Pelton, R.; Cranston, E. D. DNA Stickers Promote Polymer Adsorption onto Cellulose. *Biomacromolecules* **2012**, *13* (10), 3173–3180.
[173] Prathapan, R.; Thapa, R.; Garnier, G.; Tabor, R. F. Modulating the Zeta Potential of Cellulose Nanocrystals Using Salts and Surfactants. *Colloids Surfaces A Physicochem. Eng. Asp.* **2016**, *509*, 11–18.
[174] Vlachy, N.; Jagoda-Cwiklik, B.; Vácha, R.; Touraud, D.; Jungwirth, P.; Kunz, W. Hofmeister Series and Specific Interactions of Charged Headgroups with Aqueous Ions. *Adv. Colloid Interface Sci.* **2009**, *146* (1–2), 42–47.
[175] Jha, A. K.; Lee, J.; Tripathi, A.; Bose, A. Three-Dimensional Confinement-Related Size Changes to Mixed-Surfactant Vesicles. *Langmuir* **2008**, *24* (12), 6013–6017.
[176] Tan, G.; Ford, C.; John, V. T.; He, J.; McPherson, G. L.; Bose, A. Surfactant Solubilization and the Direct Encapsulation of Interfacially Active Phenols in Mesoporous Silicas. *Langmuir* **2008**, *24* (3), 1031–1036.
[177] Paria, S.; Khilar, K. C. A Review on Experimental Studies of Surfactant Adsorption at the Hydrophilic Solid-Water Interface. *Adv. Colloid Interface Sci.* **2004**, *110* (3), 75–95.
[178] Dupla, G.; Cedex, S.; Marques, M. F. F. Size of Sodium Dodecyl Sulfate Micelles in Aqueous Solutions as Studied by Positron Annihilation Lifetime Spectroscopy. **1996**, *3654* (96), 16608–16612.
[179] Zeng, X.; Osseo-Asare, K. Partitioning Behavior of Silica in the Triton X-100/dextran/water Aqueous Biphasic System. *J. Colloid Interface Sci.* **2004**, *272* (2), 298–307.

[180] Weisenhorn, A. L.; Maivald, P.; Butt, H. J.; Hansma, P. K. Measuring Adhesion, Attraction, and Repulsion between Surfaces in Liquids with an Atomic-Force Microscope. *Phys. Rev. B* **1992**, *45* (19), 11226–11232.
[181] Chau, M.; Sriskandha, S. E.; Pichugin, D.; Thérien-Aubin, H.; Nykypanchuk, D.; Chauve, G.; Méthot, M.; Bouchard, J.; Gang, O.; Kumacheva, E. Ion-Mediated Gelation of Aqueous Suspensions of Cellulose Nanocrystals. *Biomacromolecules* **2015**, *16* (8), 2455–2462.
[182] Cramer, G. R.; Läuchli, A.; Polito, V. S. Displacement of Ca2+ by Na+ from the Plasmalemma of Root Cells 1. *Plant Physiol.* **1985**, *79* (1), 207–211.
[183] Liu, J.; Min, G.; Ducker, W. a. AFM Study of Adsorption of Cationic Surfactants and Cationic Polyelectrolytes at the Silica - Water Interface. **2001**, No. 4, 4895–4903.
[184] Bremmell, K. E.; Jameson, G. J.; Biggs, S. Forces between Surfaces in the Presence of a Cationic Polyelectrolyte and an Anionic Surfactant. *Colloids Surfaces A Physicochem. Eng. Asp.* **1999**, *155* (1), 1–10.